National Library of Canada
Acquisitions and Bibliographic Services Branch
395 Wellington Street
Ottawa, Ontario
K1A 0N4

Bibliothèque nationale du Canada
Direction des acquisitions et des services bibliographiques
395, rue Wellington
Ottawa (Ontario)
K1A 0N4

Your file Votre référence

Our file Notre référence

NOTICE

The quality of this microform is heavily dependent upon the quality of the original thesis submitted for microfilming. Every effort has been made to ensure the highest quality of reproduction possible.

If pages are missing, contact the university which granted the degree.

Some pages may have indistinct print especially if the original pages were typed with a poor typewriter ribbon or if the university sent us an inferior photocopy.

Reproduction in full or in part of this microform is governed by the Canadian Copyright Act, R.S.C. 1970, c. C-30, and subsequent amendments.

AVIS

La qualité de cette microforme dépend grandement de la qualité de la thèse soumise au microfilmage. Nous avons tout fait pour assurer une qualité supérieure de reproduction.

S'il manque des pages, veuillez communiquer avec l'université qui a conféré le grade.

La qualité d'impression de certaines pages peut laisser à désirer, surtout si les pages originales ont été dactylographiées à l'aide d'un ruban usé ou si l'université nous a fait parvenir une photocopie de qualité inférieure.

La reproduction, même partielle, de cette microforme est soumise à la Loi canadienne sur le droit d'auteur, SRC 1970, c. C-30, et ses amendements subséquents.

Canada

INTEGRATED RECEIVER ARRAY SYSTEM FOR DIGITAL BEAMFORMING

By

YING SHEN, B. Eng. , M. Eng.

A Thesis
Submitted to the School of Graduate Studies
in Partial Fulfilment of the Requirements
for the Degree
Doctor of Philosophy

McMaster University
Octerber 1993

National Library of Canada
Acquisitions and Bibliographic Services Branch
395 Wellington Street
Ottawa, Ontario
K1A 0N4

Bibliothèque nationale du Canada
Direction des acquisitions et des services bibliographiques
395, rue Wellington
Ottawa (Ontario)
K1A 0N4

Your file Votre référence

Our file Notre référence

ISBN 0-315-93418-2

INTEGRATED RECEIVER ARRAY SYSTEM FOR DIGITAL BEAMFORMING

DOCTOR OF PHILOSOPHY (1993) MCMASTER UNIVERSITY
(Electrical and Computer Engineering) Hamilton, Ontario

TITLE:	**Integrated Receiver Array System for Digital Beamforming**
AUTHOR:	Ying Shen B. Eng. (Shanghai Univ. of Science and Technology) M. Eng. (Shanghai Univ. of Science and Technology)
SUPERVISOR(S):	Dr. J. Litva Professor, Department of Electrical and Computer Engineering
NUMBER OF PAGES:	xv,129

ABSTRACT

A C-band four-element integrated receiver system for digital beamforming (DBF) has been designed and implemented. For an array with digital beam processing, as a means of achieving precise pattern control (low sidelobe, adaptive nulling and high resolution) over large bandwidth and large dynamic range, the use of self-calibration techniques and circuitry was studied and evaluated. A multilayer linear self-calibration loop was also suggested and developed. Furthermore, in this thesis, the use of active antennas and optically controlled microwave devices in DBF systems was investigated.

Integrated antennas, as the first stage of the whole DBF system, are required for overcoming excessive power loss in large microstrip array antennas, for avoiding degraded array far-field pattern performance due to spurious radiation from microstrip feed networks and for larger effective isotropic radiated power (EIRP). The possibilities of using active antennas instead of conventional passive antennas are studied. Several new active antenna structures were proposed and implemented. Detailed design procedures and experimental results were given. Other applications for spatial power combiners and larger active antenna arrays were also addressed.

The optical control of microwave devices and subsystems is a rapidly growing area of research. In this thesis, the possibilities of using optical control in DBF systems are discussed. This thesis also describes the first reported application of frequency-dependent finite- difference time-domain ($(FD)^2TD$) method for modelling optoelectronic microwave semiconductor devices. The two major effects of a constantly illuminated semiconductor plasma which must be analyzed are: (i) the strong influence of carrier diffusion and recombination-generation processes on photoconductivity and (ii) the depth to which the plasma penetrates the device. Two examples of using modified $(FD)^2TD$ method to analyze a two-dimensional optically controlled dielectric resonators and three-dimensional optically controlled phase shifters / attenuators are presented. Finally, the comparison between available experimental results and theoretical results are discussed.

Acknowledgement

I would like to deeply thank my advisor, Professor John Litva, for all the education, support and encouragement he has given me in the past few years, and his guidance and directions in this work. I wish to thank the members of my advisory committee, Professor David Conn, and Professor P.G.Sutherland for their kindly assistance and comments.

My stay in McMaster has been made all the more meaningful and enjoyable due to the many friends I've come to know during my tenure here. I am especially endeared to my colleagues Charles Laperle and Perry Jarmuszewski, without them, the implementation of integrated receiver system would never have come to its fruition. I would also like to thank Kent Nickerson, Russ Fralich and Nagula Sangary for the meaningful cooperation at the work of interaction of microwave and optics and active array antennas, and to thank Chen Wu, Titus Lo and Zhiqiang Bi for their great assistance in my stuty. I am also thankful for the help, support,and kindness of the CRL personel.

Most importantly, I can never thank my family enough for their encouragement, understanding, and love. Without their support, none of this would have been possible.

Contents

List of Figures

List of Tables

Chapter 1

Introduction

Antenna radiation varies from omnidirectional to highly directional, and can be fixed or changed to accommodate specific needs as they arise.

In satellite communications, limited power resources and the crowding of synchronous orbital slots have created a demand for increased communications satellite capacity. Increasing the capacity of the communication system can be directly achieved by increasing the bandwidth through frequency reuse. However, the electromagnetic environment is becoming increasingly dense with a proliferation of unintentional and intentional interferences. Ever more information and sophistication are required from communications satellite systems and, therefore, the demands on antenna performance are steadily increasing. In this situation, digital beamforming, is a powerful technique to enhance antenna performance. Furthermore, for a fixed ratio of the received carrier level and noise, C/N and prechosen modulation system, the bandwidth can be increased by reducing the coverage area, using DBF technology.

Digital beamforming represents a quantum step in antenna performance and complexity. In a DBF array, the received signals are detected and digitized at the element level (Fig.1.1). The signals then are processed in a special-purpose digital computer to form the desired beam. This approach preserves the total information available at the aperture, i.e. the N individual element signals x_n, in contrast to an analog beamformer, which produces only the weighted sum of these signals and thus reduces the signal dimensionality from N to 1. The higher level of information coupled with the flexibility of digital processing allows for a number of attractive features beyond the capabilities of conventional arrays [1], [2], [3].

In summary, the advantages of DBF technology are as follows [2], [4], [5], [6]:

- Any number of closely spaced, low sidelobe beams can be formed without degradation in signal-to-noise ratio. This is in contrast to analogue multiple-beam-formers where the output beams must be orthogonal to avoid loss in signal power.
- Steerable beams can be assigned to individual mobile terminals to obtain the maximum gain for each mobile link beam.
- Adaptive beamforming can be carried out to suppress interferences as well as to increase the frequency reuse factor.
- All of the information arriving at the antenna is accessible to the signal processors. Distortions introduced by antenna hardware or signal processors can be corrected or minimized.
- Artificial intelligence has the potential for allowing DBF systems to make decisions based on received information and to learn from past experience.
- DBF systems are capable of greater system calibration accruacies and data rates and are directly amenable to adaptive beamforming and high resolution techniques. Antenna performance can be optimized in real-time.
- A DBF system has the potential for automatic calibration to optimize system performance.

DBF is a mating of antenna technology with digital technology. The incorporation of the radio frequency (RF) information to a digital format allows a multitude of digital signal processing techniques and algorithms to be applied to the spatial domain data. Key to this technology is the accurate translation of the analog signal to the digital regime. This is accomplished using high performance coherent receivers [7]. This thesis will describe a recent DBF receiving array system effort.

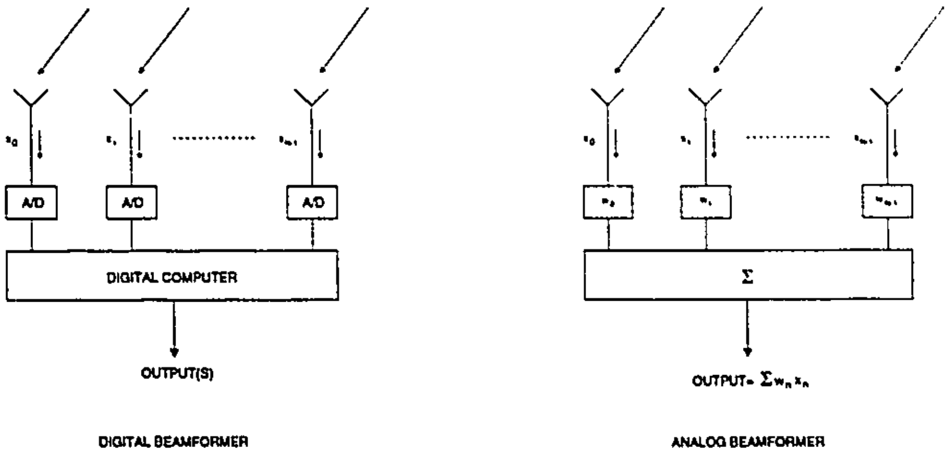

Figure 1.1: The digital beamformer (a) preserves and processes N individual signals. The analog beamformer (b) reduces the signal dimensionality from N to 1

1.1 Related Research

The discussion of research related to the topic of this thesis is divided into three areas, including study and implementation of a four-element DBF receiver array system, investigation of integrated active array antenna in DBF system and investigation of optical control in DBF system.

1.1.1 Integrated Receiving Array System for DBF

The earliest and still most ambitious reported DBF system is the ELRA phased array radar in Germany [8]. Its basic concept is to incorporate as extensive digital techniques as possible in a radar system. It has separate, circular transmit and receive arrays (300 elements and 768 elements, respectively) and operates at S band. Element calibration is performed via a fixed probe in the near-field. The outputs of the double-conversion receivers are combined into 48 subarrays with digital outputs, from which a number of beams are formed and the whole beam cluster is scanned by analog phase shifters. This radar system provided an ideal testbed for a variety of signal processing techniques.

Several experimental DBF systems have been reported in the UK. An eight-element array, intended to demonstrate rejection of barrage jamming, is discussed and experimental results on main beam nulling are presented in [9]. Another example is a partially adaptive array with 25 elements. The system operates at 3 GHz with a 5 MHz signal bandwidth. A discussion of experimental issues and results is given in [10].

In Canada, a sampled aperture radar system (SAMPAR) with 32 elements at X band, double-conversion transceiver, analog I and Q channels, was reproted by [11], [12]. The receivers are coherent, with frequency stability to 10^{-12}, accuracy of 0.1dB and 1°, 0.1Hz Doppler resolution, and 1 Hz to 2 KHz sampling rate. The transmitter has 100 mW CW into 22 dB horns with simultaneous dual frequencies, and horizontal or vertical polarization. The antenna array is a 32 element linear array with 1.82-meter aperture, 0.05715-meter inter-element spacing and matched within ±0.1 mm machine tolerance. It works at multi-frequencies, from 8.0 to 12.4 GHz with 30 MHz steps.

In the US, one large system, the CONUS B-OTH by GE Co., is an experimental over the horizon radar [13]. It is reported to be a bistatic system operating between 6 and 20 MHz with a bandwidth of about 100 KHz. On receive, up to 82 elements are used to form four simultaneous beams that cover the transmitted beamwidth. Adaptive nulling and on-line receiver error correction are provided.

Another DBF radar receiver array with eight elements at X band, double conversion receivers, analog I and Q channels and eight-bit ADCs is reported in [14]. The discussion includes a meticulous analysis of the error contributions from the various components in a proctical system.

Recently, a 76 element DBF receiver system was reported [7]. This system was delivered to the Army Missile Command by General Electric. The system worked at 5.25-5.85 GHz. Noise figure around 7 dB, signal bandwidth 400 KHz, Image rejection 50 dB and Dynamic range 72 dB. Image rejection requirements led to a triple down-conversion bandpass sampling direct receiver. The receivers use digital synchronous detection rather than conventional analog detection to provide high quality I and Q signals.

Another digital beam steering antenna is also provided by GE. The detailed specifications are given in [15].

A design study of using a DBF antenna for mobile satellite communications was given by W.Chujo et al. [16], [17]. The configuration of the DBF antenna for receive and transmit modes in digital communications is discussed. In the system, the antenna array whose elements are arranged rectangularly in 2×4 with half-wavelength spacing and excited for right-hand circular polarization was used, and continuous waves, without modulation signals at 1.54 GHz, were transmitted or received as RF signals. Calibration of the whole system except for antenna array was conducted in the digital section.

The architectures of DBF antennas are conceptual and it is prohibitively expensive to implement by combining individual components. The real challenge is then how to integrate the required components to be cost effectively. With today's MMIC technology [2], this is possible.

There are two basic design approaches. The first is the fully integrated approach, in which the array elements, coherent receivers, A/D converters, and DSP processors are fabricated in a single processing sequence on a large GaAs chip. The second approach is the hybrid monolithic approach in which the array is fabricated and combined in several layers. It is envisaged that ultimately a DBF antenna is as shown in Fig.1.2 [18]. The first layer of a DBF antenna, whether planar or conformal, will consist of a large number of patch antennas covering the wanted two-dimensional aperture. The subsequential layers are the MMIC coherent receivers, A/D circuits, and DSP processors. This approach is more practical and feasible using the present technology. This thesis will concentrate on the design and implementation of analogue part of a DBF receiver system by using the second approach. Chapter 2 will give a detailed discussion of the different architectures of an elemental receiver and

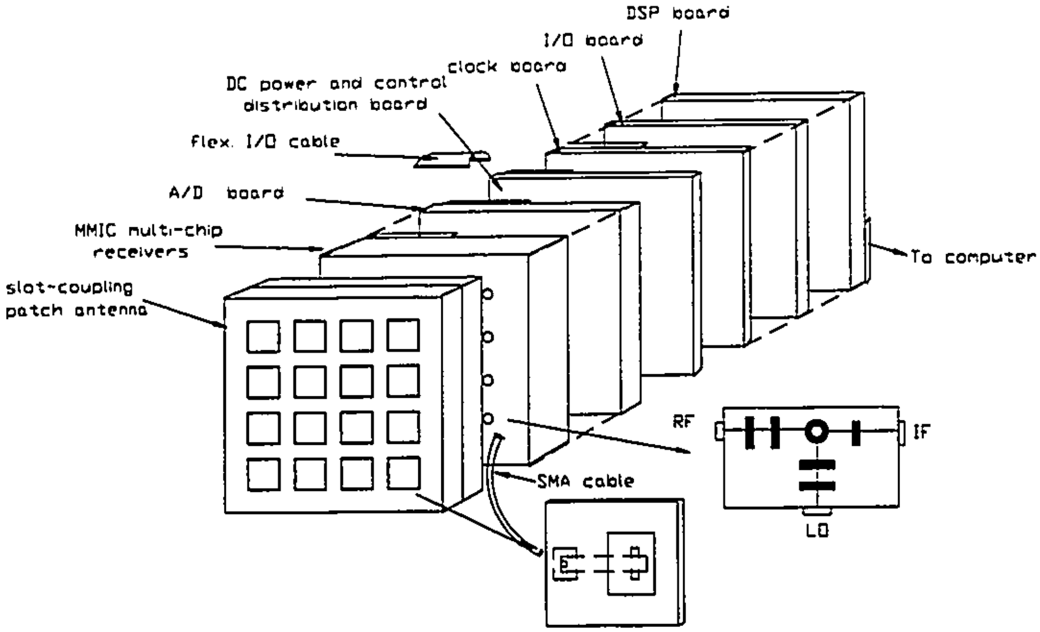

Figure 1.2: Architecture of an integrated DBF system

implementation of a multilayer integrated MMIC multichip DBF receiver, also give the errors in the elemental receiver and Omnisys analysis. Based on the one elemental receiver, design and implementation of a four-element DBF receiver system will be covered in Chapter 3. In order to achieving precise pattern control, array self-calibration techniques also will be presented in Chapter 3.

1.1.2 Integrated Active Array Antenna

Various antenna elements can be used as the first stage of the whole DBF system. These antenna elements include printed/microstrip antenna elements, horn elements, open-ended waveguide elements, slotted waveguide elements, and helical elements [2]. Microstrip antennas are expected to play an important role in future radar and communication systems thanks to the advantages of low profile, light weight, low cost, ease of mass production and ease of integration into arrays with MIC and MMIC techniques [19]. However, many of their applications are impeded by the inherent disadvantages such as low realized gain, narrow bandwidth, spurious radiation, poor polarization purity and losses in the feeding networks.

In recent years there has been much interest in combining active elements with traditional microstrip antennas. The primary motivation for this research is to overcome excessive power loss in large microstrip array antennas and to avoid degraded array far-field pattern performance due to spurious radiation along the microstrip feed network. To overcome both of these problems, it is highly desirable to supply the array with lower-power semiconductor sources at each element or subarray.

Some early work has been carried out in integrating antennas and sources into single units to form active antenna modules [20], [21], [22]. In this thesis, we will discuss several new active antenna structures, especially designed for multilayer structures. Details of design procedures and implementation of a one-element active receiver antenna and transmitter antenna for DBF applications are presented in Chapter 4. An elemental oscillator active antenna and a four-element active array antenna are also introduced. Furthermore, design and implementation of several larger active array structures for spacial power combiner, spacial amplifier and larger active array antenna are discussed.

1.1.3 Optically Controlled Microwave Devices

The MMIC program, one of the most successful ventures, has reached a high point, as a rapidly expanding and maturing area. Photonics has many potential applications, both military and civilian. A dominant feature of photonic devices and circuits is the invariable interaction between electrons and photons. Therefore, the interface between photonic and electronic processes presents a pivotal scientific and technological challenge [23].

Recently, research on photonic and microwave interaction has matured to the point that major applications are now within the realm of possibility. With regard to optical and microwave interaction, much of the work falls into two categories, the distribution of analog or digital microwave signals via high speed fiber-optic links, and the optical control and testing of microwave devices and circuits. The research in this thesis belongs to the second category.

The second category deals with the control and processing of microwave devices and signals by light. Here the optical input can be viewed as an extra terminal through which the performance of a microwave device or circuit, for example a MMIC, can be governed. Optically activated and controlled microwave switches, amplifiers, phase shifters and oscillators are examples of applications in this category [24], [25], [26], [27], [28]. Optical control techniques for MIC/MMIC transmit/receiver module also have been addressed [29], [30].

Quasi-static analysis is commonly used to analyze the optically controlled microwave devices [31], [32], [33]. The key advantage is its simplicity, but not accuracy. FDTD analysis used in picosecond photoconductive switches is first introduced by Sano [34]. The general FDTD method is capable of explicitly computing macroscopic transient electromagnetic interactions with general three-dimensional geometries. However, previous FDTD formulations were not capable of analyzing optically controlled microwave devices accurately for two reasons. First, FDTD requires that at each time step the permittivity and conductivity be specified as constants that do not depend on frequency, while even for the simplest interaction of microwave and optics these parameters vary with frequency. Second the permittivity of a plasma, when light shines on the semiconductors, can be negative, which can cause terms in FDTD expressions to become singular. In 1990, the frequency-dependent finite-difference time-domain $(FD)^2TD$ method was first presented by R.J.Luebbers et al. [35], [36]. It allows explicit calculation of wide-band transient electromagnetic interactions with frequency dependent materials and overcomes a serious limitation in current formulations of the FDTD method, which requires that the constitution parameters ϵ, μ, and σ be specified as constants.

This thesis will describe the development of the modified $(FD)^2TD$ method, which is the first reported full-wave analysis to model optoelectronic microwave semiconductor devices. The two major effects of a constantly illuminated semiconductor plasma which has analyzed are: (i) the strong influence of carrier diffusion and recombination-generation processes on photoconductivity and (ii) the depth to which the plasma penetrates the device. Chapter 5 will present details of the theoretical and experimental results. Possible optical control for DBF system will also be described.

1.2 Focus of Research

The focus of this work is to design and implement a MMIC multichip four-element integrated receiver system based on the implementation of one element receiver. The possibility of using integrated active antennas instead of traditional passive antenna at the first level of integrated DBF system will be given. Several new structures are suggested and tested. Also, the possibility of using optical control and a new full-wave analysis will be presented. Furthermore, the new structure of self-calibration loop for an integrated DBF system will be addressed.

1.3 Original Contribution

The major original contributions of this thesis are:

1. To design and implement (with Charles Laperle and Perry Jamuszewski) a C-band multi-layer integrated multichip receiver element for digital beamforming [2], [18], [37];
2. To design and implement (with Charles Laperle and Perry Jamuszewski) a C-band four-element integrated receiver system for digital beamforming;
3. To design and implement (with Charles Laperle and Perry Jamuszewski) a new self-calibration structure for multi-layer integrated receiving system [37];

4. To propose and implement a new active radiating oscillator model for integrated active radiating element [18], [38], [39];
5. To propose and implement a new four-element integrated active array structure [40], [41];
6. To propose and implement a new larger active array structure for spatial power combiner and active antenna array [42];
7. To extend the FDTD method to apply to various open dielectric resonator problems, including semi-open DRs, tuning screw DRs and multi-layer DRs, etc. [43], [44], [45], [46], [47];
8. To suggest a modified frequency-dependent FDTD method, to theoretically analyze the characteristics of optically controlled microwave semiconductor devices, and to successfully apply this to analyze a two-dimensional optically controlled dielectric resonators and three-dimensional optically controlled phase shifters / attenuators [48], [49], [50].

Chapter 2

MMIC Multi-Chip Integrated Receiver Element

2.1 Introduction

The digital beamforming array is characterized by (and limited by) the capabilities of the elemental receivers used in the array. The generic digital beamforming receiver contains the following functional elements:

1) A low noise amplifier to establish system noise figure.

2) A preselection filter to eliminate image band interference from the receiver.

3) One or more stages of down conversion to translate the receive signal to a suitable frequency band for signal spectrum match filtering and A/D quantization.

4) A filter to limit the spectrum width of the signals that are quantized.

5) A quantizer (A/D converter) subsystem.

6) Signal level overload control circuits.

7) Insertion phase and gain correction circuits.

8) Monitoring circuitry.

Since the elemental receivers are a significant factor in the cost of a digital beamforming array; it is important to use an architecture which is low cost and yet meets performance requirements. Channel to channel response match and dynamic range are the most critical performance factors of the elemental receiver since they determine the wide band noise interference adaptive cancellation performance of the digital beamforming array. Potential elemental receiver architectures and their relative capabilities are considered in the discussion which follows.

2.2 Elemental Receiver Architectures

2.2.1 Single Down Conversion Receiver

The single down conversion receiver is shown in Fig.2.1. It has the simplest architecture and is potentially low in cost. The simplicity of the architecture of the single down conversion receiver is offset by significant deficiencies in its performance. When the synchronous detector LO frequency is changed to tune the receiver over the operating band, the synchronous detector DC levels and in-phase and quadrature components balance may be expected to change. The synchronous detector outputs require compensation at each operating frequency because of phase and amplitude changes in the mixers as a function of LO frequency.

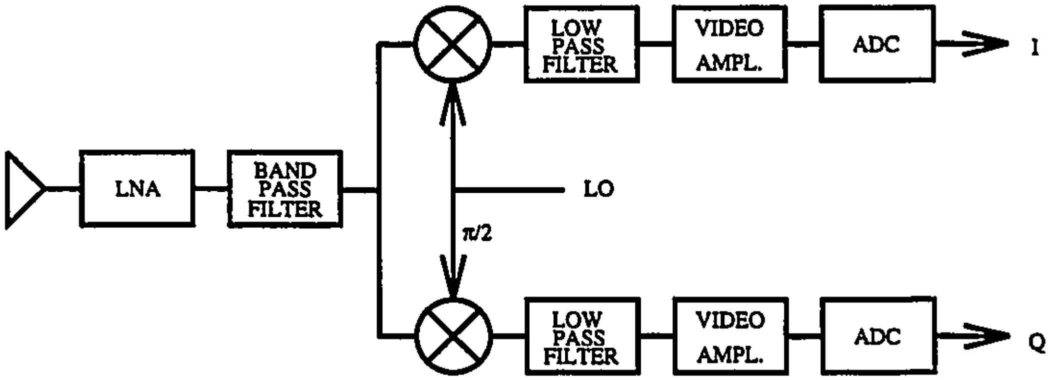

Figure 2.1: Single down conversion elemental receiver

The phase and amplitude relationship between the in-phase (I) and quadrature-phase (Q) outputs of the synchronous detector is also determined by the match between the two low pass filters following the synchronous detectors. The low-pass filters normally determine the signal bandwidth; stringent phase and amplitude matching requirements across the signal bandwidth make the filters difficult to build and hence expensive.

With only two amplifiers in a single down conversion receiver, it is difficult to realize large dynamic range, low noise figure and stable transfer characteristic. The low noise amplifier and video amplifiers must have sufficient gain to offset all receiver losses and raise the receiver self noise level to the quantization level of the A/D converters. There are adverse factors with having large gain either in the LNA or in video amplifiers. The dynamic range available from the synchronous detectors limit how much gain can be placed in the LNA before receiver dynamic range is impacted. Having high gain in the video amplifier leads to larger variations in the DC unbalance of the receiver. The noise figure of high output video amplifiers is usually poor, it is therefore undesirable to have large gain in the video amplifier to avoid increasing the receiver noise figure.

The single down conversion receiver is unsuitable for high performance DBF despite its low implementation cost.

2.2.2 Double Down Conversion Receiver

The double down conversion receiver shown in Fig.2.2 has a fixed LO for the synchronous detector reference; the synchronous detector balance and compensation is therefore independent of the agile operating frequency.

The agile mixer i-f output frequency must be high enough so that the image frequencies of the agile mixer can be rejected by the image rejection filter.

Although the match between receiver channels is improved by going to a double down conversion receiver there is still significant difficulty in attaining the channel matching needed for very low sidelobes.

Adding an i-f amplifier in the double conversion receiver does allow more flexibility

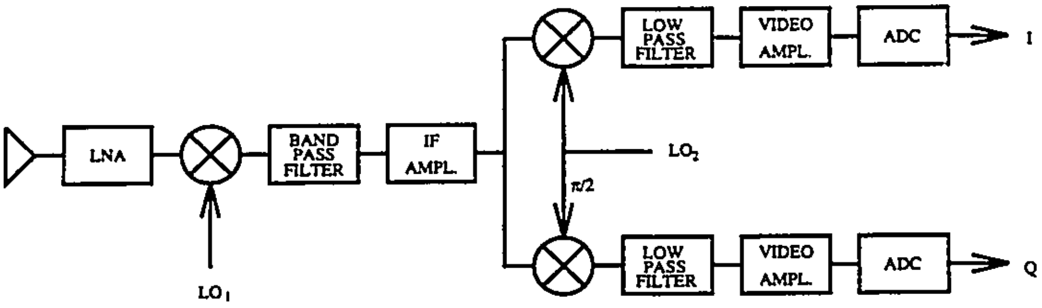

Figure 2.2: Double down conversion elemental receiver

in distributing the gain in the receiver. The three amplifiers in the receiver can be configured to have both large dynamic range and low noise figure in the overall receiver.

2.2.3 Triple Down Conversion Receiver

The addition of another mixer to the previous receiver architecture gives the triple down conversion receiver shown in Fig.2.3. This architecture allows the frequencies of the i-f stages to be optimized for specific functions. The second i-f frequencies can be made low enough to use a bandpass filter, like a surface acoustic wave (SAW) filter, to define the signal bandwidth. The SAW filter, being a finite impulse response filter, has very low phase and amplitude distortion. SAW filters can be built to be closely matched yielding elemental receiver responses which are highly correlated. The lower operating frequency for the synchronous detector makes the detector less sensitive to variations in the LO distribution. The synchronous detector minimum operating frequency is determined by the signal bandwidth and the low pass filtering available to reject the leakage from the LO and r-f inputs to the DC output of the synchronous detector mixers. The triple down conversion frequency receiver low pass filters are only used to reduce leakage components from the preceding mixers; they are made much wider than the signal bandpass to assure that they have virtually no impact on receiver matching.

The choice of filter bandwidths and center frequencies for the i-f stages are in-

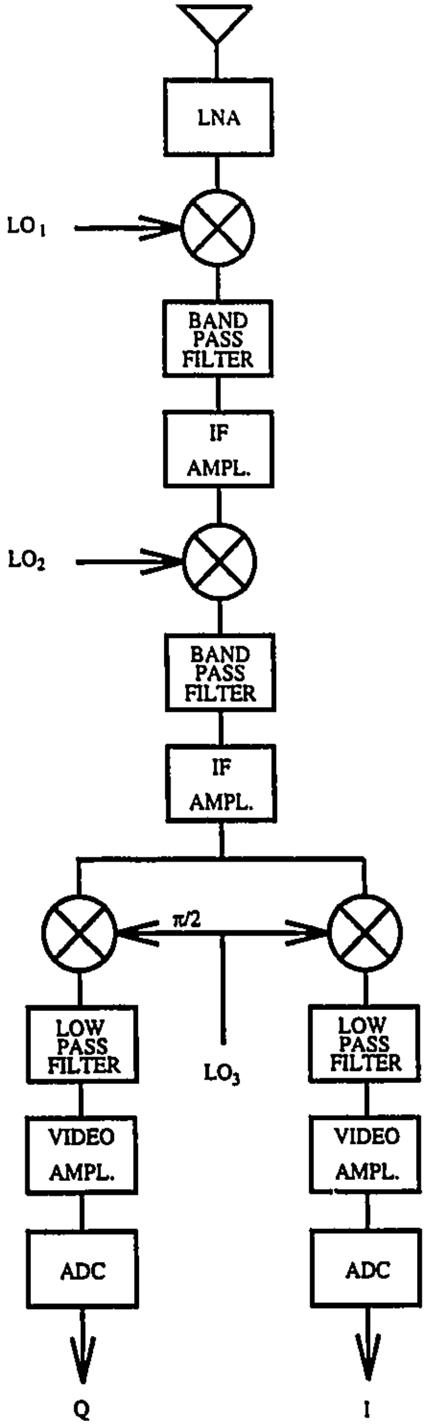

Figure 2.3: Triple down conversion elemental receiver

terrelated and require that compromises be made. The agile bandwidth is a major factor in determining the parameters of the i-f stages. The selection of the i-f filter frequencies is based on image response rejection requirements and the cost of matching responses.

A higher first i-f makes the first bandpass filter easier to realize but increases the difficulty of realizing the second bandpass image rejection filter. The second bandpass filter is required to be narrow enough to reject noise interference at the image response frequencies of the third i-f. The third i-f frequently has to be made higher than the minimum for the synchronous detector function to make the band pass filter responses more realizable.

The triple down conversion receiver has sufficient flexibility to be configured to have large dynamic range, low noise figure and relatively stable transfer characteristic; it would therefore be the preferred implementation form of the three baseband receivers for DBF system.

2.2.4 Bandpass Sampling Direct Conversion Receiver

The previous three kinds of baseband receivers have several deficiencies because the detector yields baseband in-phase (I) and a quadrature (Q) output signals from mixing the last i-f signal with a reference local oscillator (LO). The final signal bandwidth in the receiver is set by the last i-f band pass filter or alternatively by the lowpass filters on the I/Q baseband signals. The major performance limitations of the baseband receivers are:

1) The quality of the signal match which can be achieved in the I and Q signals, within a receiver channel and between receiver channel, is over the signal bandwidth;

2) The detector quality is determined by the match between the I and Q amplitudes and the degree to which phase quadrature is maintained between the components;

3) Error coming from dc offset;

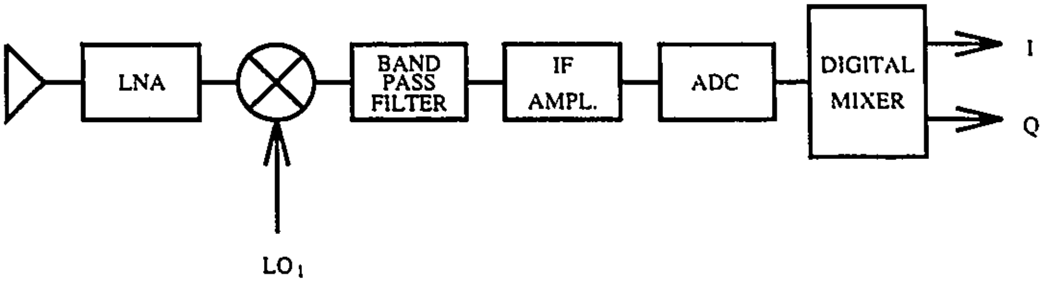

Figure 2.4: Bandpass sampling direct conversion elemental receiver

4) Spurious responses from device non-linearities.

The amplitude matching and the phase orthogonality of the I and Q channels are extremely critical and tend to be a major source of error. This has created interest in an alternative conversion technique (Fig.2.4) where the signal is sampled and digitized at IF and the complex video signal is generated digitally using the Hilbert transform or a FIR filter. This approach eliminates the lowpass filters, the video amplifiers and the two ADCs at the expense of one faster ADC and some additional digital circuitry.

Since the I and Q outputs are formed in a digital filter in the direct i-f conversion receiver, I and Q matching problem are effectively eliminated from the channel. However, the sampling jitter requirements of the quantizer in the direct i-f carrier sampling architecture, are higher than in base band receiver, because the carrier frequency must be accurately sampled to recover the signal phase information.

The complexity of the receiver can be significantly reduced in a direct i-f conversion receiver if the i-f sampler is placed at the highest i-f frequency that can be sampled and still meet dynamic range and matching requirements.

2.3 Implementations of DBF Element

2.3.1 Schematic of a DBF Receiver Element

Fig.2.5 shows the block diagram of a receiver module used in a four-element DBF receiver system. A double down conversion with bandpass sampling receiver, which

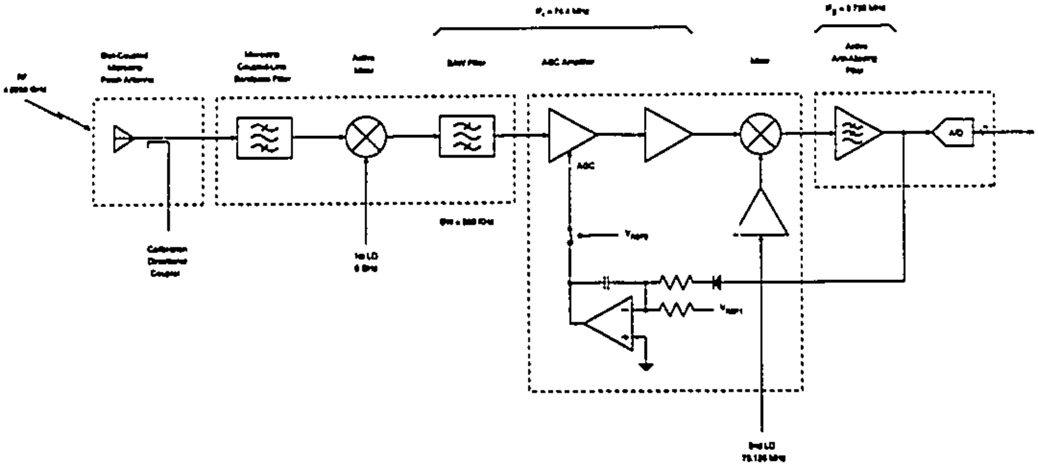

Figure 2.5: Block diagram of element receiver in DBF system

combines the advantages of multi-down conversion and IF-direct sampling structures, was used to meet the low cost and yet meet performance requirements based on current commercial MMIC chips.

Each receiver module is divided into five mechanical layers. The first layer is the radiating element which contains a multilayer slot coupled patch antenna and calibration signal couplers. The details of the calibration functions will be discussed in Chapter 3. The second layer consists of a microstrip coupled line bandpass filter, the first down-converter and a SAW filter. The chip used for the first down-converter is the model CV 0602-A from Pacific Monolithics, and the SAW filter is the model CTI-1529 from Siemens. The first down-converter brings the RF at 4.9256 GHz down to the first IF at 74.4 MHz, the SAW filter sets the signal bandwidth for the receiver ($\approx$ 360 KHz). The third layer includes automatic gain controlled (AGC) amplifier, a second IF amplifier and a second mixer. The AGC is used for balancing the signal level of each element of the array system and for increasing the dynamic range of the receiver. This layer also includes the switch which gives the option to choose whether the AGC will be used or not. The chip used for the AGC is a CLC-520 and the voltage feedback is provided by a CLC-420 both from Comlinear. The second IF amplifier uses two MAR-4 small signal amplifiers from Mini-Circuits, and the second mixer is the model RMS-1 also from Mini-Circuits. The second mixer brings the first IF from 74.4 MHz down to 3.725 MHz. The fourth layer contains the anti-aliasing filter which uses four current feedback op-amps model CLC-400 from Comlinear to filter the high frequencies and prevent aliasing in the A/D converter. The last layer contains the local oscillator, which includes the first and the second LO. Because DBF receivers must keep both phase and amplitude information, the two local oscillators must be coherent. In our implementation, the second LO is obtained directly from the first LO by using three prescaler chips (models UPG 503B, UPB 585G and UPB 587G from NEC). The first LO is at 5 GHz, and the second LO is at 78.125 MHz. Fig.2.6 shows the block diagram of the local oscillators distribution for the DBF receiver. The first LO uses a dielectric resonator oscillator model M5080 from General Microwave Co., followed by a Wilkinson power divider which feeds a series of three ÷4 prescalers. The output impedance of the last prescaler is transformed from 200 Ω to 50 Ω using a model T4-1 transformer from Mini-Circuits followed by a MAR-3 and a MAR-4 small-signal amplifiers (also from Mini-Circuits) to increase the power level. Finally, a bandpass filter is used to filter harmonics and leave a clean signal for the LO of the second mixer. to a bandpass filter to clear the spectrum and to distribute the signal to the second mixer.

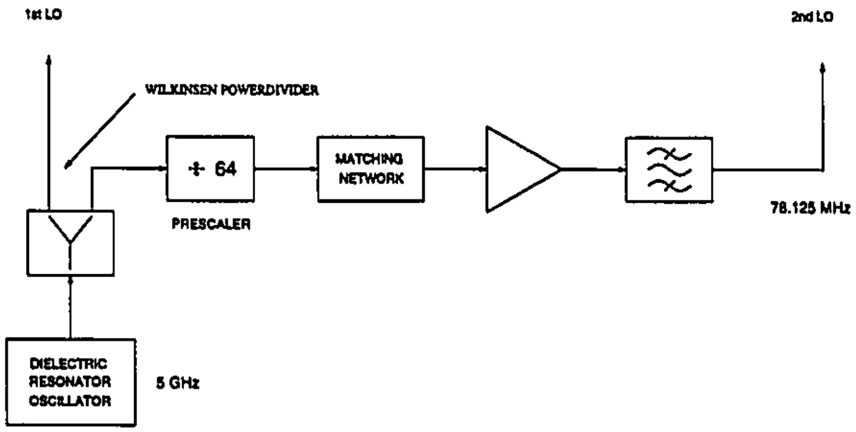

Figure 2.6: Block diagram of local oscillator layer for element receiver

2.3.2 Experimental Results

Fig.2.7 shows the layout of the multilayer integrated receiver module for the DBF system, and Fig.2.8 presents a photograph of the receiver. The receiver specifications and characteristics are given in Table 2.1.

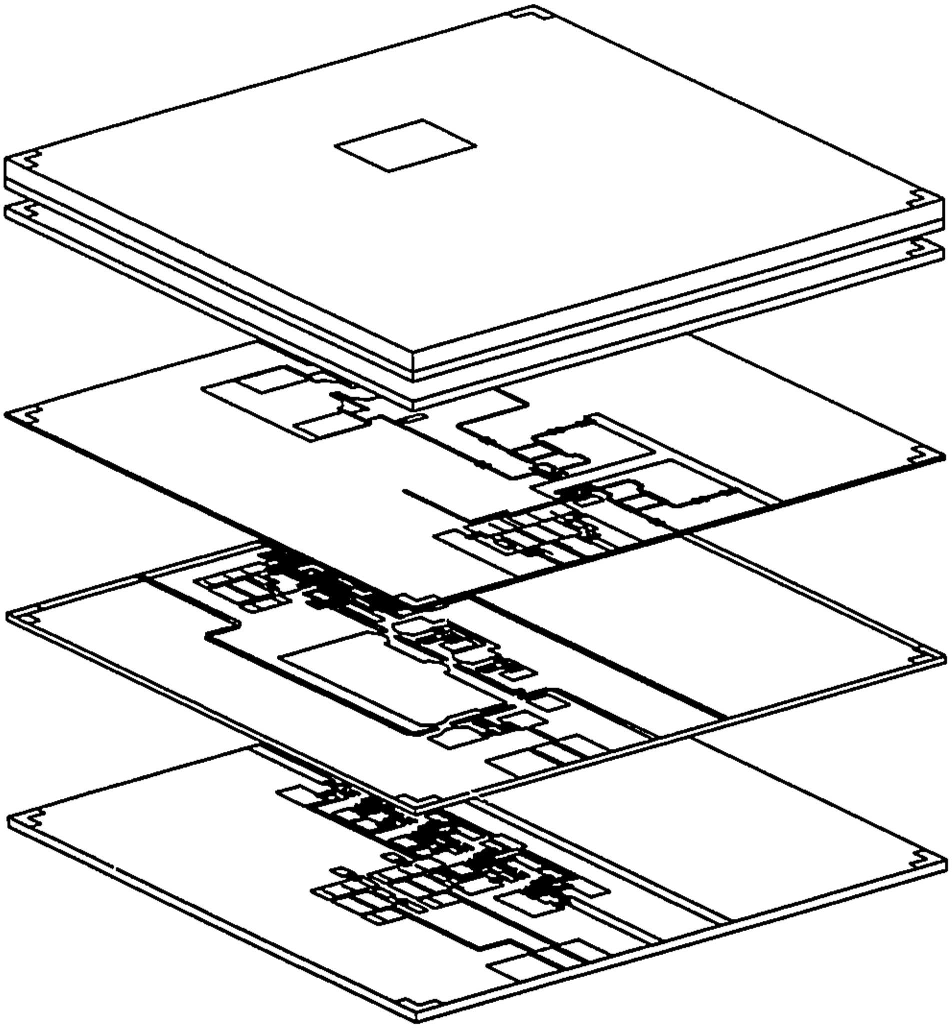

Figure 2.7: Digital beamforming receiver module

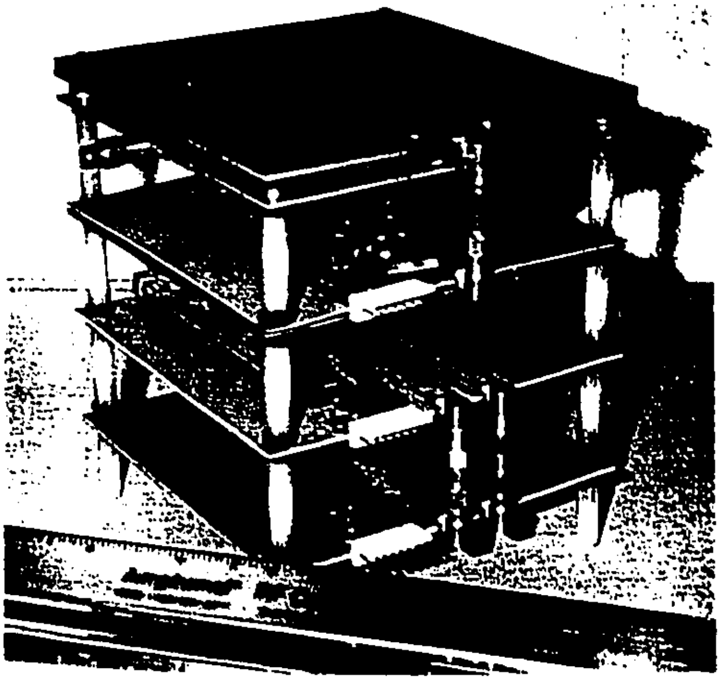

Figure 2.8: Photograph of the DBF receiver

Table 2.1: DBF receiver module characteristics

Center Frequency	4.9256	GHz
Signal Bandwidth	360	KHz
Noise Figure	9.8	dB
A/D Resolution	8	Bit
Maximum Receiver Input	-10	dBm
AGC Range	39 (-10 dBm to -49 dBm)	dB
Dynamic Range	50 (without AGC)	dB
	90 (with AGC)	dB
Receiver Gain	64	dB

2.4 Analysis Approach

2.4.1 Errors in DBF Receiver Element

One of the requirements of a DBF is to provide very deep nulls against interference sources such as mainlobe or sidelobe jammers. The cancellation performance of a DBF array is determined in part by the jamming environment (number of jammers, effective radiated power, spacing and multipath conditions) and the imperfections in the components which make up the DBF array system. The component imperfections include phase errors, amplitude errors and non-linearities which limit the ability to form deep nulls in the array response over the entire signal bandwidth.

The OmniSys software package from EEsof was used in evaluating component errors and total receiver errors for the purpose of creating error budgets and evaluating the system performance of DBF receivers. Each error source in the receiver was analyzed to determine its effect on system performance.

In the analogue section of the receiver, the sources of error generally considered are as follows:

1) RF section amplitude and phase mismatch.
2) RF section time delay mismatch.
3) First down-convertor amplitude and phase mismatch.
4) IF section amplitude and phase mismatch.
5) IF section time delay mismatch.
6) SAW filter frequency mismatch.
7) Second mixer amplitude and phase mismatch.
8) Second IF section amplitude and phase mismatch.
9) Second IF section time delay mismatch.

2.4.2 OmniSys Analysis

In this thesis, OmniSys was used with measured large-signal S-parameters of each constituent component, to predict the overall receiver system performance which includes gain, noise, dynamic range, non-linearities, spurious signals, intermodulation distortion, 1dB compression point, 3rd-order intercept point, and so on.

Fig.2.9 shows the block diagram of the DBF receiver simulated using OmniSys. In this system, the RF input is varied from 4.922 to 4.927 GHz, LO1 is 5 GHz, LO2 is 78.125 MHz, and the IF output varies from 1.2 to 5.12 MHz. Data from external files is as follows: BPF, SAWF, AGC (without feedback) and AMP are measured by a HP8510B network analyzer. Additional components (mixers, coaxial lines, microstrip lines and active filters) are modeled using OmniSys linear and nonlinear component models. Most parameters used in the simulation were taken from measurements. The simulation file for the OmniSys simulation is given in AppendixA.

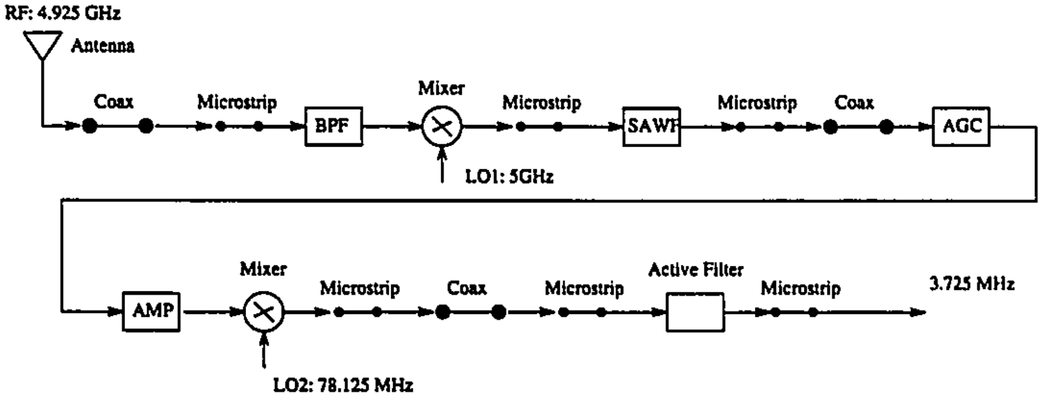

Figure 2.9: Block diagram of DBF receiver in OmniSys simulation

Fig.2.10 shows the IF output spectrum for different RF input levels. From the results, we can see that the receiver, in the case of no AGC, will saturate when the RF input power level is approximately -40 dBm. It is in very good agreement with the experimental result of -42 dBm. Fig.2.11 shows the receiver gain at IF. At the IF center frequency of 3.725 MHz, the maximum gain is 67 dB which also agrees very well with the experimental result of 64 dB. Fig.2.12 gives the noise figure (NF) of

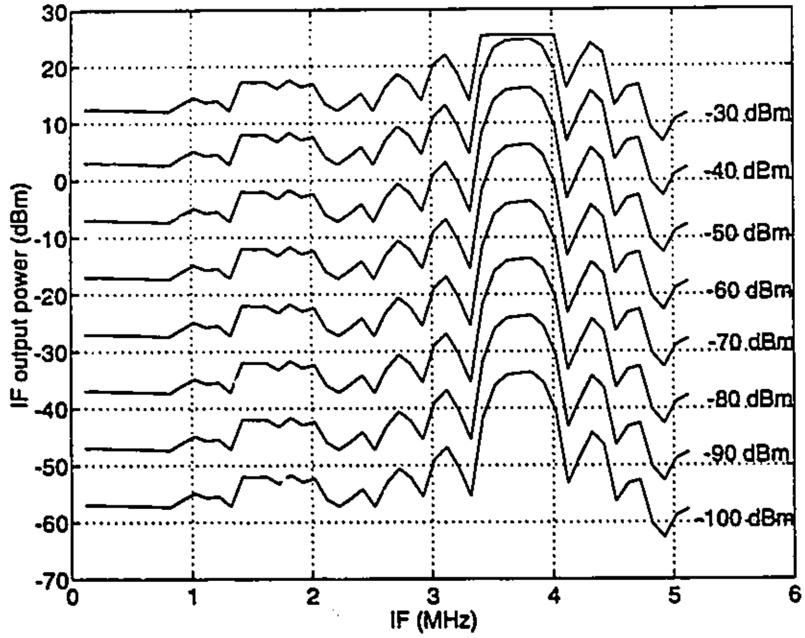

Figure 2.10: Output spectrum of the receiver

the whole receiver. Within the signal bandwidth the minimum NF is 9.982 dB and the experimental result is 9.8 dB. The output gain compression is shown in Fig.2.13. Gain compression is calculated as small gain minus large signal gain, therefore, the system 1dB compression point is approximately at -43 dBm (the input RF power level). When the RF level is at -30 dBm, the gain compression is about 11 dB.

Simulation also gives the results about the 1dB gain compression point, output 3rd-order intercept, S11 and group delay all at IF. Fig.2.14 - Fig.2.17 shows all the corresponding results.

Comparison of experimental and simulation results of the receiver output is shown in Fig.2.18. The signal bandwidth is mainly determined by the SAW filter, and the measurement and simulation agree very well, except the center frequency is a little bit shift.

Table.2.2 gives the BUDGET analysis using OmniSys. This analysis presents the performance of the cascaded components defined in Fig.2.9. Some system parameters

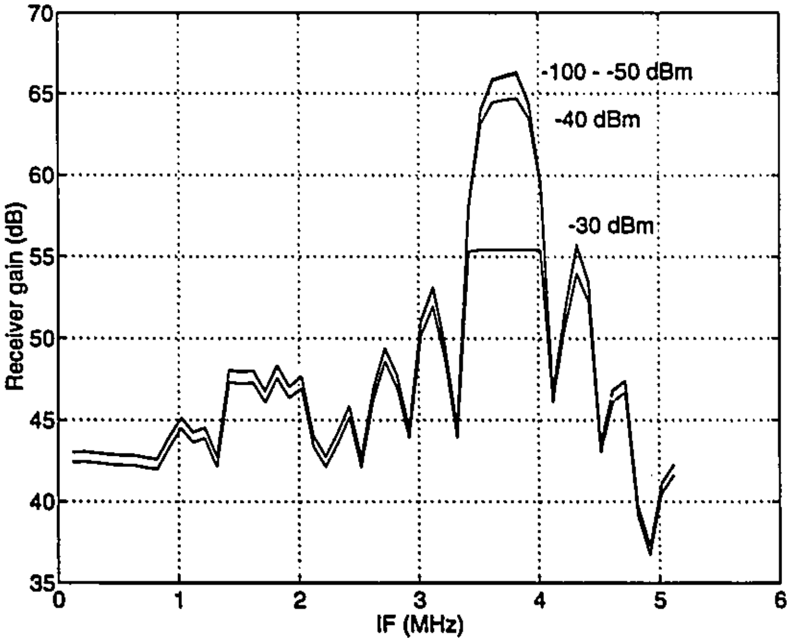

Figure 2.11: Receiver Gain of the receiver

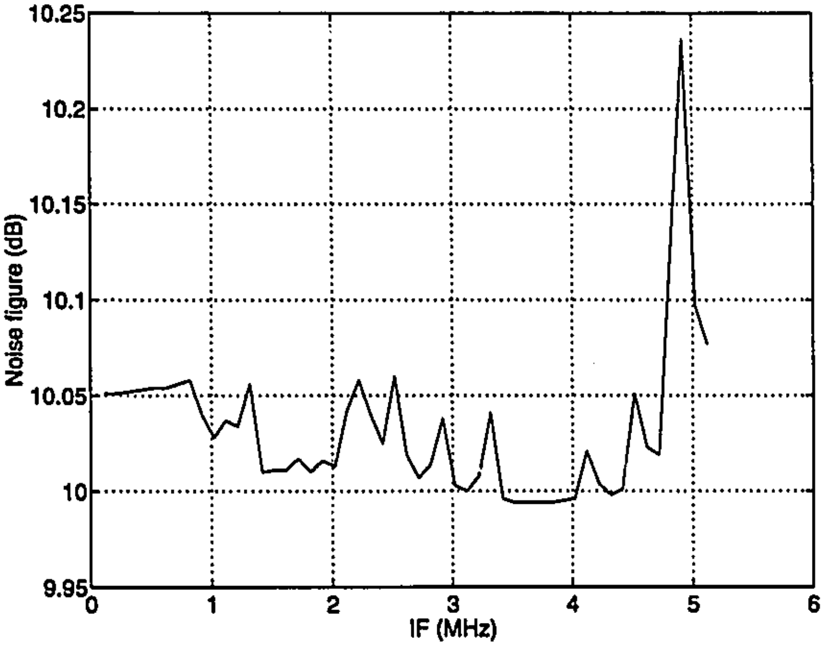

Figure 2.12: Noise figure of the receiver

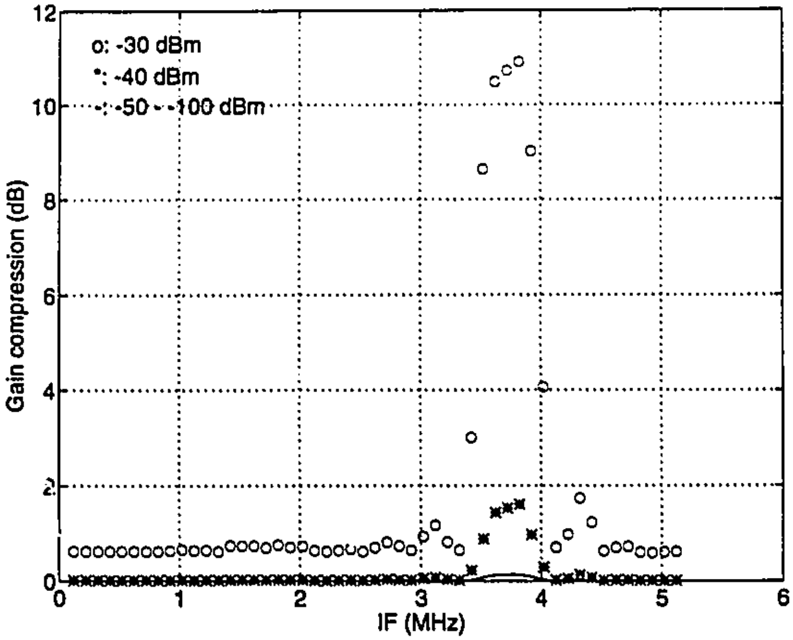

Figure 2.13: Gain compression of the receiver

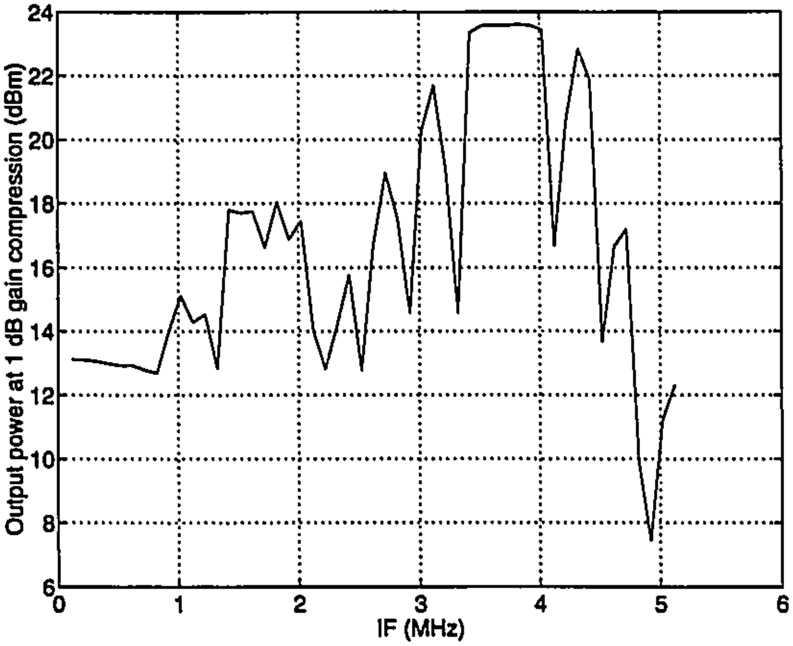

Figure 2.14: 1dB gain compression of the receiver

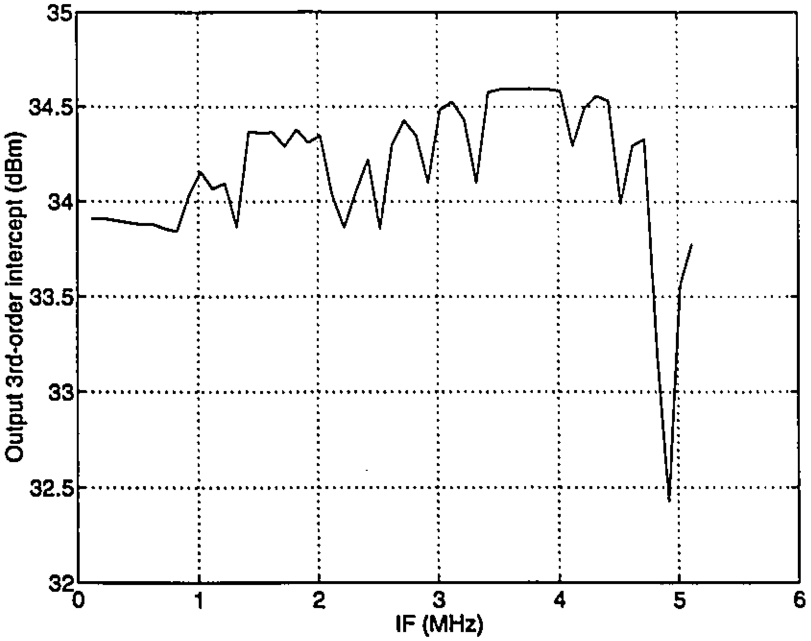

Figure 2.15: Output 3rd-order intercept of the receiver

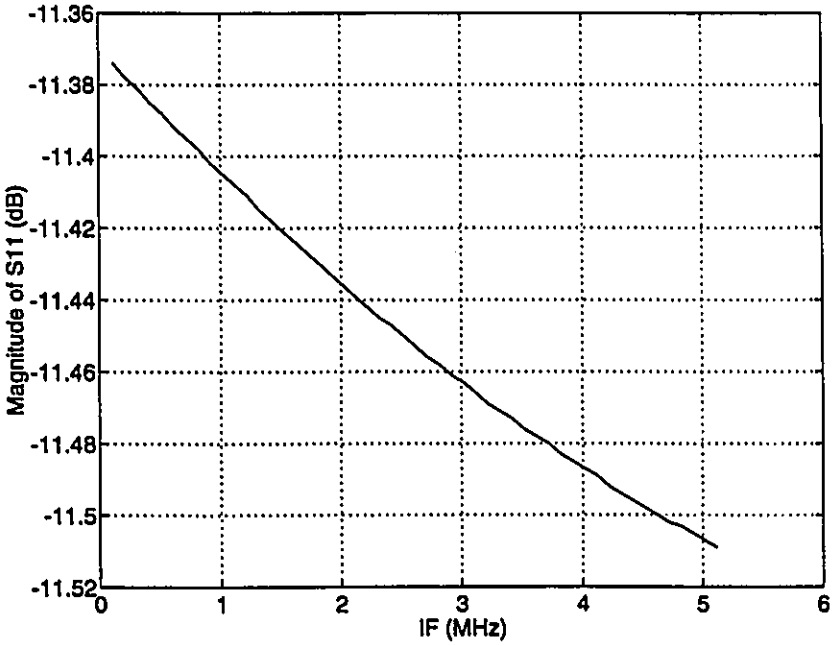

Figure 2.16: Magnitude of S11 of the receiver

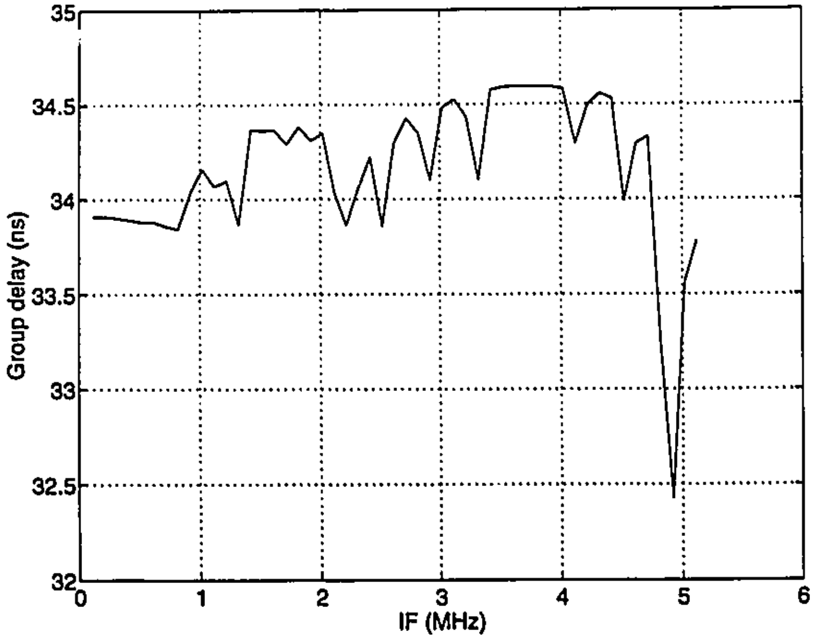

Figure 2.17: Group delay of the receiver

such as gain, noise figure, output 3rd-order intercept, IF power, 1dB compression point and dynamic range have been analyzed. Table 2.2 shows all these parameters at each node in Fig.2.9 and simulated at -60 dBm input RF power and 3.725 MHz output frequency. The BUDGET analysis gives a clear view of how each component influences the performance of the whole system. In our case, the dynamic range, noise figure and output 3rd-order intercept are mainly confined to the first downconverter. System performance can be greatly improved if we have better first downconverter chip.

Finally, the spectrum analysis capability of OmniSys is used to simulate the DBF receiver. The spectrum analysis includes all system nonlinearities and odd-order intermodulation products. The input signal is a two-tone RF signal, i.e., 4.9255 GHz and 4.9257 GHz. Fig.2.19 gives the simulation results, when the power level of modulated signal is varied from -100 dBm to -40 dBm. At low levels, the output spectrum is free of intermodulation products. On top of each figure there is a frequency re-

Table 2.2: BUDGET analysis of the DBF receiver module

NAME	GAIN	NF	IP3O	POWER	1DBCO	DYNAMIC RANGE
	dB	dB	dBm	dBm	dBm	dB
TLIN	-0.429	9.982	1000.0	-100.429	1000.0	1000.0
MLIN	-0.515	9.982	1000.0	-100.515	1000.0	1000.0
S2PA	-2.155	9.908	1000.0	-102.155	1000.0	1000.0
MIX	17.72	9.068	5.988	-82.28	-7.579	39.137
MLIN	17.673	7.260	5.979	-82.327	-7.588	39.175
S2PB	-2.601	7.253	-18.841	-102.601	-32.408	34.630
MLIN	-2.601	0.306	-18.841	-102.601	-32.408	34.629
TLIN	-2.602	0.292	-18.842	-102.602	-32.409	34.629
S2PC	15.797	0.292	-0.444	-84.203	-14.011	34.627
S2PD	33.304	2.627	18.029	-66.696	4.462	35.593
MIX	27.366	17.665	10.601	-72.634	-2.772	34.296
MLIN	27.366	11.610	10.600	-72.634	-2.772	34.296
TLIN	27.366	11.610	10.600	-72.634	-2.772	34.295
MLIN	27.366	11.610	10.600	-72.634	-2.773	34.295
GAIN1	46.868	11.610	30.100	-53.132	16.727	34.270
MLIN	46.868	0.000	30.099	-53.132	16.727	34.27

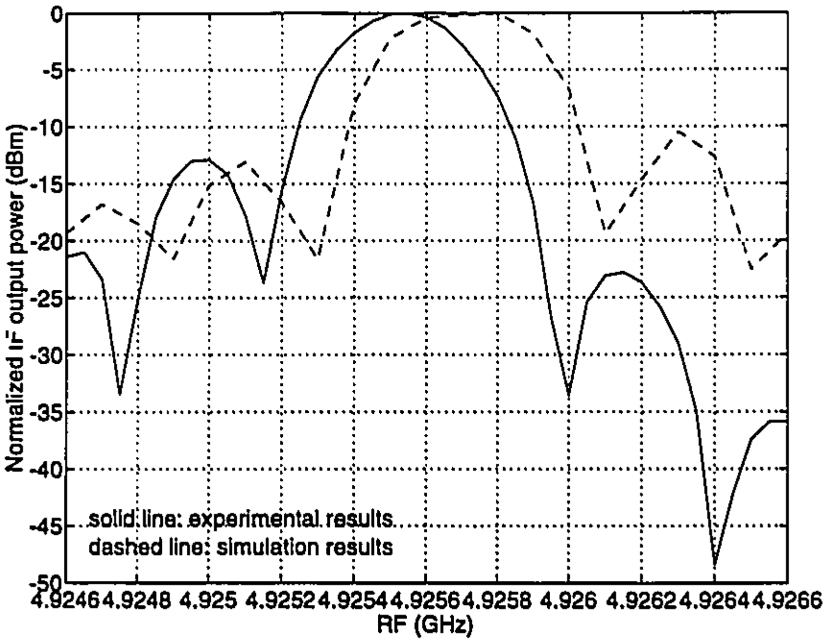

Figure 2.18: Comparison of experimental and simulation results of the DBF receiver

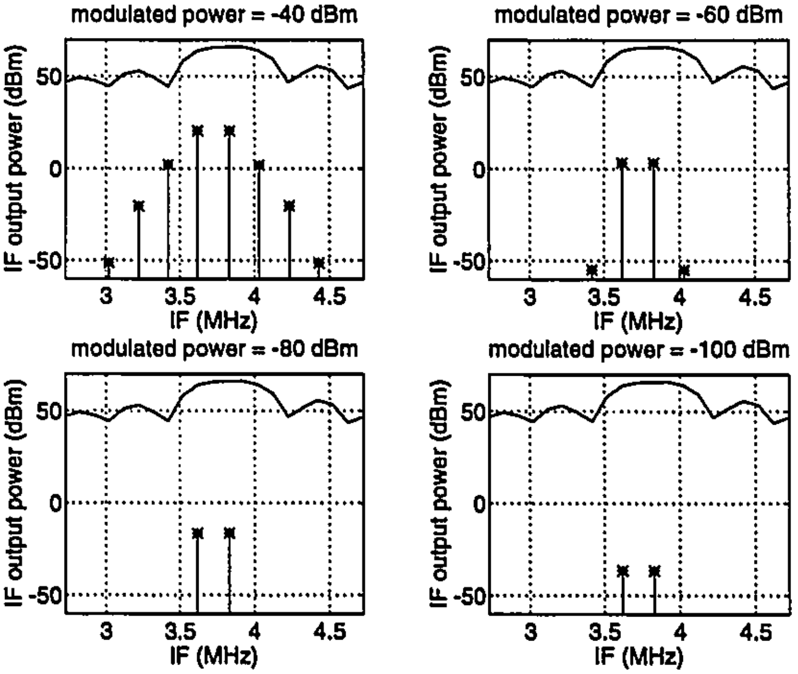

Figure 2.19: Spectrum analysis of the DBF receiver

sponse of the receiver, therefore, it can be seen clearly that how many intermodulation products in the signal bandwidth at different modulated power level.

OmniSys can perform system simulations based on component descriptions as simple as data taken from a manufacturing catalog or as complex as measured large-signal S-parameters.

2.5 Discussion and Conclusions

In this chapter, we have reviewed the potential elemental receiver architectures and their relative capabilities. The design and implementation of a double down conversion IF-direct sampling receiver has been presented. Simulations based on OmniSys were also described. It is believed that this receiver represents the state-of-the-art in readily producible receiver modules in which the components have been integrated and packaged to reduce module size for a relatively high performance DBF receiver. The parameter in which these receivers do not meet the requirements for many applications is the 360 KHz signal bandwidth. There was a trade in performance and cost that resulted in the decision to implement the 360 KHz signal bandwidth.

Phase-locked loops which can provide agile frequency control in the system and triple down conversion for high image rejection were not considered in our receiver, mainly because of cost considerations and research intention. Commercially available phase-locked sources can easily replace the local oscillator part of the receiver. Because phase and amplitude informations are critical in a DBF application, the system without AGC feedback was analyzed using OmniSys.

Chapter 3

Four-Element Integrated Receiver System for Digital Beamforming

3.1 Introduction

The operations involved in DBF are illustrated in Fig.3.1 for a linear array of elements with uniform spacing d, on which is incident a plane wave E from direction B. The received narrowband analog signals $v_n = A(t)e^{j(\omega t+\phi_n)}$, have equal amplitudes A but different phases $\phi_n = nkd\ sin\theta$, determined by their distances to a common phase front. They are down converted to baseband and the phases ϕ_n, essential for the later coherent summation, are maintained via the in-phase (I) and quadrature (Q) channels, which output the real and imaginary parts of the complex signals. These then are sampled at times t_μ, digitized, multiplied by complex weights w and summed to produce the antenna response

$$y(t_\mu) = A(t_\mu) \sum w_n e^{jnkdsin\theta}. \tag{3.1}$$

Here the factor A represents the received information and the sum represents the array pattern.

In this chapter, the design and implementation of a four-element linear array for

DBF system will be discussed. The key technique, self-calibration, in DBF system will be described and a new calibration structure for multilayer system will be presented.

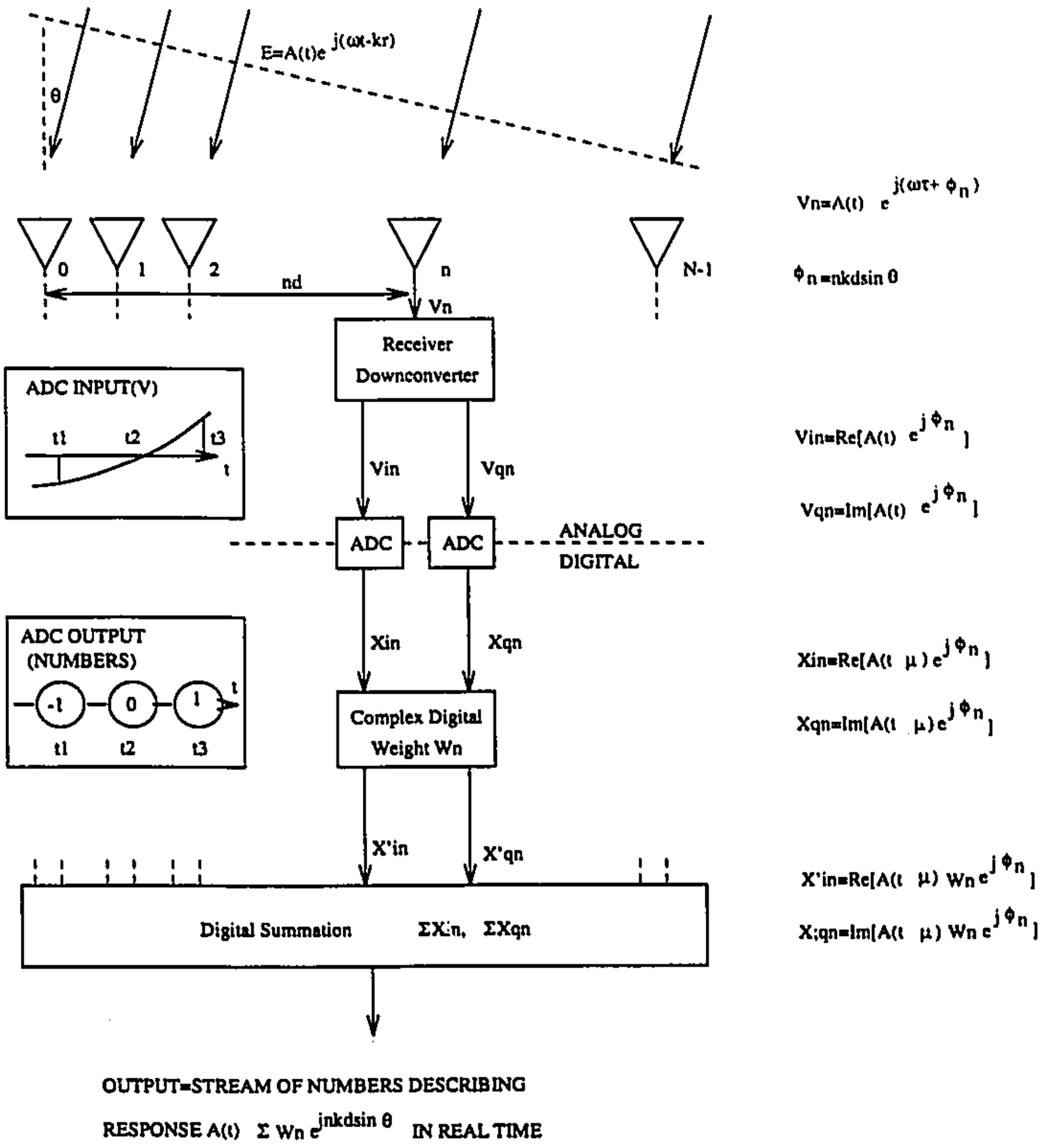

Figure 3.1: Digital beamforming operations

3.2 System Performance Requirements

Performance characteristics of potential tactical planar array surveillance systems are shown in Table 3.1. Standoff jammer type Electronic Counter Measure (ECM) threats require average sidelobe levels of -55 dB and peak sidelobe levels less -50 dB, over critical sectors in the scan coverage. Self screening jamming threats require adaptive cancellation techniques and a large receiver dynamic range (70 dB) to offset high jamming levels.

Table 3.1: Potential requirements for a surveillance radar

Parameter	Value
Array gain	38- 41 dB
Number of elements	2000 - 4000
Average sidelobe levels	$\prec$ -55 dB
Peak sidelobe levels	$\prec$ -50 dB
Azimuth coverage	±45° minimum
Elevation coverage	0 - 30° minimum
Dynamic range	70 dB minimum
Signal bandwidth	0.3 - 200 MHz

Signal bandwidth requirements range from 0.3 to 200 MHz. Long range surveillance requirements can be satisfied with signal bandwidths as low as 0.3 MHz; most track applications can be satisfied with bandwidths of 5 to 20 MHz. Bandwidths higher than 20 MHz may be needed to track targets in dense raids or to evaluate miss distances during intercepts; wide bandwidth, however, is usually only required over a limited range window. The widest signal bandwidth requirement is target identification where high range resolution is needed to obtain sufficient detail in the target signature; 200 MHz is the lower bound on bandwidths that would have any value in this application [15].

The reduction in bandwidth is particularly important in a digital beamforming array since it allows the A/D converters and digital beamformer parameters to remain unchanged from that used for the low bandwidth all range waveforms. The response of all of the circuits which precede the output of the mixer, however, must be phase and amplitude matched over the high bandwidth signal to achieve low sidelobes as in the case of conventional arrays. Time delay compensation may also be required across the array for high signal bandwidths to attain low range sidelobes for off broadside targets [15], [3], [6].

The elemental signal path includes a radiating element, an elemental receiver (r-f input to A/D converter output), an LO distribution system and all interconnecting signal cables in the digital beamforming array. An on-line calibration system is required to measure the elemental signal paths for component drift with temperature, operating voltage and time (component aging) in order to compensate the array. A comprehensive calibration system can reduce performance requirements on individual components and thereby reduce the fabrication cost of the array. Ideally the calibration system should include all of the elemental signal path components to allow the widest tolerance in the elemental signal path components. The calibration system itself must include provisions to compensate for insertion phase and gain errors within its signal paths and have a residual error significantly less than the error bounds of the receivers themselves.

3.3 Array Self-Calibration Techniques

3.3.1 Why is Self-Calibration Required?

There are two types of matching reuirements that impact antenna performance. The first is the conventional phase and amplitude match that sets the antenna sidelobes. Having a calibration input signal and a relatively easy means by which to measure the through phase and amplitude of the receivers, it is hoped that these errors can be reduced significantly. In fact, it is hoped that this might lead to reduced manufacturing tolerances resulting in less expensive fabrication costs followed by calibration after assembly.

The second matching requirement deals with phase and amplitude matching within the signal bandwidth of the receiver. This requirement sets the nulling performance of the array. For the majority of the components this is not a significant problem because the signal bandwidth is such a small percentage of the component's operating bandwidth. However, for the SAW filter this is not the case. In order to reduce the SAW manufacturers requirements, with very tight tolerances in center frequency for phase and amplitude ripple, a compensating calibration circuit is required to get good nulling performance for DBF applications.

Furthermore, insertion phase and amplitude of receivers are bias dependent. Many bias related errors are sensitive to operating temperature, supply voltages and component aging. It is necessary, therefore, to incorporate calibration equipment into a DBF array to permit the insertion phase and gain corrections to be updated whenever operating conditions change. Ideally, the array calibration approach should account for all errors in the array components and have an inherent error significantly less than the maximum acceptable channel insertion phase and gain error.

3.3.2 Different Self-Calibration Methods

The calibration technique which permits all component errors to be corrected is only achieved on an ideal pattern range or compact range facility with an equivalent far field source and an environment free of reflections and interference. The array calibration system, however, must be able to correct array transfer functions bias errors under field conditions with typical sources of interference and including non-ideal siting locations. Table 3.2 summarizes advantages and disadvantages of several calibration techniques for operational type array environments.

In Table 3.2, the two far-field calibration approaches permit the array radiating element characteristics to be included in the calibration. Both methods, however, are not suited to field equipment where frequent calibration is required. The airborne

Table 3.2: Array calibration techniques

Approach	Advantages	Disadvantages
Airborne Source	Includes array face environment. No added array complexity	Must accurately locate source. Logistically expensive.
Far-Field Source	Includes array face environment. No added array complexity.	Problems in siting source. Multipath effects. Not suitable for mobile DBF system.
Near-Field Source	Includes array face environment. No added array complexity.	Accurate source positioning required. Multipath effects.
Aperture Probe	Partial face environment. No added array complexity.	Accurate probe positioning required. Channel drift during measurement.
Aperture Face Coupling	Partial face environment. No added array complexity.	Large dynamic range required. Accuracy of end coupled data.
Precision Corporate Calibration Feed	Self-contained. High isolation between taps. Tap mismatch errors uncorrelated.	Array face errors not included. Calibration feed must be calibrated. Questionable long-term accuracy.
Precision Element Loop Calibration Feed	Self-contained. Self-test of calibration feed prots. Self-compensating on port outputs.	Array face errors not included. Feed input must have low VSWR. Mismatch errors at port couplers are correlated.

source is expensive to use and its angular position, relative to the array face, must be accruately known to derive phase calibration data. Suitable sites for a fixed far-field source are frequently not available at typical field sites; in addition, the need to enplace a far-field source as well as the DBF radar diminishes the radar mobility.

The near-field source calibration approach also permits the array element characteristics to be included. The position of the source must be accurately known in order to compensate the array calibration data (for the near field phase front distortion) and be able to use the compensated data to correct the elemental receiver insertion gain and phase. It will also be difficult, in most cases, to find locations in a field environment for the source where there are not significant multipath effects.

The aperture probe calibration approach overcomes many of the previous limitations in siting of the source. A precision positioning system is required, however, to accurately place the probe over each element grid location for an insertion phase and amplitude measurement. The drift in the insertion phase and gain of a receiver channel over the time required to move the probe over the array to calibrate the overall array decreases the accuracy of any measurement. With the both the far-field and near-field sources, it was possible to simultaneously collect calibration data from all of the array elemental receivers which eliminates drift as a factor in the measurement errors.

In the aperture face coupling approach, an array auxiliary element (or possibly several) is used as the source to couple the calibration signal into the active elements of the array. Since the calibration source is part of the array, the approach eliminates the logistic problems of the external source approaches while seemingly including the array face environment in the calibration path. This calibration approach is subject to error, however, because the mutual coupling between elements drops off for elements not near the source element resulting in a large variation, across the array face, in the signal level input to the elemental receiver channels. The elemental receiver channels must have a large dynamic range to have sufficient signal-to-noise ratio to calibrate the receiver with the lowest mutual coupling and not saturate the receiver which has the highest mutual coupling. The dipole radiating element is particularly difficult to calibrate by the aperture face coupling calibration approach since mutual coupling is relatively low for elements several wavelengths away. A second factor which decreases the accuracy of the aperture face coupling approach is that the test signal arrival angle is at end fire with respect to the array elements and not at the arrival angle which is normally used for forming the beams.

The two approaches using calibration feeds yield self contained calibration systems which can be accessed as frequently as needed when the array environment changes require a new set of calibration corrections (subject to operational constraints on time allocated for maintenance and calibration). The insertion phase and gain variations in the radiating element path, however, are not included in the calibration feed path which leaves a potential residual error in each receiver channel. It is imperative for low sidelobes that the radiating elements paths have essentially the same transfer function if there is no means of determining the variations in the radiating element path. The variations in the radiating element insertion phase and gain are reduced by close tolerances on the element size, position relative to the ground plane and array grid, and the dielectric properties of the materials making up the element (and radome cover); in addition, variations in the mutual coupling of the elements as a function of element location in the array are reduced by adding several rows and columns of dummy elements around the perimeter of the array to make the active element environmental more uniform across the array.

Even with the use of dummy elements and close control of the array radiating element construction and placement, the residual radiating element insertion phase and gain errors may be too large for desired level of sidelobes. It may be necessary to measure the transfer function of the radiating elements after the array is assembled and modify the calibration data measured for each elemental receiver by the complex array element transform to achieve the desired level of sidelobe control.

The precision corporate calibration feed has high isolation between the feed output ports; a reflection from a mismatch at the connection to the monitoring port on the elemental receivers is attenuated by the isolation between feed ports and has minimal effect on any other port output. The distribution loss for the calibration signal through the corporate feed is equal to the splitting loss for the number of taps plus a small loss for the attenuation of the feed and cable interconnections. The construction errors in the corporate calibration feed distribution will be too high to use the feed outputs without compensation corrections to measure the insertion phase and gain of the elemental receivers of a low sidelobe array. The corporate calibration feed has deficiency areas; an auxiliary calibration method is required to permit the calibration feed system to be monitored periodically. There must also be provisions, either through the feed system construction or a correction algorithm, to maintain accuracy over the operating temperature range. Differential phase errors may be avoided in the corporate calibration feed system by making all signal path lengths equal in length, have the same electrical sensitivity to changes in temperature and have a uniform thermal environment. The calibration feed then also may require recalibration of its transfer function from time to time to maintain system accuracy. In a large array with many calibration ports on a feed, the depth needed to fit the power dividers in may lead to a problem in the space available to fit the feed into the DBF array [15].

An alternative calibration feed concept, the precision element loop calibration feed, has features which eliminate some of the problems discussed in the previous paragraph. In our four-element linear array DBF system, we will use this calibration method.

3.3.3 Precision Element Loop Calibration Feed

The essential features of the precision element loop calibration feed are shown in Fig.3.2 which illustrates the feed applied to a linear array. The calibration source has two paths, which are T_{fk} and T_{bk}, to each elemental receiver coupling port. The calibration feed ports utilize a non-directional coupler to sample signals from the main transmission line of the feed; the coupling coefficient at a port is therefore identical from either path through the feed.

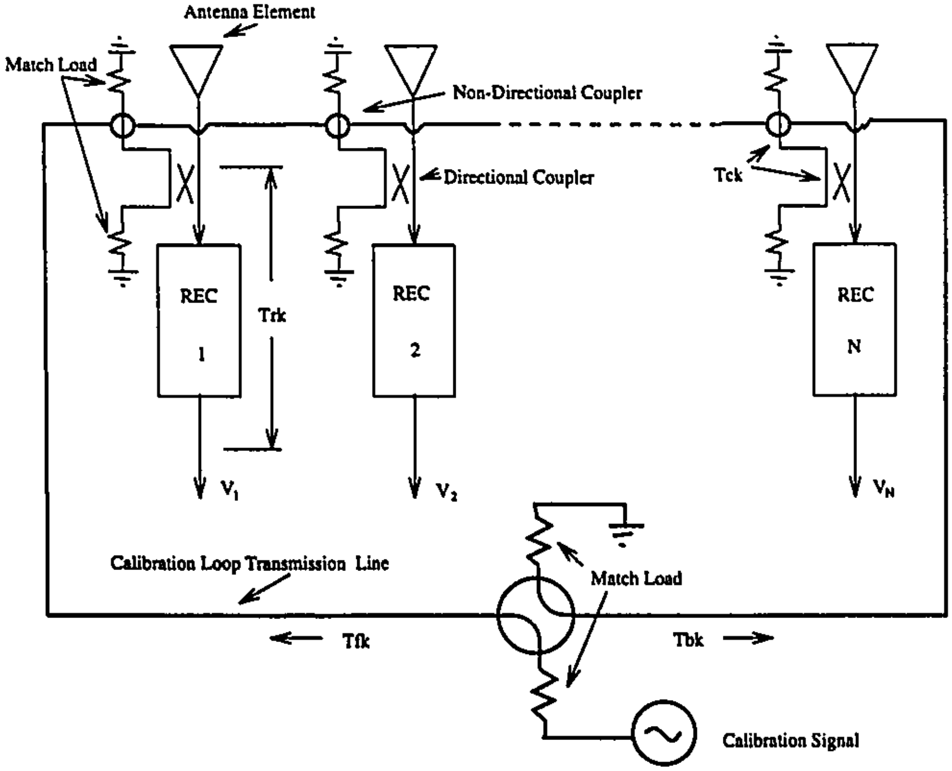

Figure 3.2: Precision element loop calibration feed method

Calibration of an elemental receiver channel requires two measurements with the loop calibration feed for each receiver channel. The calibration rest signal output from the receiver channel must be measured with the test signal successively fed from each side of the loop feed. The complex vector product of the two measurements represents the transfer function for the receiver channel. The insertion phase and attenuation of the entire feed is included in each pair of measurements when the vector product of the two measurements is used. Variations in the location of the calibration test port and the phase shift and attenuation of the signal through the feed cancel out when the measurements to an output tap from each side of the feed are combined. The calibration measurements are insensitive to thermal expansion changes in the feed.

The calibration measurement at each port of the feed is accomplished by setting the calibration switch in the direction to propagate V_{inc1} (the signal entering the left side of the feed) and then simultaneously measuring all of the elemental receiver outputs (V_{k1}) for each tap. This is closely followed by the second set of measurements of the elemental receiver outputs (V_{k2}) for each tap, the calibration switch set to propagate V_{inc2} into the right side of the calibration loop. The desired elemental channel transfer function (T_{rk}) is proportional to the vector square root of the complex product of the measurements ($V_{k1} \times V_{k2}$) and the port coupling constant K. The relationships between the measurements and the parameters of the loop calibrator are as follows:

Measure values

$$V_{k1} = V_{inc1} \times T_{fk} \times T_{ck} \times T_{rk} \tag{3.2}$$

$$V_{k2} = V_{inc2} \times T_{bk} \times T_{ck} \times T_{rk} \tag{3.3}$$

Calculated values

$$A_k = V_{k1} \times V_{k2} \tag{3.4}$$

$$T_{rk} = K_k \times \sqrt{A_k} \tag{3.5}$$

$$K1 = \sqrt{V_{inc1} \times V_{inc2}} \tag{3.6}$$

$$K2 = \sqrt{T_{fk} \times T_{bk}} \tag{3.7}$$

$$K_k = \frac{1}{K1 \times K2 \times T_{ck}} \tag{3.8}$$

The total port insertion loss (T_{ck}) is designed to be the same for each receiver port. The square root of the source voltage (K1) is a constant; the square root of the transfer independent of the port number. The calibration measurement is then (considering first order error effects) dependent only on having equal coupling through the single hole couplers and the calibration output port couplers.

A calibration error will result if there are uncompensated differences between the couplers on each elemental receiver port. Another source of calibration error is associated with mismatches on the main transmission line; the signal reflected to the source from any mismatch on the transmission line also couples to the ports between the mismatch and the source because of the non-directional couplers. A mismatch at the load end of the loop calibration feed produces a correlated error across all of taps in the feed.

3.3.4 Linear Array Calibration Loop

The structure of loop calibration feed for our linear array DBF system is shown in Fig. 3.3. The calibration feed ports utilize a non-directional single hole coupler, in a microstrip line feed implementation, to sample the signals from the main calibration line. The single hole coupler consists of a small aperture in the ground plane above the microstrip line which passes through the length of the feed. Energy would normally be uniformly coupled from the main line into the region around the hole on the top side of the coupling hole defined by the space between the ground planes. In order to confine the energy which is transmited from the main calibration line to the directional coupler, without affecting the antenna characteristics, a dielectric resonator (model D-8516 of Trans-Tech, Inc.) is used on top of the hole. The substrate used for the non-directional coupler is RT/Duroid 6006 of thickness 1.905 mm. In the channel, energy is propagated in two directions towards an absorptive load and towards a microstrip directional coupler which is the calibration output port. The directional coupler is at the same layer of feedline of the slot coupling patch antenna.

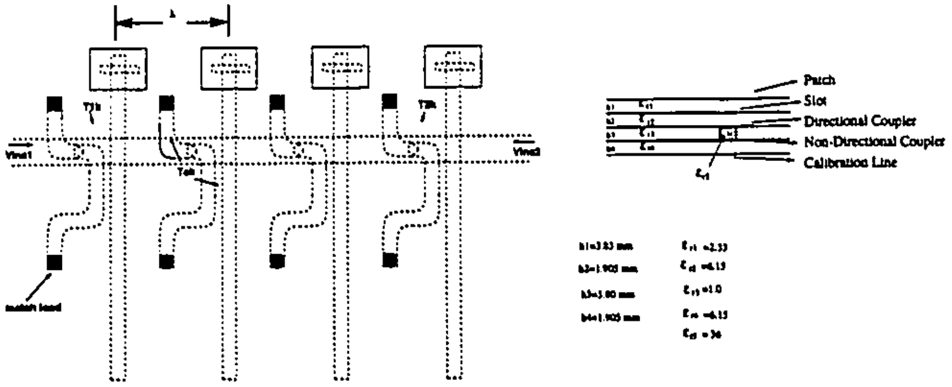

Figure 3.3: Calibration structure used in the four-element linear DBF system

A low coupling loss in the non-directional coupler is desirable to minimize calibration signal attenuation and interference from signal leakage; a high coupling loss is desirable to minimize reflections from mismatches at the coupling apertures. The designed coupling value for the non-directional single hole coupler is -25 dB; the coupling on the directional coupler is -20 dB. The total port insertion loss in the feed is then -45 dB plus a small loss for the energy coupled out of the other taps on the main feed line and the ohmic loss of the main calibration line.

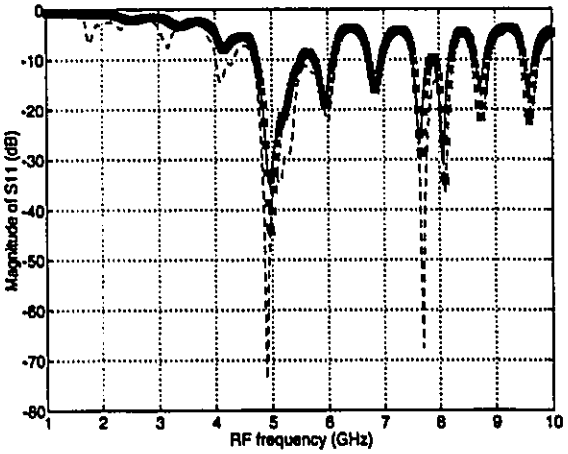

Figure 3.4: The influence of the calibration to the return loss of the antenna. solid line: the slot coupling patch antenna without calibration; star line: antenna with directional coupler; dashed line: antenna with both directional coupler and non-directional coupler

It is imperative to ensure that the antenna's resonant frequency remains unchanged when calibration is added, especially when the directional coupler and non-directional coupler are designed. Fig. 3.4 gives the experimental results which show how the influence of the calibration couplers to the return loss of the slot coupling patch antenna. We can see, in our design, the resonant frequencies of the antenna are almost keep the same both with calibration and without calibration.

3.4 System Architectures and Implementations

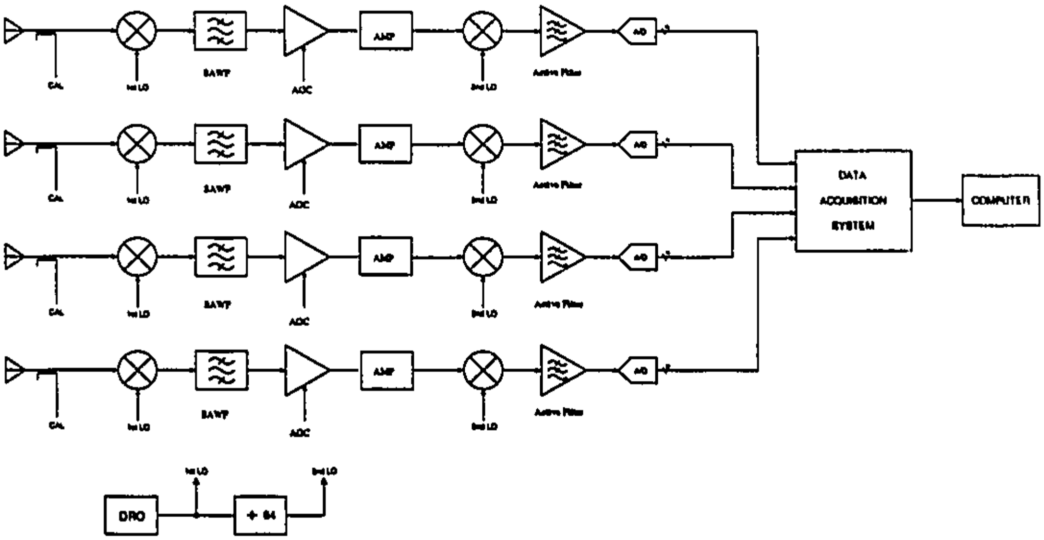

Figure 3.5: Block diagram of the 4-element array

Fig.3.5 shows the block diagram of a four-element linear array system for DBF applications. Basically, each receiver module in the array is the same as the receiver we described in the privous chapter. The A/D converter and data acquisition system used is the same one that was built for 32-element sampled aperture antenna system, which was developed at the Communications Research Laboratory, McMaster University [11]. The maximum sampling rate of the A/D converter is 50 MHz, the resolution is 8 bits and the maximum input voltage level of the A/D is 0.7 V in 50 Ω. The local oscillator part is the same as the one used for the receiver module, except we added the one-to-four Wilkinson power divider at both outputs of LO1 and LO2. Fig.3.6 gives the LO structure for the four-element array. The distance between adjunct elements was chosen to be λ, so as to accommodate the size of the receivers. The dimension of the whole array is $12 \times 24\ cm^2$, and the array has six mechanical layers which has been shown in Fig.3.7

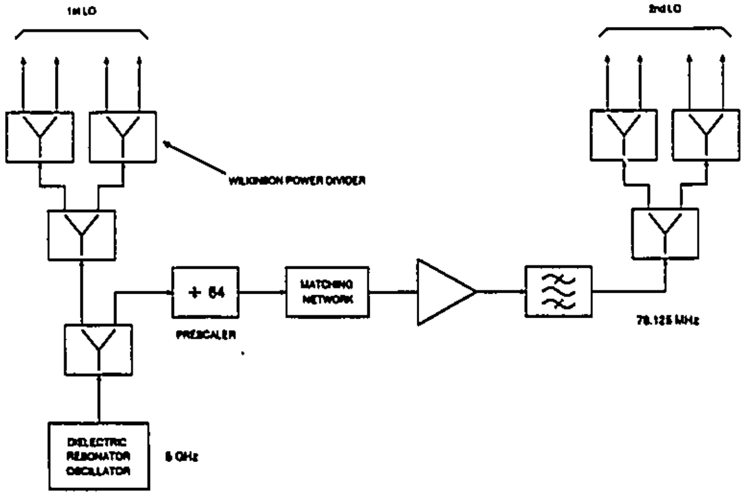

Figure 3.6: Local oscillator distribution for the four-element array

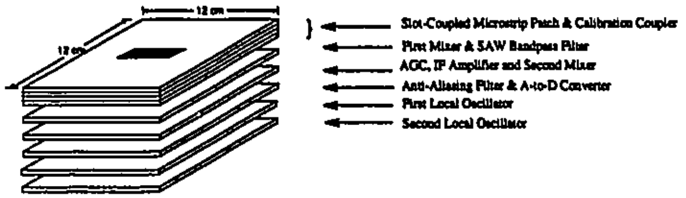

Elemental Integrated Receiver Module for DBF

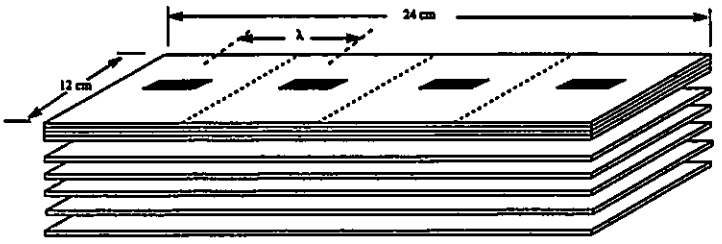

Four-Element Linear Array & Integrated Receiver System

Figure 3.7: Four-element array structure

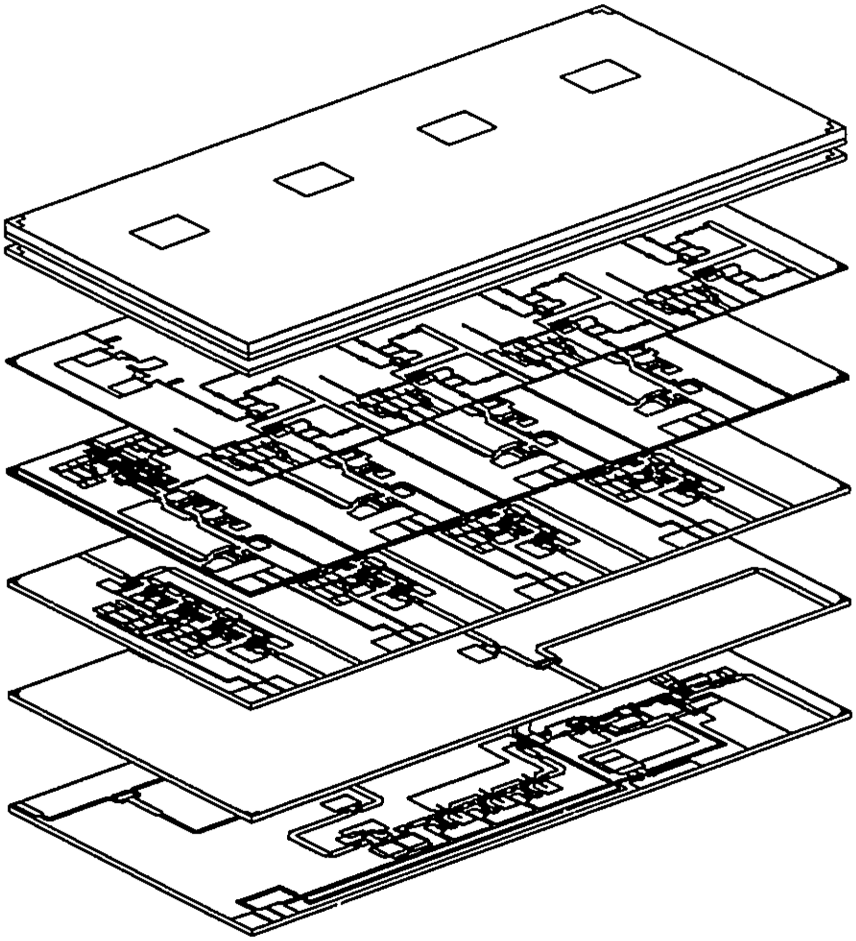

Figure 3.8: Layout of the Four-element array system

3.5 Experimental Results

The four-element linear receiver array system for DBF has been built. The layout of the system is shown in Fig. 3.8 which gives the details of each layer. Fig. 3.9 shows the photograph of the whole array. The system assessment at the first stage was concentrated on calibration and direction finding (DF) for one source measurements. The experimental setup was shown in Fig. 3.10. The source, local oscillator and sampling rate of the A/D converter were all kept coherent by means of a 5 MHz crystal oscillator.

During the calibration of the array, the signal source is configured to generate a

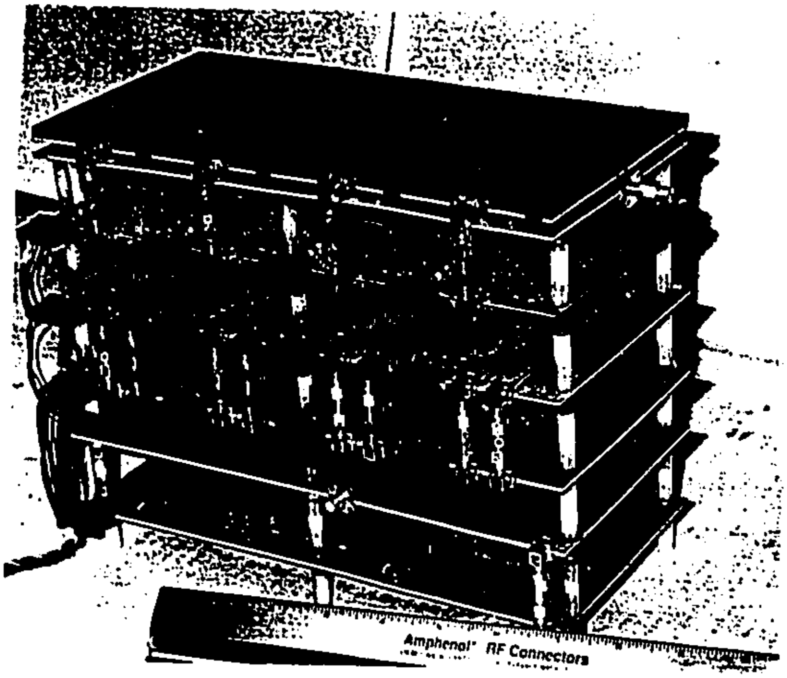

Figure 3.9: Photograph of the four-element array system

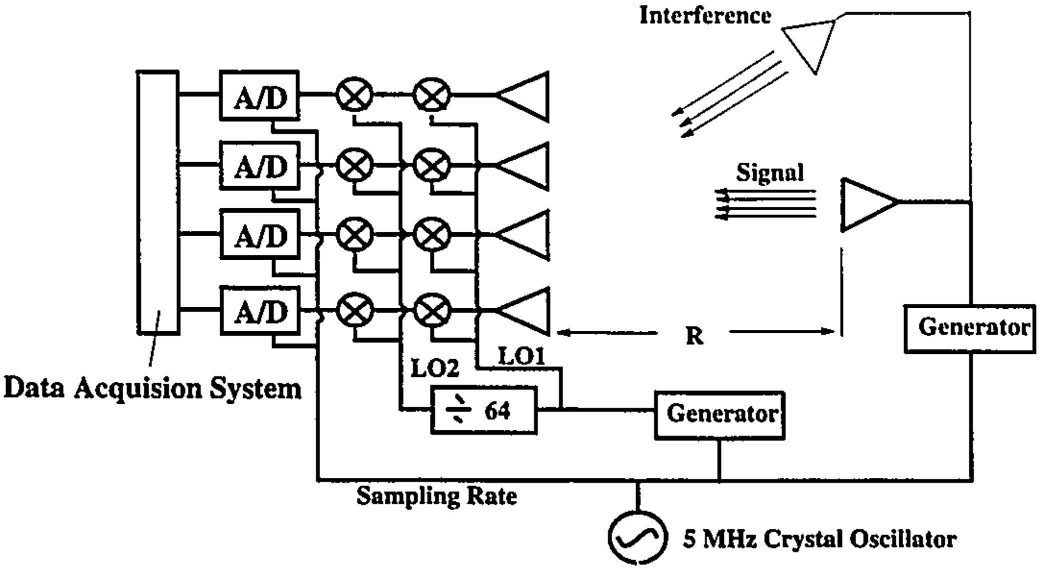

Figure 3.10: Setup for the array measurements

calibration pulse with a 10 KHz bandwidth and connect it to one side of the calibration feed. Each array calibration requires the collection of two sets of data; the first data set is taken with the calibration signal connected to the left side of the loop calibration feed. The second set of data is collected with calibration signal connected to the right side of the loop calibration feed. Two hundred and fifty six contiguous 8 bit samples are collected from each of the 4 receivers and stored in the buffer memory for each data block. After each data block has been collected, the contents of the buffer memory is formated into 8 bit bytes and transferred to the Unix Station for off-line processing.

The transfer function (insertion gain and phase) for a receiver channel is represented by a signal amplitude and phase value for the channel; this value is derived from the calibration signal measurements at the output of each receiver channel when the calibration signal source is connected to the left and right sides of the loop calibration feed as described in section 3.3.3. The complex square root of the product of the pair of I and Q samples, which was obtained directly by applying a Hilbert transform to the samples, is the signal amplitude and phase of the channel.

The first receiver channel is used as the reference channel. The insertion phase and gain of receiver channels 2 through 4 relative to receiver channel 1 is computed by dividing the signal amplitude and phase of channels 2 through 4 by the signal amplitude and phase of channel 1. A set of complex correction coefficients are computed which are used to correct the data from subsequent measurements.

In Fig. 3.11(a) is shown the amplitude distribution of a typical calibration function and in Fig. 3.11(b) is shown the corresponding phase. Figs. 3.12(a) and 3.12(b) show an example of the averaged amplitude and phase distributions of a set of calibrated data for the case of one incoming signal at boreside. For a perfect calibration, the amplitude at each channel is the same and the phase difference between two adjacent channels is also constant. However, it can be observed that there are residual errors after calibration. That is, the amplitude distribution is not perfectly uniform and the phase is not perfectly linear. This small amount of residual error will usually cause errors in DBF applications.

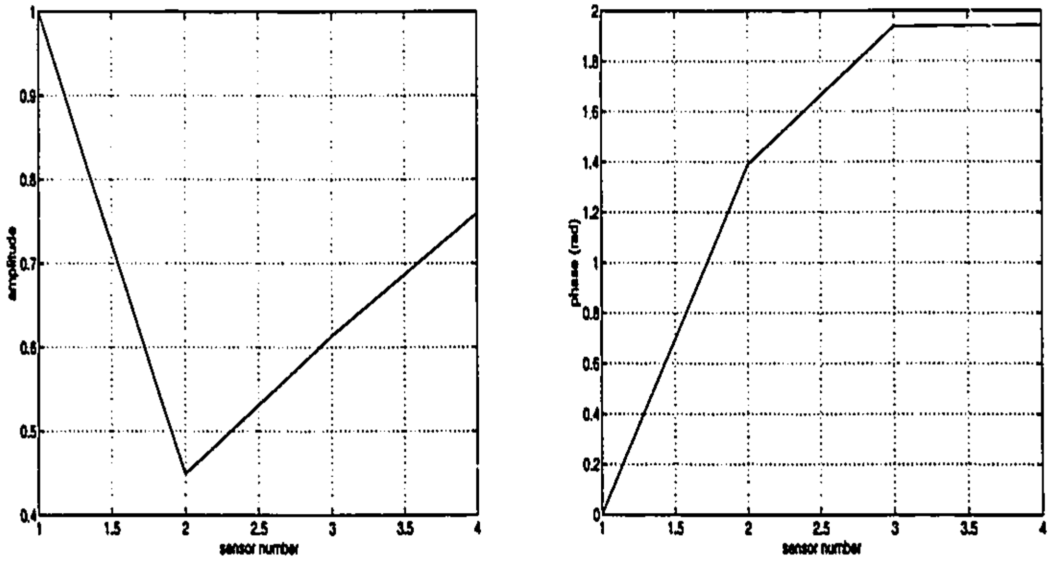

(a)

(b)

Figure 3.11: A typical signal distribution on each element of the DBF array before calibration; (a) amplitude distribution (b) phase distribution

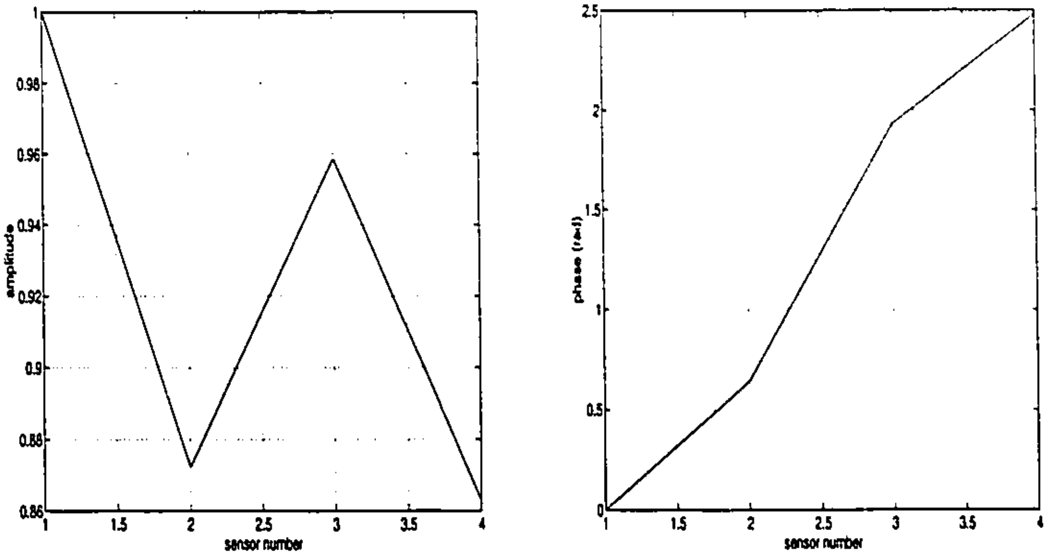

(a) (b)

Figure 3.12: A typical signal distribution on each element of the DBF array after calibration; (a) amplitude distribution (b) phase distribution

During direction finding measurements, data samples are collected from the array using the source located in the far field of the array as the input signal. In the off-line data process, each set of 4 I and Q data samples is normalized by the last set of calibration coefficients recorded at the operating frequency used to correct the data.

The 4 compensated and normalized receiver sample outputs from the 4 receiver channels are coherently combined by an FFT algorithm to produce the array factor response. A 2048 FFT point transform is performed to evaluate the array performance based on the real data. Fig. 3.13 shows the direction finding pattern for a source located at an angle of 21° from the boreside. Fig. 3.14 gives the DF pattern at an angle of -5.1° degree. Boths measurement results are good agreement with the real cases.

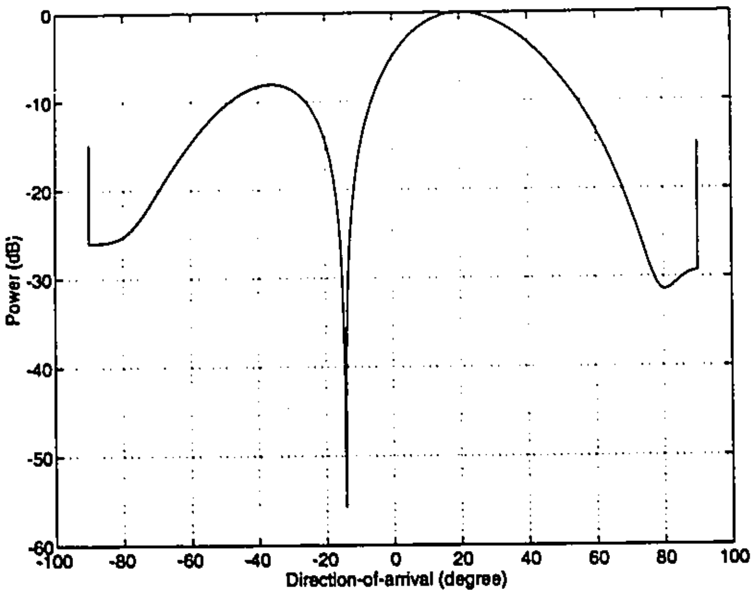

Figure 3.13: DFT pattern for a source located at 21° from the boreside

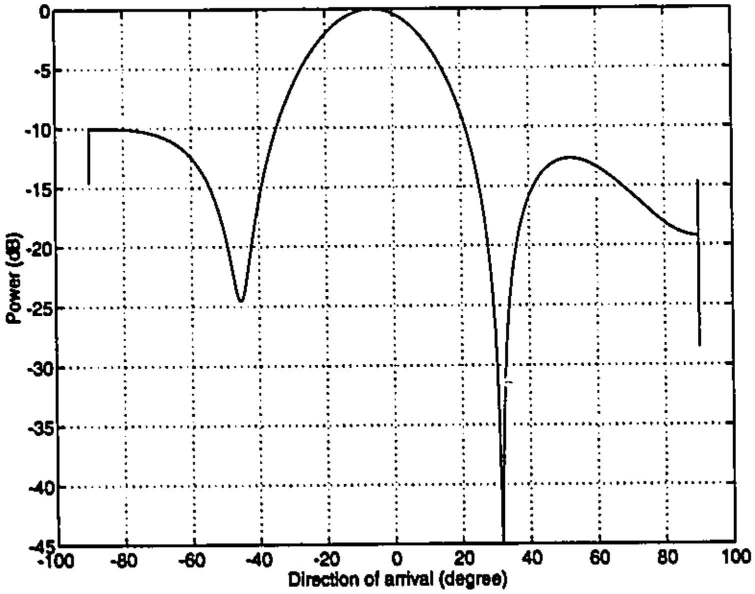

Figure 3.14: DFT pattern for a source located at −5.1° from the boreside

3.6 Discussion and Conclusions

The four-element linear array receiver system for DBF has been built and tested. The preliminary assessment of the system self-calibration approach indicates the measurement approach meets the objective of being able to compensate for mechanical and electrical variations in the receiver channels and changes in insertion phase and gain of the channels with temperature. The precision loop calibration feed had low construction errors with low phase and amplitude errors. The loop calibrator approach, however, is limited by the correlated error introduced into the calibration measurements by small mismatches at the couplers and at the terminations on the load ends.

Further experiments are being carried out to demonstrate the DBF receiver system to be used in adaptive beamforming in communications, two source direction finding and outdoor mobile communications. Based on the four-element array system, a larger linear array or planar array can be made easily by repeating the four-element array to get narrow main beam and low sidelobes.

Chapter 4

Investigation of Integrated Active Array Antenna in DBF System

4.1 Introduction

Fundamental contributions in the area of microwave and millimeter-wave antennas are currently being made by the design of integrated and monolithic active antennas. Integrated active antennas may be defined as radiating structures where the radiating elements, feed lines and associated components such as sources, detectors, phase shifters, and other control circuits are not clearly separated. In the case of monolithic active antennas, moreover, these components are printed on or deposited in the same substrate, usually in close proximity so that an antenna complete with its transmit, receive, and control circuits can be produced in a single fabrication procedure.

It is found that active antennas which exist at present can be divided into two classes depending on the arrangement of the active elements and the way in which they are connected: antennas with active elements directly built into the radiator or its immediate vicinity; and antenna arrays, with an active element in the channel of each radiator or a group of radiators.

In the literature much evidence is found proving that active antennas have many advantages, including electronic beam steering, fast adaptive beam forming/nulling, and multibeam operation. Furthermore, if distributed power amplifiers (transmit case) or low-noise amplifiers (receiver case) are integrated with the radiating elements, loss profile of the antenna can be precisely controlled. Additional advantages of such active antennas include the fact that in the transmit case, a high output power can be achieved by space combining the outputs of many low-power solid-state sources, and that graceful degradation will occur if some of the solid-state devices should fail.

An important consideration in the design of integrated antennas is the choice of transmission media, which must be amenable to the design of structurally simple radiating elements, and to the monolithic fabrication of solid-state components, which are easily connected to the antenna or their feedline. The microstrip medium lends itself to design where radiating elements, transmission lines, phase shifters, and possibly, receiver or transmitter circuits are integrated on the same substrate. However, the substrate may consist of several layers when circuits for more complex functions have to be accomodated and high-purity radiation patterns are required. Since the spacing between the elements of a DBF array must be of the order of half a wavelength to prevent grating lobes from appearing within the scan volume and since transmission-line lengths used for coupling in the calibration system are of the same order of magnitude in terms of wavelength, the surface area available on a single substrate for integrated components or circuits is limited, one must devise three-dimensional techniques that may be applied to integrate antennas so that sources, detectors, and control electronics may be placed behind radiating elements [51]. Circuits with radiating elements are collected into groups, or subarrays, on a common substrate, with microwave active devices to excite each subarray [52], [53], [54].

The crucial problem is the design and fabrication of the integrated active and control components in a form useful with the integrated antenna structure. In comparison to a monolithic active device, which may have linear dimensions of 1 μm of less, the antenna elements themselves are large, with critical linear dimensions of half a free-space wavelength or more. In the millimeter region this would be of the order of 1 to 10 mm. Such large range in critical dimensions leads to difficult manufacturing problems. Additional practical problems include techniques to remove excessive heat developed by active devices and mechanical stress on semiconductor layers. In addition, antenna elements require a certain clearance between each other, from transmission, bias,and control lines, and from other components to avoid pattern distortions and undesirable radiation coupling into nearby integrated components. These clearances become more critical as the overall performance of an array is increased, and a trade-off may become necessary between array performance and advantages in compactness, ruggedness, uniformity, and cost.

Current studies are usually directed at developing a proof-of-concept model to demonstrate a specific point with potentially important future implications, but an overall research pattern is not easily identified at this time. As dicussed earlier, we are only beginning to see a coherent approach to active array architecture and hence, active array element design. Instead of trying to present a general description of the field, an attempt is made in this thesis to indicate the possibility of using active antennas instead of passive antennas in DBF system, both for receiver and transmitter use. Active array antennas for other applications are also been addressed.

4.2 Design and Implementation of Active Antenna Elements

4.2.1 Design Procedure

A general active antenna element (shown in Fig. 4.1) can be devided into two parts: one is an active circuit part and the other is an antenna part. The antenna part also can be looked as a load of the active circuit.

A general design procedure used in this thesis is given as follows:

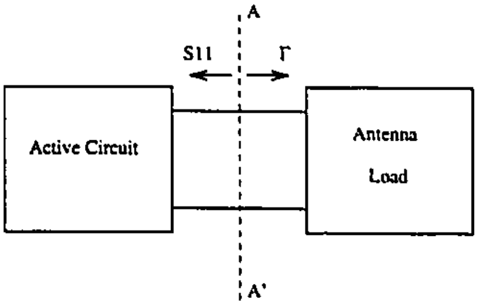

Figure 4.1: Block diagram of a general active antenna

- Design antenna:
  - use FDTD method to analyze the multilayer slot coupled patch antenna
  - use HP8510B to measure the reflection coefficient of the antenna
- Design active circuit:
  - select transistors: including S parameters, noise parameters, etc.
  - measure S parameters of FET by using TRL calibration
  - use EEsof's Academy to analyze the active circuits

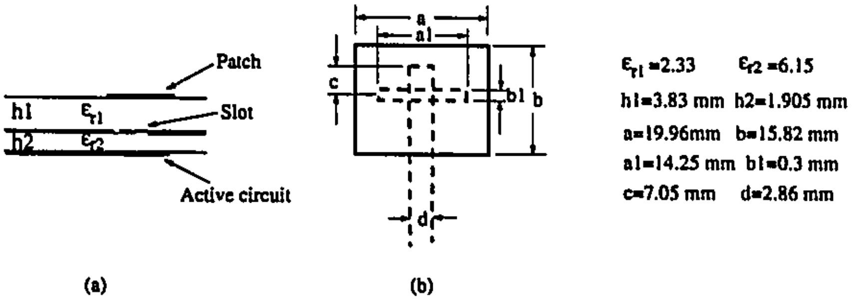

Figure 4.2: A multilayer slot coupled patch antenna

Whatever designs are used for active antennas, it is very important at the onset to carry out an accurate calculation for the input impedance of the antenna. In this thesis the antenna is a multilayer slot coupled patch. Because of the complexity of this structure, the Finite-Difference Time-Domain (FDTD) method is used to carry out the analysis [41], [55]. The simulations are then confirmed using an HP8510B network analyzer which is calibrated using the Through-Reflect-Line (TRL) technique [56]. Details of FDTD method will be described in Chapter 5.

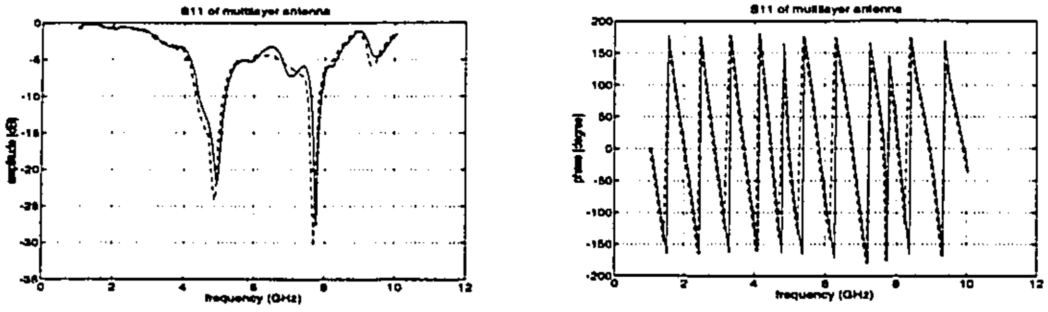

(a) (b)

Figure 4.3: Reflection coefficient for a multilayer slot coupled patch antenna, solid line: FDTD results; dashed line: experimental results

Multilayer slot coupled patch antenna was chosen through this thesis because radiation from the feed line does not affect the antenna pattern and the feed network need not be fabricated using the same substrate material as the antenna elements. FETs are chosen as active elements because they have higher efficiencies and lower noise figures than either IMPATT or Gunn diodes, and can be easily be incorporated into monolithic circuits.

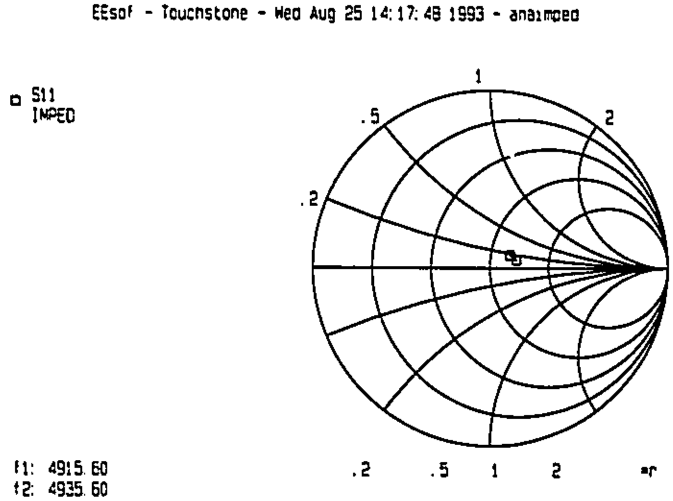

Figure 4.4: Input impedance for a multilayer slot coupled patch antenna

A multilayer slot coupled patch antenna, with dimensions shown in Fig. 4.2, has been developed for DBF applications at 4.9256 GHz. 3dB passband was from 4.3 GHz to 5.6 GHz, corresponding to a bandwidth of approximately 26%, and the gain of the antenna is 8.7 dB. Fig. 4.3 shows both the FDTD simulation results of the reflection coefficient and experimental results using TRL calibration. Input impedance of the antenna at 4.9256 GHz in Smith Chart is shown in Fig. 4.4.

After obtaining the correct input impedance of the antenna, the general rules applicable to amplifiers or oscillators can be used for designing the active antenna circuits. For the investigation of DBF applications, low noise amplifier design for receiver use and power amplifier design for transmitter use in DBF system have been studied. Furthermore, oscillator design for other applications are presented. Details of each design are given in the following sections.

4.2.2 Amplifier Module and Experimental Results

The design techniques are shown schematically in Fig. 4.5. For an amplifier, the power available from the source should be delivered to the input of the transistor through the input-matching network M_1. The output matching structure M_2 should also be designed to deliver the maximum power to the load. Usually, M_1 and M_2 are lossless network when the stability factor k is greater than unity. If k is less than or equal to unity, a stable amplifier will require some imput or output mismatch.

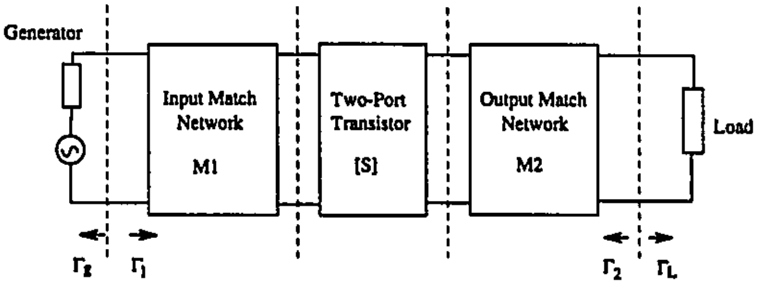

Figure 4.5: Block diagram of an amplifier

The amplifier module was designed in two ways; one as a low-noise amplifier for the DBF receiver and the other as a power amplifier design for the DBF transmitter.

Low-Noise Amplifer Module

For simplicity and ease of realization, a single-stage low noise amplifier configuration was chosen for the design of the receiver active antenna, considing the parameters at low noise bias, the design procedure considered is [57]:

- Design M_1 for low noise,

$$\Gamma_1 = \Gamma_{opt} \tag{4.1}$$

- Design M_2 for

$$\Gamma_L = S_{22}'^{*} = (S_{22} + \frac{S_{12}S_{21}\Gamma_{opt}}{1 - S_{11}\Gamma_{opt}})^{*} \tag{4.2}$$

- Design another input matching network M_1' between Γ_g and Γ_1 for

$$\Gamma_g = \Gamma_1 \qquad and \qquad \Gamma_g = \Gamma_{ant} \tag{4.3}$$

The input impedance of the radiating element, which was got accurately from FDTD results (shown in Fig. 4.4), was used as the generator impedance of the low-noise amplifier. The input matching network consists of two parts, one is for the generator impedance to the optimum low noise impedance of the FET and the other one is for the Γ_{opt} to S11 of the FET. The input and output matching networks of the amplifier were optimised by Academy software package of EEsof. Both input and output matching are accomplished by a T-type microstrip network. The transistor used in the design is model NE42484A low noise HJ FET ,with Vds=2V, Vgs=-0.6V and Ids=20 mA, from NEC. Fig. 4.6 shows the schematic diagram of the active antenna for receiver use. R1 and R2 are used for resistive loading (50 Ω - 150 Ω) to stabilize the amplifier since the initial k of the FET is less than unity at 4.925 GHz.

To judge the transmission performance of this active antenna element, a reference antenna, which is completely identical to the antanna part of the active antenna, has been built. Fig. 4.7(a) shows both the antenna receiving pattern of the active

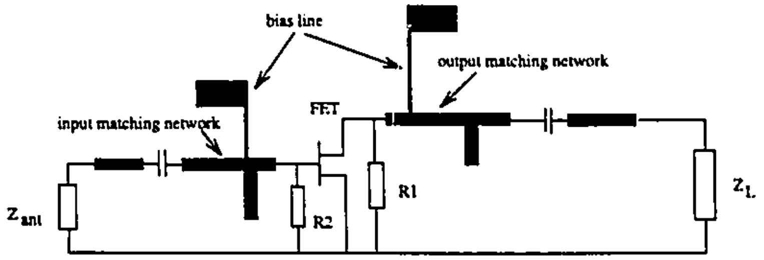

Figure 4.6: Circuit diagram of an active antenna element for the DBF receiver

antenna and the reference antenna on one side and a standard gain horn on the other side. Not too much difference can be seen between these two patterns. Extra gain about 9.89 dB at 4.9256 GHz was realized by the active antenna compared to the gain of the reference antenna. Extra gain changing with frequency was shown in Fig. 4.7(b).

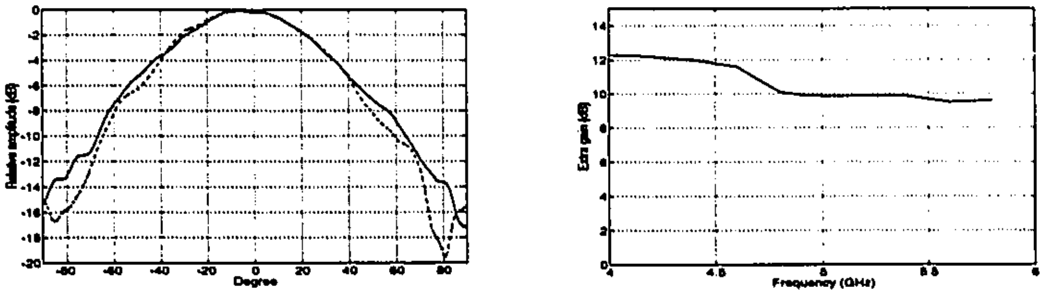

(a)

(b)

Figure 4.7: Response of the active antenna element for DBF receiver: (a)E-plane pattern, solid line: active antenna; dashed line: reference antenna, (b)relative gain improvement of active antenna

To measure the input noise figure of the active antenna, another reference antenna, which is exactly same as the active antenna except that the antenna part is replaced by a passive microstrip matching network to 50 Ω, has been implemented. Fig. 4.8 shows the noise figure measured by HP8970B noise figure meter. Combining the results shown in Fig. 4.7, we see the gain and the noise figure have the inverse relationship.

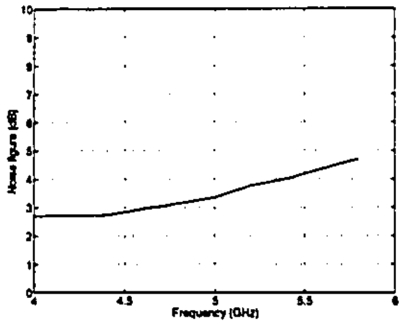

Figure 4.8: Response of the noise figure

Power Amplifer Module

The design of active transmitter antenna is quite similiar as the receiver antenna except that the input impedance of the multilayer antenna is a load instead of a generator in the design of active receiver antenna. In order to get the maximum power, the designing techniques are:

- Design M_2 for high power

$$\Gamma_2 = \Gamma_{ant}^* \tag{4.4}$$

- Design M_1 for

$$\Gamma_1 = S_{11}'^* = (S_{11} + \frac{S_{12}S_{21}\Gamma_{ant}}{1 - S_{22}\Gamma_{ant}})^* \tag{4.5}$$

The simulation of the amplifier circuit was done using EEsof's Touchstone software. The amplifier's topology used for the simulation is shown in Fig. 4.9. The Touchstone listing is given in Appendix B.

In the simulation, we have tried to include as much information as possible relating to the physical layout in order to get meaningful results for the real circuit. Shunt resistive loading (RS) and voltage-shunt feedback (RFB) are used to stabilize the amplifier. Conjugate match was involved in the optimization. Fig. 4.10 shows the simulation results of the transmitter antenna.

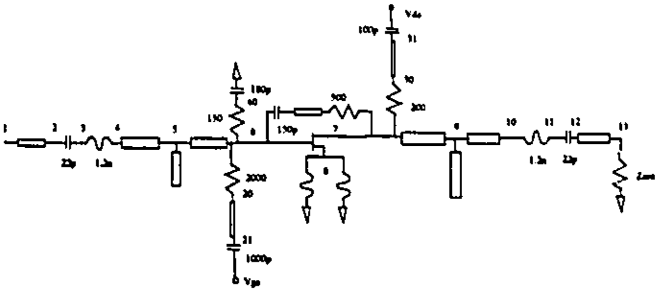

Figure 4.9: Topology used for simulating the active transmitter antenna using Touchstone

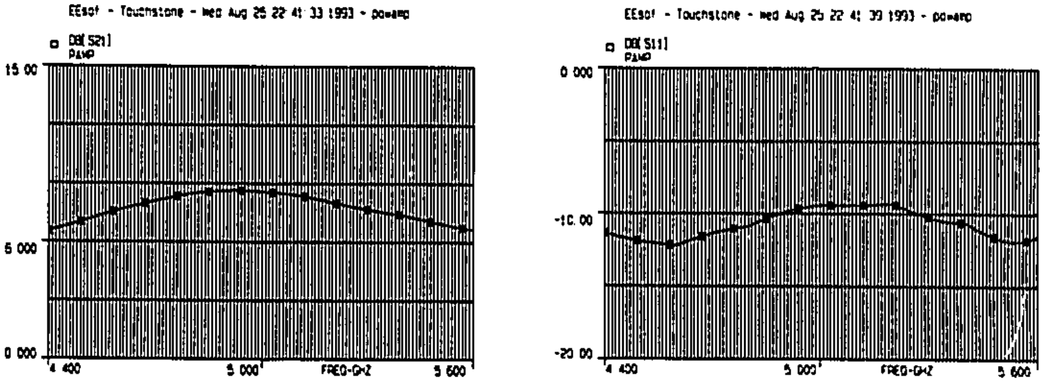

(a)

(b)

Figure 4.10: Simulation results of Touchstone: (a) gain, (b) S11

An active transmitter antenna using model NE800495-5 from NEC, which is basically the same as that used in the simulation, has been built. At 4.925 GHz, the total gain of 17 dB and output power of 29 dBm were measured using Friis transmission equation [58]. The structure of active antenna used was completely the same as the the one used in the receiver antenna.

4.2.3 Osciallator Module and Experimental Results

Osciallator module used for active transmitter antenna has also been developed in this work. The patch and the active circuit were fabricated on a 3.83 mm thick Duroid 5879 substrate with ϵ_r=2.33 and a 1.67 mm thick Duroid 5880 substrate with ϵ_r=2.2, respectively. A ground plane was located under a layer of foam, with ϵ_r =1.06 and a thickness of 10.96 mm. The source for the circuit was an NE71083 GaAs FET. The circuit is shown in Fig. 4.11.

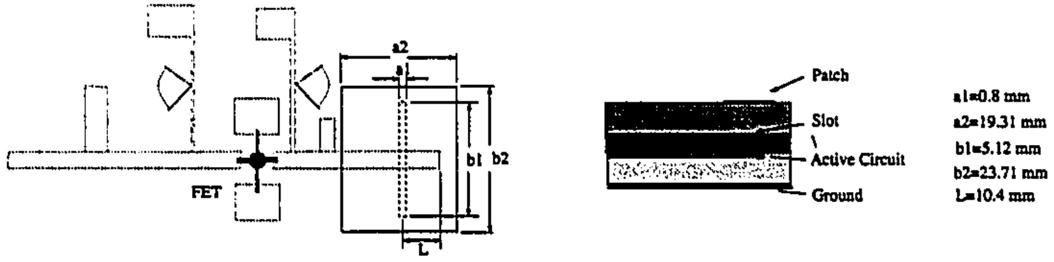

Figure 4.11: The structure used for the active oscillator antenna

The active antenna, viewed as an oscillator, was designed as a 'reflection amplifier'. Along the reference plane AA' (Fig. 4.1), S_{11} and Γ satisfy the oscillation conditions, which are

$$|\frac{1}{S_{11}}| < |\Gamma| \tag{4.6}$$

$$ang(\frac{1}{S_{11}}) = ang(\Gamma) \tag{4.7}$$

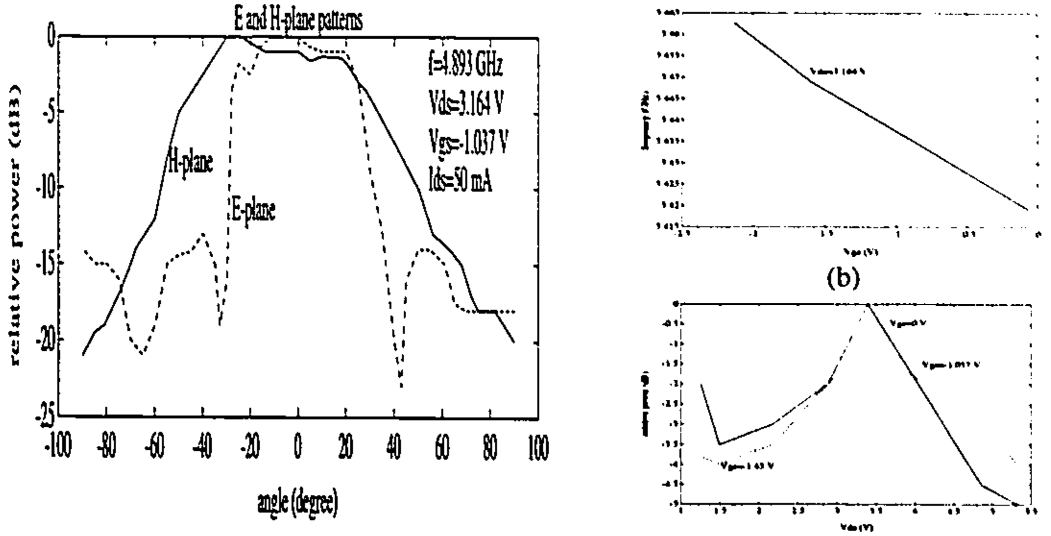

(a)

(b)

(c)

Figure 4.12: Measurement results of active oscillator antenna: (a) E- and H-plane patterns, (b) frequency vs. V_{gs}, (c) relative output power vs. V_{ds}

The quantities $1/S_{11}$ and Γ can be measured using the HP8510B. These parameters must satisfy the two stability criteria [38], [39] which are

- $1/S_{11}$ curves intersect the resonance circle, Γ, and inside the intersection the two curves travel in opposite directions with changing frequency;
- for optimum phase noise, the amplitude trajectory of $1/S_{11}$ at f_{osc} crosses the resonance loop (Γ) perpendicular to the tangent at the point of intersection.

The output power of the active antenna was measured using a horn antenna located at one end of an anechoic chamber with the active antenna located at the other end. The output power of the active antenna was measured to be 4.81 mW at 4.893 GHz. The sinusoidal output of the antenna was observed to be very stable with a clean spectrum. Fig. 4.12 shows the E- and H-plane field patterns for the active antenna and the output power and frequency versus bias.

4.3 Design and Implementation of Active Array Antennas

Recent developments in solid-state devices and microwave/millimeter-wave integrated circuits have made it possible to combine active devices with antenna elements to form active arrays. Many elements can be combined to build an active phased array or a spatial power combiner. The resulting active arrays should have many applications in radar, communication, and EM systems. It is believed that the active antenna, with low-noise amplifier module in receiver and power amplifier module in transmitter, will be finally used in DBF systems.

4.3.1 Four-Element Active Array Antenna

Based on a single active antenna element design, a new circuit array structure consisting of 4 symmetrical MESFETs, which are integrated with 4 slot coupled patch antenna to form a FET-active antenna, is now introduced.

Each element of the power combiner that we describe here can be thought of as consisting of two parts; the negative resistance element, which supplies energy to the circuit, and the resonant element, which provides the frequency selection. The negative resistance element consists of a FET with the gate and source terminated in the proper way, and the resonant element consists of the multilayer slot coupled patch antenna.

The oscillation condition for the circuit is given by [21], [38]

$$\Gamma_r \times \Gamma_d = 1 \tag{4.8}$$

where Γ_r and Γ_d represent the one-port reflection coefficients of the resonator and device, respectively. This expression is quite useful when dealing with multiple resonant structures such as the microstrip slot coupled patch antennas described in this thesis, since with these structures it is possible for the oscillation condition to be

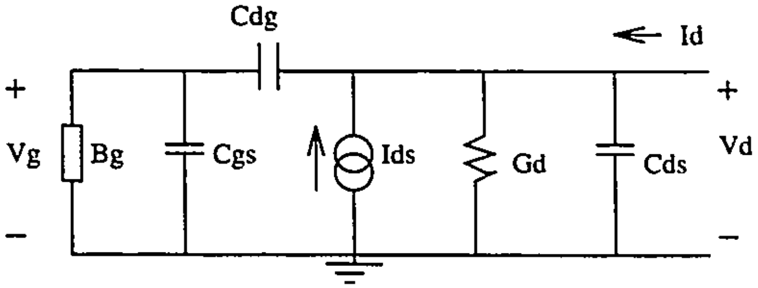

Figure 4.13: Equivalent circuit

satisfied at a number of different frequencies. The product in equation 4.8 is plotted on the Smith chart as a function of frequency, and wherever the curve nears the point $R = \infty$, jX=0, a possible oscillation is indicated.

The device used in our design is a GaAs MESFET. By properly terminating the gate and the drain of the MESFET, we may regard it as a one-port negative-resistance device by looking into the drain. Fig. 4.13 shows the simple equivalent circuit linear model of a common-source configuration. The drain admittance of the device can be expressed as:

$$Y_d = \frac{I_d}{V_d} = \frac{-g_m}{B_g + C_{gs}} + j\omega[C_{dg}(\frac{B_g + C_{gs} - 1}{B_g + C_{gs}}) + C_{ds}] \qquad (4.9)$$

Depending on the value of B_g, the drain admittance may contain a negative real part. In addition, since the MESFET has a Schottky barrier type gate, the value of C_{gs} may be varied by changing the dc bias applied to the gate. The output power and the operating frequency may be adjusted in this way too. In practive, an additional series feedback element may be added to the source to increase the instability as well as to provide for dc bias connections.

An X-band prototype circuit has been developed for operation at 8.7 GHz. The patch and the active circuit were fabricated on a 3.170 mm thick Duroid 5880 substrate with ϵ_r = 2.33 and a 1.905 mm thick Duroid 6006 substrate with ϵ_r =6.15, respectively. The FET for the circuit were 4 NE76038 GaAs MESFETs. The circuit configurations are shown in Fig. 4.14.

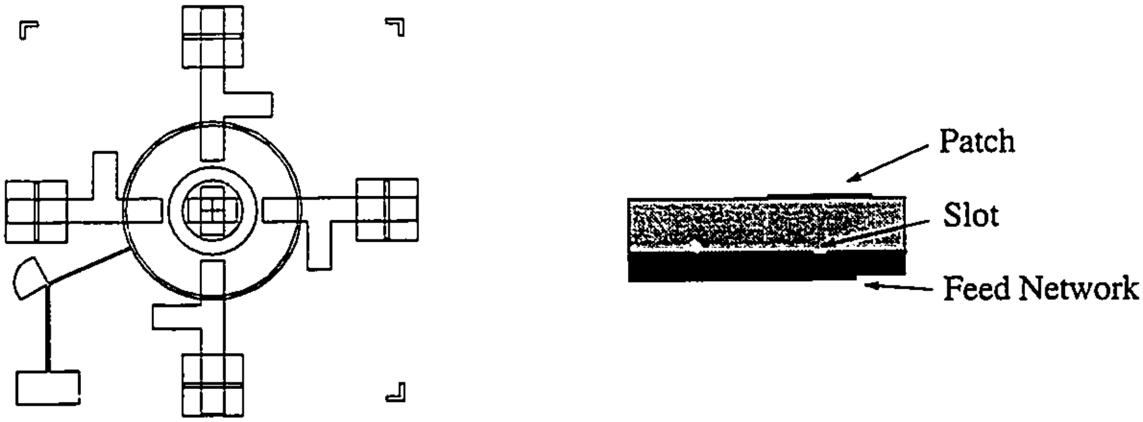

Figure 4.14: Four-element active array structure

Despite the fact that the design was based on only small-signal models, all the circuits oscillated within 4% of the design frequency.

For the prototype circuit, the maximum output power is 20.44 mW at 8.706 GHz with about 16 % dc-RF conversion efficiency. Fig. 4.15 gives the E-plane pattern for the active array. It is seen that the 3dB-beamwidth is approximately ± 15°. The antenna was designed to be strongly linearly polarized, with a measured axial ratio that is greater than 30dB. 100 MHz bias modulation and power variation with bias are also shown in Fig. 4.15.

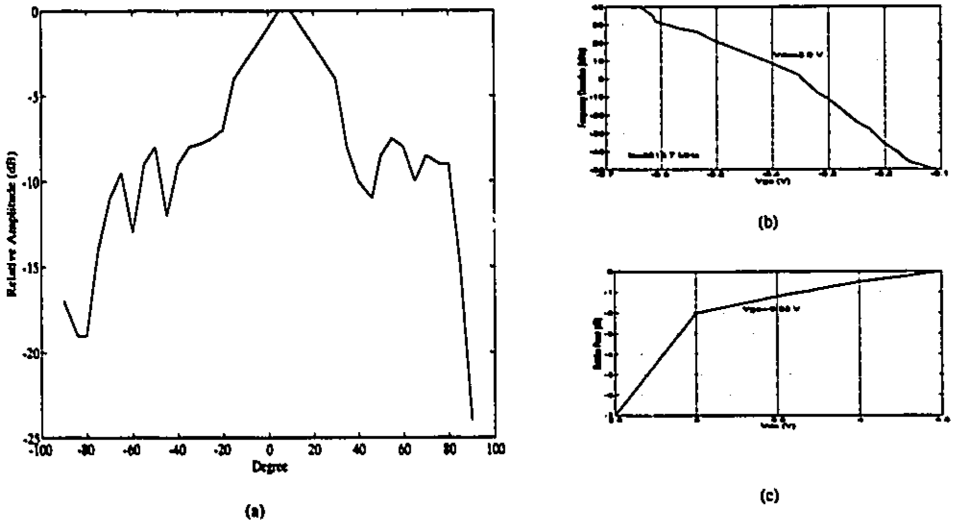

(a)

(b)

(c)

Figure 4.15: Experimental results of the active array antenna

Figure 4.16: Phase locking: (a) 10 MHz/div, (b) 100 KHz/div

Usually, some form of external injection-locking must be built into active antenna to ensure that the radiated signal is coherent. In our active antenna we do not require an external locking signal, because injection-locking is provided by the mutual coupling among the elements of the array. Experimental results are shown in Fig. 4.16. They show rather good performance for the active antenna.

4.3.2 Circular Polarization Design

By changing the feed network, we were able to design a circularly polarized active antenna array. To achieve circular polarization with the four-element array, the signals fed to one pair of diagonally opposing elements remained unchanged while the signals sent to the opposite pair was modified. The reflection coefficients at the slot coupling ports corresponding to the latter two antennas are optimized to have the same amplitudes but to have phases which differ by 90 degrees. In Fig. 4.17 is shown

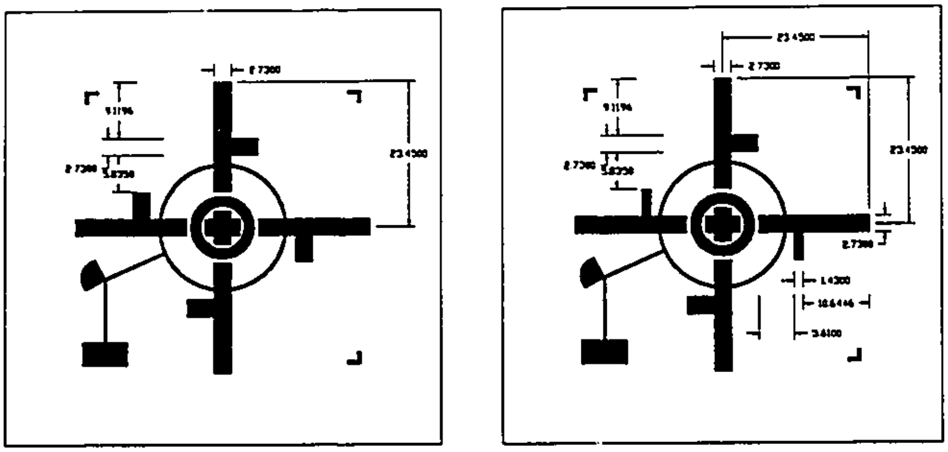

(a) (b)

Figure 4.17: Design of feed network for two types of polarization: (a) linear polarization, (b)circular polarization

the feed networks for the linearly and circularly polarized antennas. Using the feed network shown in Fig. 4.17 (b), we were able to develop a prototype antenna with a 2 dB axial ratio.

4.3.3 Dual-Mode Application

We have found that if the feed network is further modified so that the opposing elements of the array are designed to operate at one frequency and the other two are designed for another frequency, that a dual mode antenna can be achieved. EEsof's Touchstone software was used to optimize the performance of this antenna. Fig. 4.18 shows simulated results, which indicates two resonant frequencies, one at 8.7 and the other at 9.2 GHz. Tests on a prototype of this antenna showed good agreement between measurements and simulated results. Experimentally, it was found that the resonancies occurred at 8.741 and 9.242 GHz, respectively.

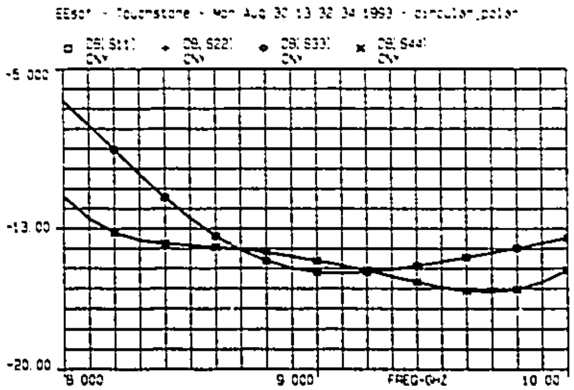

Figure 4.18: Simulation of a dual-mode antenna

4.4 Design and Implementation of Quasi-Optical Power Combiner Arrays

Recently, quasi-optical circuits, which integrate circuits and radiators, have been of growing interest for application to microwave and millimeter-wave systems [59]. Such circuits should be compact, simple, light and reliable so that they can be deployed in space, as well as being used for portable ground communications. In these circuits, an FET is frequently used as the quasi-optical source. However, it is not easy to generate high power from a single FET oscillator, especially at millimeter-wave frequencies. Therefore, if high power systems are to be developed in the future we must devise techniques for combining power from a large array of sources.

A number of active arrays, which were developed for generating power at high frequencies, have been reported in the literature. For example, in the case of arrays based on quasi-optical structure, there is the wave beam oscillator [53], the grid oscillator [60] [61], and the weakly coupled oscillator [62]. These arrays have been developed to demonstrate the efficiency of generating high powers by using a large number of solid state devices arrayed in a grid-like structure. In this thesis we present a new technique for coupling large numbers of active devices by using quasi-optical technology and a grid structure that is circular rather than rectangular.

We show the advantages of using the circular grid pattern. Using these concept, we achieved high efficiency in single phase locked mode of operation for an array of active devices [41], [42], [63].

4.4.1 Four-Element Spatial Power Combiner Array

Fig. 4.19 shows a four-element circular active antenna for spatial power combiner. It is fabricated on a Duroid RT/6010 with $\epsilon_r = 10.5$ and thickness 2.7 mm. The radial lines connected to the transistor drain and gate terminals support the flow of RF currents. The circular lines are used for DC bias and a ground for the source. The distance between adjacent drains, measured along the microstrip connecting lines, is approximately a half guide wavelength at the frequency oscillation. The gate lead is not connected to a DC bias. Its length is chosen so that the RF embedding impedance for the gate is inductive. The transistors were obtained from NEC and have the designation NE76038. Each element is designed as a negative resistance oscillator, and the slope at the resonant frequency is optimized to be positive for purposes of stability. Fig .4.20 shows the simulation results.

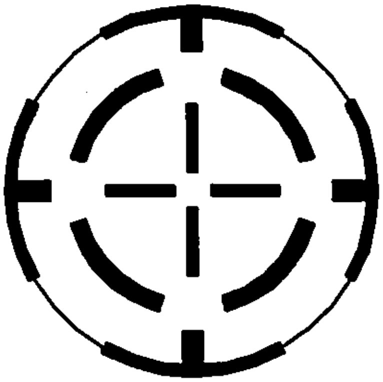

Figure 4.19: Topology for a four-element power combiner

The resonator configuration is shown in Fig. 4.21. This configuration is analogous to a maser, where the transistor grid, which is the active medium, is placed inside a Fabry-Perot resonator. The idea is that the transistors couple through one of the

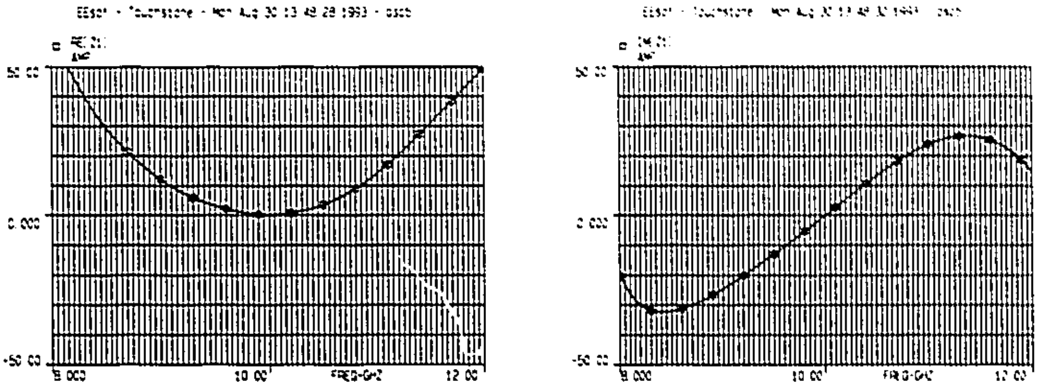

(a) (b)

Figure 4.20: Simulation results for a single active oscillator being developed as an element in a spatial power combiner

modes of the parallel plate cavity, principally by receiving a signal through the gate lead and radiating through the drain lead. One resonator plate is a metal mirror, and the other is a partially transparent reflector. In the actual array, the partially transparent reflector is just another microstrip substrate (RT/6010 with ϵ_r =10.5, thichness = 2.7 mm) with the copper removed from both sides. With the bias voltage set to 3.0 V and the separation between the two sheets equal to 30 mm, which is about λ at the oscillating frequency, the transistors oscillate at 9.636 GHz.

Varying the spacing between the substrate and the reflector shifts the frequency and the power. It is observed that the longer the spacing, the smaller is the variation in frequency as the spacing is changed. The power is seen to have a periodic variation as a function of the separation of the plates, as shown in Fig. 4.22. The largest effective radiated power that we measured was 70.63 mW at a spacing of 30 mm. The DC to RF conversion efficiency for this example is 39%. Fig.4.23 shows the measured far-field pattern. The cross-polarized signal is 26 dB down from the peak. We also noticed that the beam position can be shifted by tilting the reflector. The relation of the drain current, oscillating frequency and radiated power change with the bias Vds at a spacing of 30 mm is shown in Fig. 4.24.

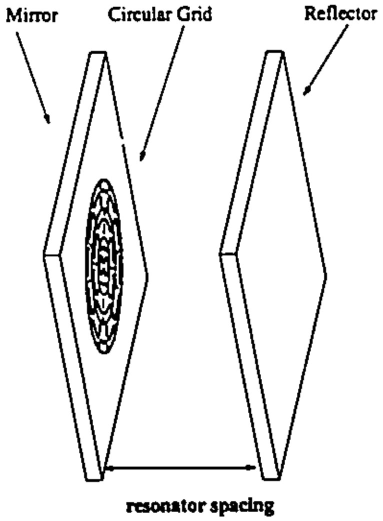

Figure 4.21: Resonator structure

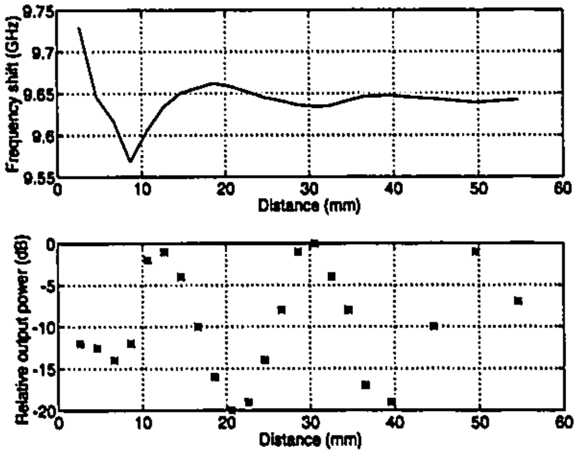

Figure 4.22: Experimental results for frequency and output power as a function of resonator sapcing

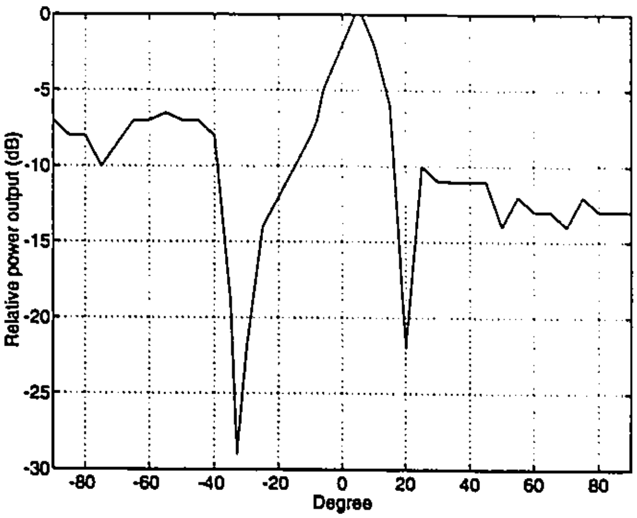

Figure 4.23: E-plane pattern of a spatial power combiner

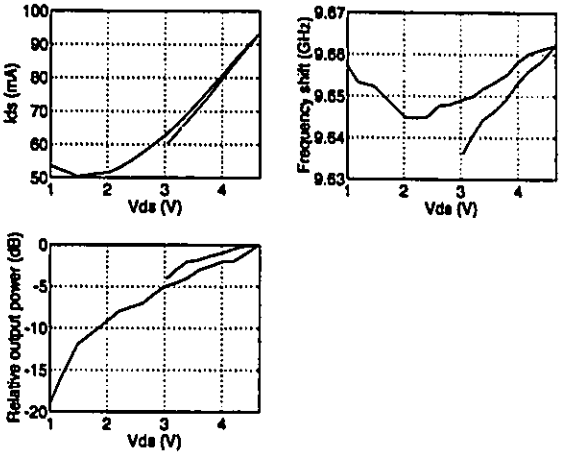

Figure 4.24: The drain current, frequency of oscillation and radiated power vs. drain bias

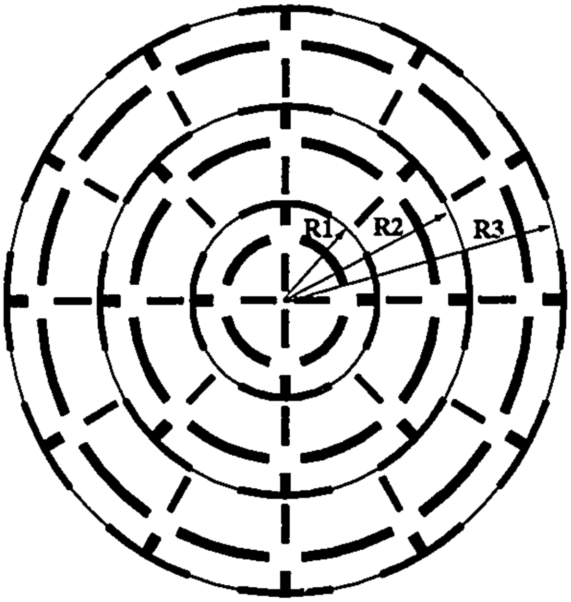

Figure 4.25: 24-element active spatial power combiner

4.4.2 Larger Active Antenna Array

The promising results obtained with the four-element active array, lead one to speculate that larger arrays could be developed using the same principles. A proposed 24-element active array structure, which consists of three concentric circles is shown in Fig. 4.25. The distance between adjacent drains, measured along the microstrip connecting lines associated with each circle, is the same as that used for the four-element active antenna, i.e. it is approximately a half guide wavelength at the frequency of oscillation. The radii of the circles are 9.55 mm, 19.10 mm and 38.20 mm, respectively. The bias for each circle is routed through the backside of the substrate. The FETs are NE76038 devices from NEC.

A 12-element antenna using two concentric circles was implemented and tested. The same resonator configuration used in the four-element design (shown in Fig. 4.21 was tested with the 12-element structure. Phase-locking is an important issue for a large active array. In this configuration, the phase-locking can be realized by either changing the bias voltage fed to the two circles or by changing the dimension of the

Figure 4.26: Locking sequence for the spatial power combiner (a) free-running (b) phase-locked

cavity. In this structure, either two separate biases or one common bias can be used. The use of separate biases provides for a larger dynamic range, while the use of a common bias leads to a simpler topology. Fig. 4.26 shows the spectrums for the phase-locked and free-running cases. The spectrum is similiar to an injection-locked spectrum, in which the different modes of the oscillator lock to one of the modes of the oscillator itself, rather than to an external locking signal.

Various characteristics of the spatial power combiner versus the dimension of the cavity are shown in Fig. 4.27. Whenever a free-running condition occurs, the frequency jumps from one to another. The output power varies periodically, with the output power reaching a maximum value when the dimension of the cavity is about 36 mm. In Fig. 4.28 is shown the variation of the frequency and the output power as a function of the value of the common bias for a fixed cavity dimension (36 mm).

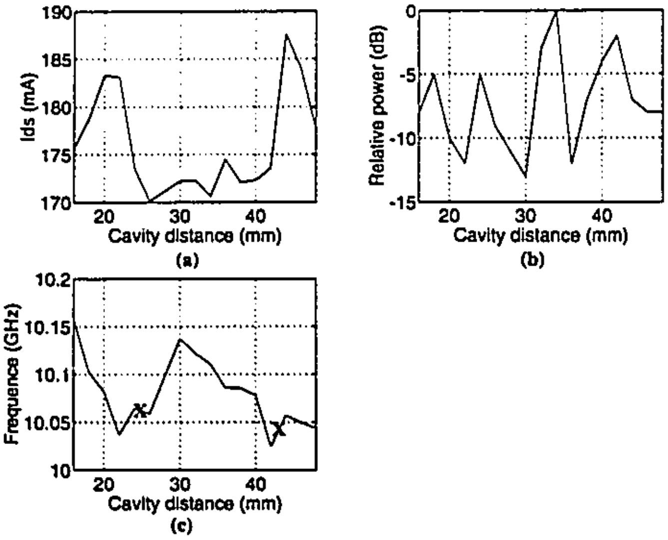

Figure 4.27: The drain current, frequency and power change with the cavity spacing. The symbol identifies the unstable points: (a) drain current vs. cavity spacing, (b) frequency vs. cavity spacing, (c) relative output power vs. cavity spacing

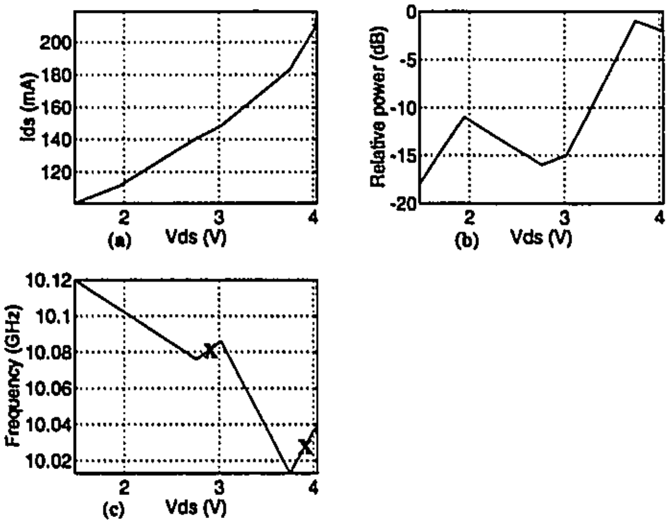

Figure 4.28: Drain current, frequency and output power as a function of bias. The points of instability are identified by X: (a) Ids vs. Vds, (b) frequency vs. Vds, (c) relative outout power vs. Vds

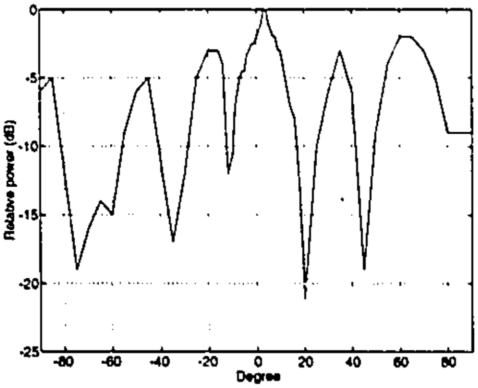

Figure 4.29: E-plane pattern of the 12-element active spatial power combiner

Finally, the output power and the DC-to-RF efficiency were measured and compared to the four-element case. Measured values for the DC-to-RF efficiency and the output power are 29.8% and 178 mW, respectively. Fig. 4.29 shows the pattern of the 12-element spatial power combiner. A larger spatial power combiner, based on these same principles, is now under development.

4.5 Other Applications and Possible Structures

Active antenna, as an alternative structure, also can be used as a spatial amplifier especially in wireless communication applications. As a relay, the integrated active antenna can receive the signal, amplify the signal and then transmit the signal. It is predicted that MMIC active antenna as a space amplifier will be widely used in wireless communications.

Based on the work introduced in this thesis, two possible structures for space amplifier have been suggested. A back-to-back integrated active antenna is shown in Fig. 4.30. The configration consists of two back-to-back active antennas, each side has one antenna. One is a receiver active antenna, which can be a low-noise amplifier module introduced in this chapter, and the other is a transmiter antenna, which is a power amplifier module also discussed in this chapter. Input and output signals can be easily separated by choosing opposite polarizations of the input and output antennas.

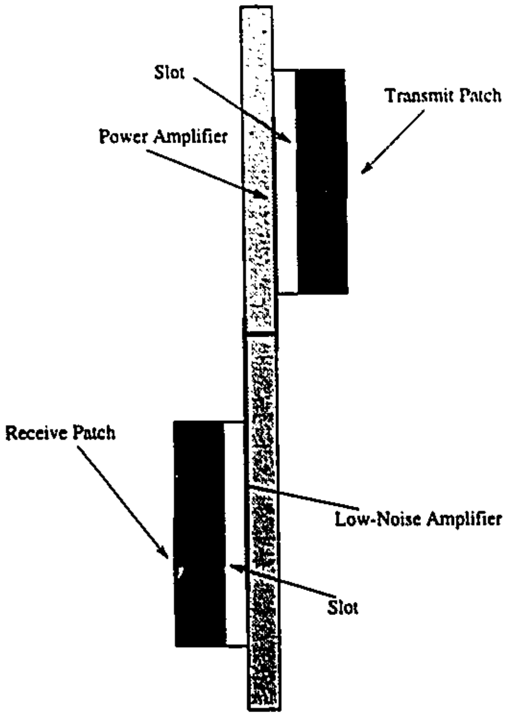

Figure 4.30: A back-to-back spatial amplifier structure

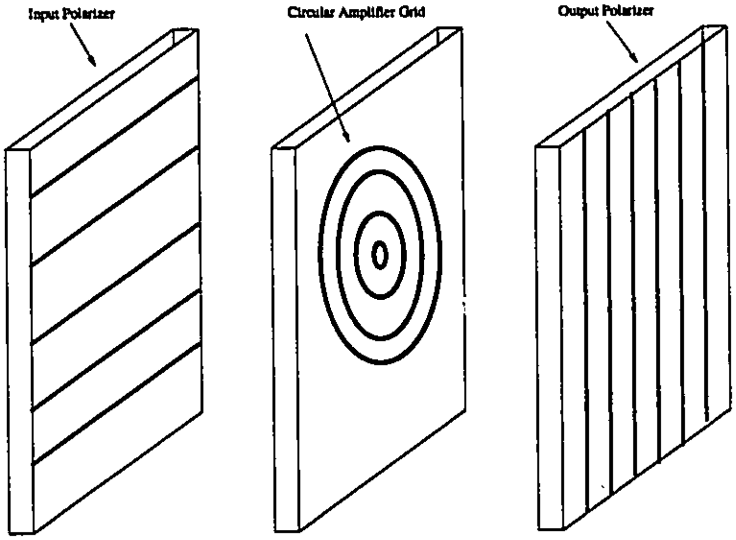

Figure 4.31: A circular grid spatial amplifier structure

The other possible configuration is shown in Fig. 4.31. This configuration is modified by the resonator structure for a spatial power combiner. In this structure, each element is designed as an amplifier and two reflectors are used as input polarizer and output polarizer.

These two possible structures are now being investigated.

4.6 Discussion and Conclusion

Several new active antenna elements and array structures, including receiver and transmitter active antannas for DBF applications, oscillator module for transmitter, array antennas for oscillators, spatial power combiners and spatial amplifiers, have been discussed. Mutual coupling between active circuits and the radiating elements were not considered in the analysis. The DBF system using active antennas instead of passive antennas is still under developing. Although all our realized active antennas were MIC structures, the design techniques and structures are equally well suited for MMIC designs.

Chapter 5

Investigation of Optical Control in DBF System

5.1 Introduction

Direct optical control of microwave semiconductor devices has been an area of growing interest since the beginning of the last decade. Various RF control functions including gain control of amplifiers, oscillator tuning, locking and frequency modulation, switching, mixing, limiting, phase shifting and attenuating have already been demonstrated [64].

Optical techniques have attracted interest largely because of their very wide bandwidth, the inherent high DC and reverse signal isolation between the control and RF signals, and their suitability for use with optical fiber links. Rapid advances in laser diode technology, particularly the increase in available modulation bandwidth and the possibility of integrating the optically controlled devices in microwave monolithic integrated circuit (MMIC) or optoelectronic integrated circuit (OEIC) forms, have stimulated further interest in optical control techniques. Optical control of microwave semiconductor devices has already been used in active phased array radars [65], [66] and is likely to find application in RF, microwave, and wide-band signal processing systems [64].

Future generations of phased array radar systems as well as satellite-borne communication systems might need several thousand active radiating elements to form a pencil beam for tracking and communications, respectively. In addition, advanced DBF array radars for tactical aircraft and satellite will require distributed transmitter-receiver modules constructed from GaAs MMICs and arranged in an antenna architecture. The beam steering in these arrays is done electronically or digitally by rapidly varying the relative phase of the radiating elements. This can be accomplished optically by using either a fiber optic link to carry digital commands to the MMIC phase shifters, or optical fibres to perform RF power distribution and phase shifting. Especially in DBF array, because each element consists of a whole receiver or transmitter, direct optical control, such as oscillator tuning, gain control, switching, mixing and channel balance, etc., can all be used in the array structures.

The work in this thesis is not to discuss the method of different optical control in DBF system, but to provide a full-wave analysis which can accurately predict the behavior of the optically controlled microwave devices; since up to now there is no physics-based full-wave analysis available in open literatures. Also, our work is mainly confined in passive optically controlled microwave devices.

The basic process in optical control of microwave semiconductor devices is the photoexcitation of carriers (hole-electron pairs) within the active region of the device when light with photon energy greater than the band gap of the semiconductor is absorbed. In a semiconductor waveguide, the main effect is to generate a photo-induced plasma and to change the photoconductivity, which modifies the complex dielectric constant of the semiconductor. Therefore, the absorption of the light changes both the resistive and the reactive behavior of the devices, the response time being governed by carrier dynamics.

This chapter will describe the first reported modified frequency-dependent finite-difference time-domain ($M(FD)^2TD$) method for the modelling of optoelectronic microwave semiconductor devices. The two major effects of a constantly illuminated semiconductor plasma which have been analyzed are : (i) the strong influence of carrier diffusion and recombination-generation processes on photoconductivity and (ii) the depth to which the plasma penetrates the device. Finally, examples of a two-dimentional optically controlled dielectric resonator(OCDR) [48] and a three-dimentional optically controlled coplanar waveguide [49] were analyzed.

5.2 Finite-Difference Time-Domain Method

5.2.1 General FD-TD Method

The finite difference time-domain (FDTD) method was first introduced by K.S.Yee [67] to solve electromagnetic scattering problems. Formulation of the FDTD method begins by considering the differential form of Maxwell's two curl equations which govern the propagation of fields in the structures. The media are assumed to be piecewise uniform, isotropic, and homogeneous. The structure is assumed to be lossless. With these assumptions, Maxwell's curl equations may be written as

$$\mu\frac{\partial \mathbf{H}}{\partial \mathrm{t}} = -\nabla \times \mathbf{E} \tag{5.1}$$

$$\epsilon\frac{\partial \mathbf{E}}{\partial \mathrm{t}} = \nabla \times \mathbf{H}. \tag{5.2}$$

To obtain discrete approximations to these continuous partial differential equations the centered difference approximation is used on both the time and space first-order partial differentiations. For convenience, the six field locations are considered to be interleaved in space as shown in Fig. 5.1. The entire computational domain is obtained by stacking these rectangular cubes into a larger rectangular volume. The advantages of this field arrangment are that centered differences are realized in the calculation of each field component and that continuity of tagential field components is

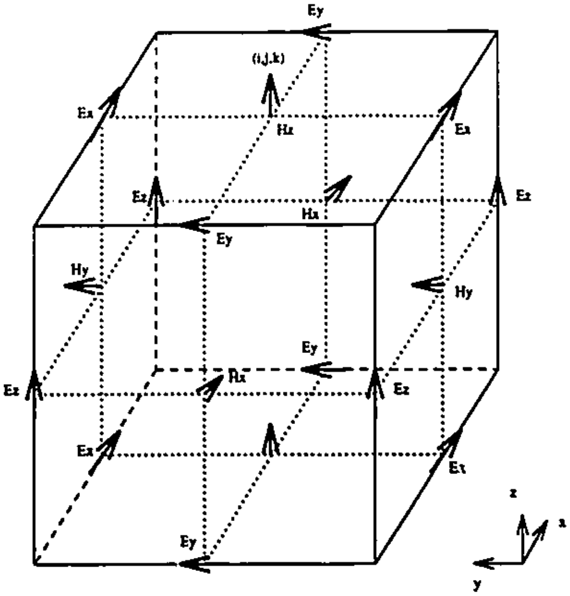

Figure 5.1: Field component placement in the FDTD unit cell

automatically satisfied. Using this field component arrangement, the above notation, and the centered difference approximation, the explicit finite difference approxizations to H_x and E_x are (H_y, H_z, E_y and E_z have the similiar forms)

$$\begin{aligned} H_x^{n+1/2}(i,j,k) &= H_x^{n-1/2}(i,j,k) + \frac{\Delta t}{\mu \Delta z}(E_y^n(i,j,k) - E_y^n(i,j,k-1)) \\ &\quad -\frac{\Delta t}{\mu \Delta y}(E_z^n(i,j,k) - E_z^n(i,j-1,k)) \end{aligned} \tag{5.3}$$

$$\begin{aligned} E_x^{n+1}(i,j,k) &= E_x^n(i,j,k) + \frac{\Delta t}{\epsilon \Delta y}(H_z^{n+1/2}(i,j+1,k) - H_z^{n+1/2}(i,j,k)) \\ &\quad -\frac{\Delta t}{\epsilon \Delta z}(H_y^{n+1/2}(i,j,k+1) - H_y^{n+1/2}(i,j,k)) \end{aligned} \tag{5.4}$$

The half time steps indicate that **E** and **H** are alternately calculated in order to achieve centered differences for the time derivatives. In these equations, the permittivity and the permeability are set to the appropriate values depending on the location of each field component. For the electric field components on the dielectric-air interface the average of the two permittivities, $(\epsilon_0 + \epsilon_r)/2$, is used.

Due to the use of centered differences in these approximations, the error is second order in both the space and time steps; *i.e.*, if Δx, Δy, Δz, and Δt are proportional to Δl, then the global error is $O(\Delta l^2)$. The maximum time step that may be used is limited by the stability restriction of the finite differrence equations,

$$\Delta t \leq \frac{1}{v_{max}}\left(\frac{1}{\Delta x^2}+\frac{1}{\Delta y^2}+\frac{1}{\Delta z^2}\right)^{-1/2} \tag{5.5}$$

where v_{max} is the maximum velocity of light in the computational volume.

The FDTD method has been widely used for solving electromagnetic problems. The popularity of the method is due mainly to the following two reasons. First, it can be easily applied to very complex structures which may be very difficult to solve using other analytical or numerical methods. Second, to get the frequency domain results over a long frequency spectrum, only one computation is required using the FDTD method, while for the frequency domain methods the results are obtained one point at a time.

5.2.2 FD-TD Method for Analysis of Different Dielectric Resonators

Dielectric Resonators (DRs) are the basic constituent elements of microwave integrated circuits. The accurate study of DRs using different numerical approaches is one of the most improtant topics in microwave circuits. The current cut-and-try cycles in the design of DR integrated circuits will be greatly reduced if the resonant frequencies and spatial field distribution of the DRs can be obtained with certainty.

In this work, a numerical procedure based on the FDTD method and Mur's absorbing boudary condition, is used to calculate the resonant frequencies for the $TE_{o1\delta}$ mode of open axisymmetric dielectric resonators. The DRs discussed here consist of semi-open DR, DR with tuning screw and multilayer structures [43], [44], [45].

The generalized dielectric resonator under investigation is shown in Fig.5.2, where the relative dielectric constant of DR is ϵ_r. The structure is assumed to be in an open

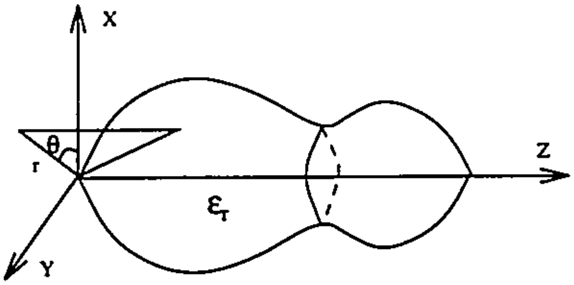

Figure 5.2: Gemetry and cylindrical coordinates for a body of revolution

environment, that is around the DR, free space is assumed to extend to infinity.

The Maxwell equation governing the solution of this problem are

$$\frac{\partial \mathbf{E}}{\partial t} = \frac{1}{\epsilon_i} \nabla \times \mathbf{H} \tag{5.6}$$

$$\frac{\partial \mathbf{H}}{\partial t} = -\frac{1}{\mu_0} \nabla \times \mathbf{E} \tag{5.7}$$

Where i=1,2 represents the DR and the free-space region, respectively. At the interface of the two regions, the field continuity conditions are enforced.

For the uniqueness of the solution of these Maxwell equations, the following conditions must be satisfied:

a) The initial condition for the fields must be specified on the whole domain of interest; that is, E(r, t=0) and H(r, t=0) must be given everywhere inside the computation domain.

b) The tangential components of E and H on the boundary of the domain of interest must be given for all $t > 0$.

Dielectric resonators of cylindrical shape which were excited in the $TE_{01\delta}$ mode, were used in most of the DR applications. For simplicity, only the $TE_{01\delta}$ mode is discussed.

Maxwell's equations in cylindric coordinate system, for $TE_{01\delta}$ modes, can be discretized as:

$$\begin{aligned} E_\theta^{n+\frac{1}{2}}(i,j) &= E_\theta^{n-\frac{1}{2}}(i,j) + \frac{\Delta t}{\Delta z \epsilon_i}[H_r^n(i,j+\frac{1}{2}) - H_r^n(i,j \\ &\quad -\frac{1}{2})] - \frac{\Delta t}{\Delta r \epsilon_i}[H_z^n(i+\frac{1}{2},j) - H_z^n(i-\frac{1}{2},j)] \end{aligned} \tag{5.8}$$

$$H_r^{n+1}(i,j-\frac{1}{2}) = H_r^n(i,j-\frac{1}{2}) + \frac{\Delta t}{\Delta z \mu_i}[E_\theta^{n+\frac{1}{2}}(i,j) - E_\theta^{n+\frac{1}{2}}(i,j-1)] \tag{5.9}$$

$$H_z^{n+1}(i+\frac{1}{2},j) = H_z^n(i+\frac{1}{2},j) - \frac{\Delta t}{\mu_i \Delta r r_{i+\frac{1}{2}}}[r_{i+1}E_\theta^{n+\frac{1}{2}}(i+1,j) - r_i E_\theta^{n+\frac{1}{2}}(i,j)] \tag{5.10}$$

In a practical implementation, an absorbing boundary condition [4] is used at the surface S_{out}. Here k is a constant, which is chosen as 0.65.

$$E^n(M,j) = E^{n+1}(M-1,j) + \frac{1-k}{1+k}[E^{n+1}(M,j) - E^n(M-1,j)] \tag{5.11}$$

Assume that at t=0, an abrupt field excitation is introduced (for instance, zero everywhere except at some localized points) which in turn excites a large number of modes. Using the above algorithm, the resonant frequencies can be obtained by reading the peaks in the spectrum diagram, which is obtained by taking the fourier transform of the computed time domain response [44].

The FDTD method has a number of advantages which have been discussed in many papers. However, it has one significant disadvantage which is that it requires a very long computation time for extracting the resonant frequencies from the FDTD results. For example, in the case of the problem discussed in [68], the time iteration N has to be as long as $N = 2^{16}$. We introduce digital filtering and modern spectrum estimation techniques into FDTD method to overcome the above limitation. Detailed procedures were given in [46], [47].

5.2.3 Simulation and Experimental Results

Using the above efficient FDTD method coupled with digital filtering and the MUSIC algorithm, we analyzed several DR structures of practical importance, semi-open DRs, tuning screw DRs and multilayer DRs.

A semi-open dielectric resonator coupled to a microstrip substrate was studied. The parameters for the analysis are given in Fig. 5.3. The parameters used for this analysis are

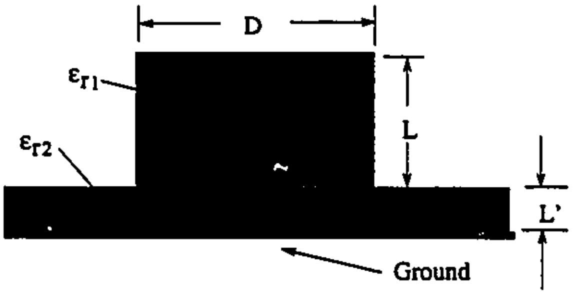

Figure 5.3: Semi-open dielectric resonator on a microstrip substrate

Dimension: D=11.06 mm, L=4.99 mm,

L'=1.59 mm

ϵ_{r1} =35.76, ϵ_{r2} =2.2

Dielectric region: 15 $\Delta z \times 18 \Delta r$

Δz =0.33267 mm, Δr = 0.325294 mm

Δt = 0.65 $(\Delta z + \Delta r)$ / (2c), c is the speed of light in free space.

Table 5.1: Resonant frequency for the $TE_{01\delta}$ mode of a semi-open DR

L' (mm)	FDTD Results (GHz)	Measured Results (GHz)
1.59	4.9680	4.9832
3.18	4.7770	4.7918

The calculated and measurement results are given in Table 5.1. The resonant frequencies are determined by the method presented in this paper. For the experimental results, the DR was mounted on a substrate, and the measurement was carried out with an HP8510B network analyzer.

The variations in the resonant frequency of the $TE_{01\delta}$ mode of a tuning screw DR shown in Fig. 5.4 with respect to different sizes of the structure were analyzed. This is especially useful for choosing an adequate screw diameter to obtain the desired tuning margin. The results are also compared with finite element results [69]. Fig. 5.5 gives its field distribution of $TE_{01\delta}$ mode.

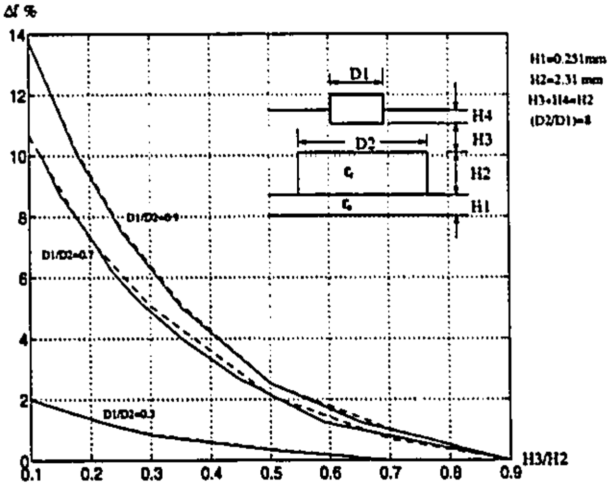

Figure 5.4: Resonator frequency versus different sizes of tuning screw DR

An open two layer semiconductor-dielectric resonator is also analyzed by the algorithm. Fig. 5.6 shows the resonant frequency of $TE_{01\delta}$ mode changing with different sizes of two layer materials. The lower material used is model D8500 dielectric resonator from Trans-Tech. Inc., and the upper material is silicon semiconductor. An experiment was carried out for the two-layer semiconductor-dielectric resonator, with ϵ_{r1}=35.76 and ϵ_{r2} =11.8. The multilayer DR was mounted on a substrate materials with ϵ_r=2.2, and was surrounded by absorbing materials to reduce reflections. The traditional transmission line method was used to measure the resonant frequencies of the DR. The comparison between the resonant frequency of the $TE_{01\delta}$ mode and the experimental results are also given in Fig. 5.6. The comparison results are in reasonable agreement.

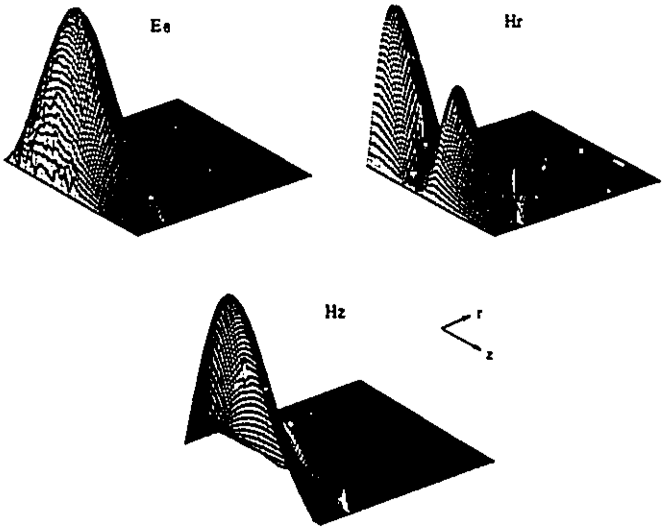

Figure 5.5: Field distributions of $TE_{01\delta}$ mode in a tuning screw DR

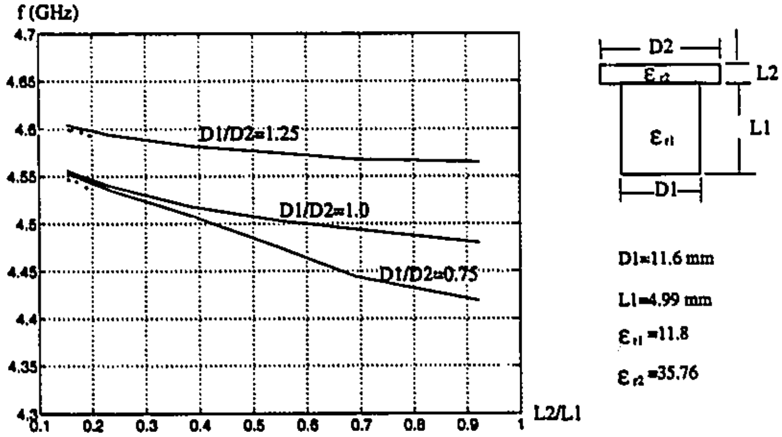

Figure 5.6: Resonant frequency versus different dimensions of a two-layer semiconductor-dielectric resonator

5.3 Modified Frequency-Dependent FD-TD Method

5.3.1 Background of Interaction of Electromagnetic Wave with a Photoinduced Solid-State Plasma

When an electromagnetic wave is incident on a semiconductor, it may propagate through the semiconductor with or without attenuation depending upon the frequency of the radiation. A characteristic feature of all semiconductors in the pure state is that as the frequency of the incident radiation increases from a low value, where the semiconductor behaves as transparent medium, at a particular frequency the absorption increases very rapidly and the absorption coefficient may become as high as $10^5\ cm^{-1}$. This sudden rise in absorption coefficient with incident photon energy is called the absorption edge and in the concept of band theory it is related to the excitation of electrons from the valence band across the band gap to the conduction band. The reaction of free electrons and holes due to the absorption of radiation is called a photoinduced plasma. Normally the energy of the absorbed radiation is greater than the band gap of the semiconductor.

A schematic of a bulk semiconductor on a dielectric waveguide with a photoinduced electron-hole plasma is shown in Fig. 5.7. The thickness d of the plasma layer generally corresponds to the absorption depth of the optical field. In the plasma-occupied region, the applied RF field would satisfy the Maxwell equation as follows:

$$\nabla \times \mathbf{H} = \sigma \mathbf{E} + \frac{\partial \mathbf{D}}{\partial t}, \tag{5.12}$$

where σ is the dark conductivity. The effect of the electron-hole plasma is included in the term **D** through a change in the dielectric constant.

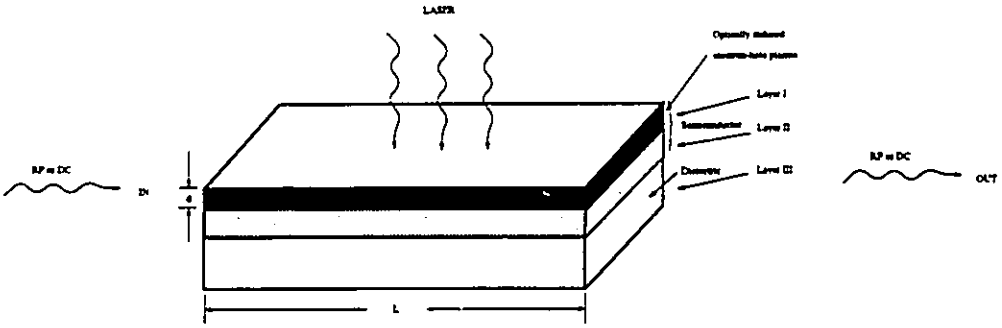

Figure 5.7: Interaction of electromagnetic waves with the photoinduced electron-hole plasma in a semiconductor

5.3.2 Modified $(FD)^2TD$ Method

FDTD simulation has been applied by many investigators to a wide range of electromagnetic problems. Extension of the FDTD method to frequency-dependent materials has, until recently, received relatively little attention. The most pertinent previous paper [70] is limited to one dimension without a FDTD context. The frequency-dependent FDTD, or $(FD)^2TD$, method was first presented by R.Luebbers et al in 1990 [35], [36]. It allows explicit calculation of wide-band transient electromagnetic interactions with frequency dependent materials. This overcomes a serious limitation in current formulations of the FDTD method, which must specify the electromagnetic parameters ϵ, μ and σ as constants. For this work we will assume that the plasma is linear, isotropic and is adequately described by a complex frequency dependent dielectric constant $\epsilon(\omega)$. Extension to the case of an anisotropic plasma should be possible.

The fundamental advantage of a frequency domain numerical analysis is that the electromagnetic parameters are constant at each frequency. In the time domain, all of the frequency domain permittivity information is Fourier transformed into a time domain susceptibility function. The formulation of the $(FD)^2TD$ method incorporates the necessary convolution into the traditional FDTD method. We will assume the reader's familiarity with the basic Yee algorithm [67].

In the typical layered semiconductor-dielectric waveguide structure (shown in Fig. 5.7), the permittivity of the layer I plasma is frequency dependent, while those of layers II and III are frequency independent. The new $(FD)^2TD$ algorithm is therefore applied only to layer I. Details of the FDTD algorithm applied to layers II and III are described in the previous sections.

The time domain electric vector equation is

$$\mathbf{D}(\mathbf{t}) = \epsilon_\infty \epsilon_0 \mathbf{E}(\mathbf{t}) + \epsilon_0 \int_0^{\mathbf{t}} \mathbf{E}(\mathbf{t} - \tau)\chi(\tau) \mathbf{d}\tau \tag{5.13}$$

where ϵ_0 is the permittivity of free space, $\chi(\tau)$ is the electric susceptibility, and ϵ_∞ is the relative permittivity as $\omega \rightarrow \infty$. Here, we assume that $\epsilon_\infty = 1$ for all materials [48].

Using Yee's notation, the relationship between $\mathbf{D}$ and $\mathbf{E}$, for $t = n\Delta t$, is

$$D(t) \simeq D(n\Delta t) = D^n = \epsilon_\infty \epsilon_0 E^n + \epsilon_0 \int_0^{n\Delta t} E(n\Delta t - \tau)\chi(\tau) d\tau. \tag{5.14}$$

Using a central difference scheme, Yee's time differential form of Maxwell's equations can be discretized to the following form:

$$\begin{aligned} E_x^{n+1}(i,j,k) \;=\; & \frac{\epsilon_\infty(i,j,k) + \Delta x_0(i,j,k)}{\epsilon_\infty(i,j,k) + x_0(i,j,k)} E_x^n(i,j,k) + \frac{1}{\epsilon_\infty(i,j,k) + x_0(i,j,k)} \psi_x^n(i,j,k) \\ & + \frac{\Delta t}{[\epsilon_\infty(i,j,k) + x_0(i,j,k)]\epsilon_0} \{ [\frac{H_z^{n+1/2}(i,j+1,k) - H_z^{n+1/2}(i,j,k)}{\Delta z}] \\ & - [\frac{H_y^{n+1/2}(i,j,k+1) - H_y^{n+1/2}(i,j,k)}{\Delta r}] \} \end{aligned} \tag{5.15}$$

$$\begin{aligned} H_x^{n+1/2}(i,j,k) \;=\; & H_x^{n-1/2}(i,j,k) + \frac{\Delta t}{\mu \Delta z}(E_y^n(i,j,k) - E_y^n(i,j,k-1)) \\ & - \frac{\Delta t}{\mu \Delta y}(E_z^n(i,j,k) - E_z^n(i,j-1,k)) \end{aligned} \tag{5.16}$$

where

$$x_0(i,j,k) = \frac{w_p^2(i,j,k)}{v_c(i,j,k)}\Delta t - (\frac{w_p(i,j,k)}{v_c(i,j,k)})^2(1 - e^{-v_c(i,j,k)\Delta t}) \tag{5.17}$$

$$\Delta x_m(i,j,k) = -(\frac{\omega_p(i,j,k)}{v_c(i,j,k)})^2 e^{-mv_c(i,j,k)\Delta t}(1 - e^{-v_c(i,j,k)\Delta t})^2 \tag{5.18}$$

$$\psi_\theta^n(i,j,k) = \sum_{m=1}^{n-1} E_\theta^{n-m}(i,j,k)\Delta x_m(i,j,k) \tag{5.19}$$

$$\psi_\theta^n(i,j,k) = E_\theta^{n-1}(i,j,k)\Delta x_1(i,j,k) + e^{-v_c(i,j,k)\Delta t}\psi_\theta^{n-1}(i,j,k) \tag{5.20}$$

and v_c is the collision frequency, ω_p is the plasma frequency (in rad s^{-1}). The complex permittivity $\epsilon(\omega)$ for an isotropic plasma is given by [33] [48]

$$\epsilon(\omega) = \epsilon_0(\epsilon_L + \frac{\omega_p^2}{\omega(jv_c - \omega)}) \tag{5.21}$$

where ϵ_L is the dielectric constant of the plasma host including the contributions of bound charges.

5.3.3 Complex Permittivity of the Plasma Region

Due to the contribution from free charges, the permittivity of the plasma layer differs from that of the remainder of the plasma host. For a classical electron-hole plasma, we expect the permittivity to follow the theoretical predictions of the Drude theory [33] [48], which defines a collision frequency $v_c = 1/\tau$ and a plasma frequency ω_p such that

$$\omega_p^2 = \frac{ne^2}{\epsilon_0 m^*}, \tag{5.22}$$

where τ is the collision time, n is the plasma density, e is the electric charge and m^* the carrier effective mass. Equation 5.21 can now be written as

Table 5.2: Plasma frequency and collision time for different carriers

i (i=1,2,3,4,5)	ω_{pi}	τ_i
1: intrinsic holes	$\frac{n_{p0}e^2}{\epsilon_0 m_p^*}$	τ_p
2: intrinsic electrons	$\frac{n_{e0}e^2}{\epsilon_0 m_e^*}$	τ_e
3: photoinduced electrons	$\frac{n_e e^2}{\epsilon_0 m_e^*}$	τ_e
4: photoinduced light holes	$\frac{P_l e^2}{\epsilon_0 m_{pl}^*}$	τ_p
5: photoinduced heavy holes	$\frac{P_h e^2}{\epsilon_0 m_{ph}^*}$	τ_p

$$\epsilon_r = \epsilon_L - \frac{\omega_p^2}{\omega^2 + v_c^2} - j\frac{v_c}{\omega}\frac{\omega_p^2}{\omega^2 + v_c^2} \tag{5.23}$$

This shows that the difference between the plasma permittivity and that of the host depends on plasma density, the collision frequency of the plasma, and the frequency of the microwave signal. Substituting for ω_p and v_c, assuming an intrinsic host, and assuming high level injection conditions ($n_e = n_p$), yields the following expansions for equation 5.23:

$$\frac{\omega_p^2}{\omega^2 + v_c^2} = \sum_{i=1}^{5} \frac{n_i e^2 \tau_i^2}{m_i^* \epsilon_0 (1 + \omega^2 \tau_i^2)} \tag{5.24}$$

$$\frac{v_c}{\omega}\frac{\omega_p^2}{\omega^2 + v^2} = \sum_{i=1}^{5} \frac{n_i e^2 \tau_i}{\omega m_i^* \epsilon_0 (1 + \omega^2 \tau_i^2)} \tag{5.25}$$

where i=1,2,3,4,5 correspond respectively to intrinsic holes, intrinsic electrons, photoinduced electrons, and photoinduced light and heavy holes. Table 5.2 gives ω_{pi} and τ_i for each of these cases.

Collision times for electrons and holes are

$$\tau_e = \frac{\mu_e m_e^*}{e}, \qquad \tau_p = \frac{\mu_p m_p^*}{e}. \tag{5.26}$$

Where μ_e, μ_p are the respective electron and hole mobilities.

Combining the effects of illumination as described in 5.24-5.26 with 5.17 and 5.18 yields

$$x_0(i,j) = \sum_{i=1}^{5}[\frac{\omega_{pi}^2}{v_{ci}}\Delta t - (\frac{\omega_{pi}}{v_{ci}})^2(1 - e^{-v_{ci}\Delta t})] \tag{5.27}$$

$$\Delta x_m(i,j) = \sum_{i=1}^{5}[-(\frac{\omega_{pi}}{v_{ci}})^2 e^{-mv_{ci}\Delta t}(1 - e^{-v_{ci}\Delta t})^2] \tag{5.28}$$

The photoinduced conductivity is

$$\sigma_p = \omega\epsilon_0\epsilon''. \tag{5.29}$$

5.3.4 Recombination-Generation Processes and Skin Depth in Plasma Host

The net steady-state recombination rate for an semiconductor illuminated strongly enough to support high level injection where $n_e = n_p \gg n_{p0}$ or n_{e0}, can be written as [71], [72]

$$R_r = \frac{n_e}{\tau_p + \tau_e} \tag{5.30}$$

while the electron-hole generation rate is

$$G = \frac{P(1-R)}{E_g e A\delta} \tag{5.31}$$

P is the input light power, R is the reflection coefficient at the air-semiconductor interface, E_g is the semiconductor bandgap, A is the area of the plasma (which is normally equal to the illuminated area) and δ is the $1/e$ illumination penetration depth. Note that the product $A\delta$ is the volume occupied by the plasma.

Under equilibrium conditions, the recombination rate is equal to the generation rate. It follows, then, that the relationship between plasma density n_e and the input power P is

$$P = \frac{E_g e A\delta}{(\tau_p + \tau_e)(1 - R)} n_e. \qquad (5.32)$$

The plasma diffusion depth is given in [28]

$$d = \frac{1}{\alpha}[\frac{L_a(1 + \alpha L_a) + v_s\tau}{L_a + v_s\tau}][\frac{1}{\alpha L_a}(\frac{\alpha L_a^2 + v_s\tau}{L_a + v_s\tau})]^{\frac{\alpha L_a}{1-\alpha L_a}} \qquad (5.33)$$

and

$$L_a = (\frac{2\mu_n\mu_p\tau k_b T}{e}\frac{1}{\mu_n + \mu_p})^{\frac{1}{2}} \qquad (5.34)$$

L_a is the ambipolar diffusion depth, k_b is Boltzmann's constant, T is the absolute temperature, α is the radiation absorption coefficient, and $v_s = 10^4$ cm/s is the surface recombination velocity. Although α is a strong function of the illumination wavelength, this can be taken as a constant for monochromatic sources such as laser diodes or light-emitting diodes.

5.4 Optically-Controlled Dielectric Resonators

Dielectric resonators (DRs) are a basic element in microwave integrated circuits. They have proven their usefulness in microwave band-reject and bandpass filters, slow-wave structures, frequency converters, diode and FET oscillators, as well as frequency-selective limiters [73]. They are also compatible with TEM-line, waveguide and microstrip transmission line circuits . If one considers all of these applications, the DR's resonant frequency is obviously the most important of all its parameters, in terms of the control and adjustment that needs to be exercised once the device is *in situ.* One well-known tuning method incorporates the variable proximity of a metal plate adjusted by a screw [44]. However, there are several mechanical shortcomings, associated with a tuning plate. These include temperature sensitivity, difficulty of incorporation in MMIC circuits and inherently slow tuning adjustment. An elegant non-mechanical substitute for the plate is an optically induced sheet of plasma on the

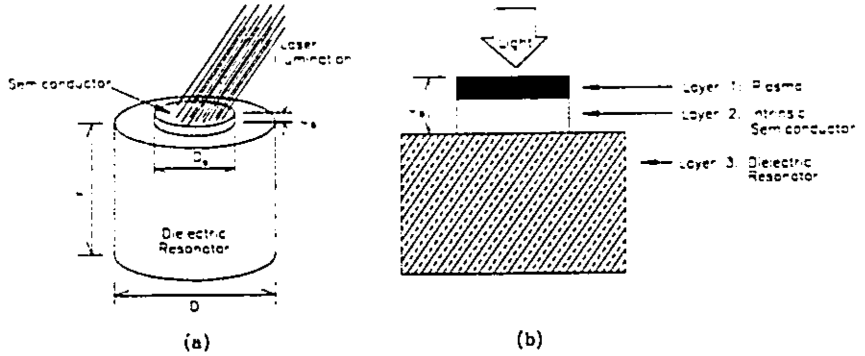

Figure 5.8: (a) Optically controlled dielectric resonator schematic (b) definition of the simulated layers

surface of a slab of semiconductor. This new tuning element, discussed by Herczfeld *et al.* [74], defines a novel device called an optically controlled dielectric resonator (OCDR).

Fig. 5.8 (a) depicts a dielectric resonator with a slab of intrinsic semiconductor placed on top. Optical resonator tuning is realized when the slab is illuminated by light of a wavelength shorter than the semiconductor bandgap (*e.g.* about 880 nm for GaAs), thus forming a sheet of plasma on the illuminated semiconductor face. The light can be locally generated or supplied by an optical waveguide. The diameter and height of the dielectric resonator are selected properly so that the resonator supports a $TE_{01\delta}$ mode. The depth of injection for the optically induced plasma is a function of the host semiconductor's optical absorption and the wavelength of the illumination. Generally, shorter wavelengths suffer higher semiconductor absorption and hence a thinner region of injection.

For a sufficiently small plasma injection thickness, the final steady state plasma thickness is determined primarily by carrier diffusion and recombination. The plasma layer will have a higher microwave dielectric constant than the semiconductor host material. One then expects to see the resonant frequency increase with the plasma density, since the plasma acts like a conductive tuning plate. The magnitude of the frequency shift Δf as a function of the illumination intensity (and hence plasma density) depends on the resonator's material and geometric design. Deriving this relation theoretically is the object of this chapter.

5.4.1 Two-Dimensional $M(FD)^2TD$ Method for Optically-Controlled Dielectric Resonator

In the frequency dependent photoinduced plasma layer, using a central difference scheme, Yee's time differential form of Maxwell's equation [67] can be discretized to the two-dimensional form:

$$\begin{aligned} E_\theta^{n+1}(i,j) &= \frac{\epsilon_\infty(i,j)+\Delta x_0(i,j)}{\epsilon_\infty(i,j)+x_0(i,j)} E_\theta^n(i,j) + \frac{1}{\epsilon_\infty(i,j)+x_0(i,j)} \psi_\theta^n(i,j) \\ &\quad + \frac{\Delta t}{[\epsilon_\infty(i,j)+x_0(i,j)]\epsilon_0} \{ [\frac{H_r^{n+\frac{1}{2}}(i,j+\frac{1}{2}) - H_r^{n+\frac{1}{2}}(i,j-\frac{1}{2})}{\Delta z}] \\ &\quad - [\frac{H_z^{n+\frac{1}{2}}(i+\frac{1}{2},j) - H_z^{n+\frac{1}{2}}(i-\frac{1}{2},j)}{\Delta r}] \} \end{aligned} \tag{5.35}$$

$$H_r^{n+\frac{1}{2}}(i,j+\frac{1}{2}) = H_r^{n-\frac{1}{2}}(i,j+\frac{1}{2}) + \frac{\Delta t}{\Delta z}\frac{1}{\mu}[E_\theta^n(i,j) - E_\theta^n(i,j-1)] \tag{5.36}$$

$$H_z^{n+\frac{1}{2}}(i+\frac{1}{2},j) = H_z^n(i+\frac{1}{2},j) - \frac{\Delta t}{\mu \Delta r r_{i+\frac{1}{2}}}[r_{i+1}E_\theta^n(i+1,j) - r_i E_\theta^n(i,j)] \tag{5.37}$$

where parameters such as ϵ_∞, Δx_0, x_0 and Δx_m are same as those of the previous section.

5.4.2 Simulation Results and Available Experimental Results

The simulated OCDR was subjected to a modelled abrupt electric field excitation so that many resonant modes were excited. A Fourier transform was then applied to the

Table 5.3: Numerical parameters for Si and GaAs at T=300 K

parameters	Si (T=300 K) [33]	GaAs (T=300 K) [75],[76],[77]
m_e^*	0.259 m_0	0.07 m_0
m_p^*	0.38 m_0	0.713 m_0
m_{pl}^*	0.16 m_0	0.12 m_0
m_{ph}^*	0.49 m_0	0.68 m_0
μ_e	1500 $cm^2/V.s$	8500 $cm^2/V.s$
μ_p	600 $cm^2/V.s$	400 $cm^2/V.s$
n_{p0}	10^{11} cm^{-3}	$1.1 * 10^7$ cm^{-3}
n_i	$1.18 * 10^{10}$ cm^{-3}	$2.25 * 10^6$ cm^{-3}
P_l	$0.14n_p$	$0.13n_p$
P_h	$0.86n_p$	$0.87n_p$
e	$1.6 * 10^{-19}$ coul	$1.6 * 10^{-19}$ coul
m_0	$9.11 * 10^{-31}$ kg	$9.11 * 10^{-31}$ kg
ϵ_L	11.8	10.9
E_g	1.12 eV	1.43 eV

response to extract the resonant frequencies from the simulated results. Two types of OCDRs were considered: an X-band resonator tuned by a silicon (Si) semiconductor wafer; and a K-band resonator with a wafer of gallium arsenide (GaAs). Properties of the semiconductors are listed in Table 5.4.2.

Fig. 5.9 shows the $TE_{01\delta}$ mode resonant frequency shift for an illuminated Si slab (with dimensions $D_s \times L_s$= 1.76 × 0.60 mm^2) on an X-band (f_o=10.92 GHz) dielectric resonator ($D \times L$=5.46 × 2.46 mm^2, ϵ_r = 36), as a function of plasma density for various thicknesses of the plasma layer. Fig. 5.10 is a similar plot for the case of a GaAs tuning slab ($D_s \times L_s$=0.77 × 0.60 mm^2) on a Ka-band (f_o=30.91 GHz) dielectric resonator ($D \times L$=1.93 × 0.86 mm^2, ϵ_r = 29.1). No significant frequency shift occurs until a critical quantity of photoinduced plasma is created, after which it rises rapidly and saturates. Note that Δf is only weakly affected by the plasma thickness. This is expected, since the electrical skin depths at the resonator frequencies are less than the given plasma thickness. For these configurations, the relative maximum frequency

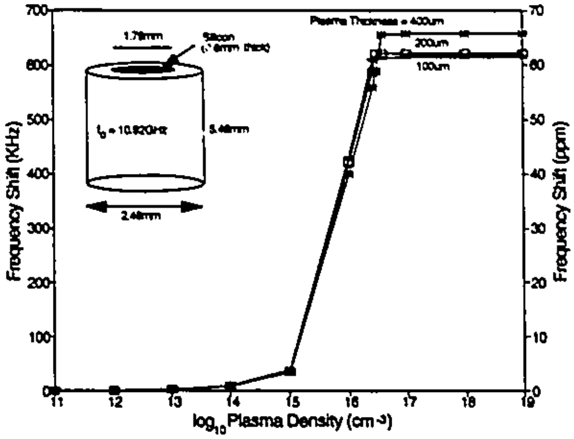

Figure 5.9: Predicted $TE_{01\delta}$ mode resonant frequency shift for an X-band resonator ($\epsilon_r = 36$) versus plasma density for various plasma depths in silicon

shift for the X-band OCDR (70 ppm) is almost twice as great as that for the Ka-band OCDR (40 ppm).

The influence of the semiconductor on the X-band DR spectrum is shown in Fig.5.11. A semiconductor layer strongly affects the high-order resonance modes, and both Si and GaAs have about the same effect on the fundamental mode. Fig. 5.12 shows the resonance frequency changes in an illuminated OCDR. As in the case of metal plate tuning, the resonator frequency goes up and the Q decreases as plasma density increases.

Fig. 5.13 shows the relationship between optical illumination irradiance and photoinduced plasma density. For a fixed photoinduced plasma density and resonator tuning range, higher resonator frequencies require lower illumination irradiance.

The modified FDTD technique that we have developed was applied to an actual experiment by Herczfeld *et al* [74] in an attempt to emulate their results. In the experiment, the $TE_{01\delta}$ mode frequency of an X-band DR was measured when overlaid with a Si slab. The plasma layer thickness and density was calculated from the parameters of Table 5.4.2 and the illumination reported in [74]. Our simulated results for a DR identical to that in [74] are compared with measurement in Fig. 5.14 and they are shown to agree within 8%. This result is encouraging, but it should be noted

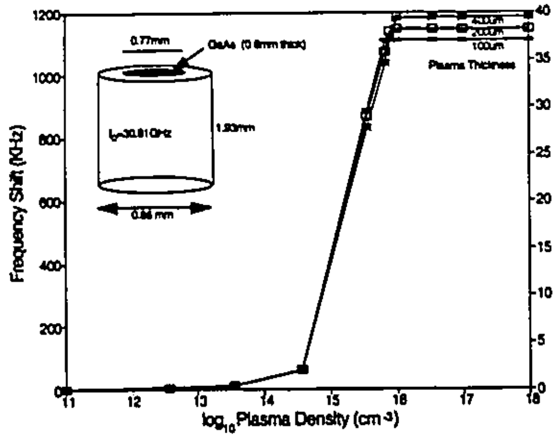

Figure 5.10: Predicted $TE_{01\delta}$ mode resonant frequency shift for a Ka-band resonator (ϵ_r=29.1) versus plasma density for plasma depths in GaAs

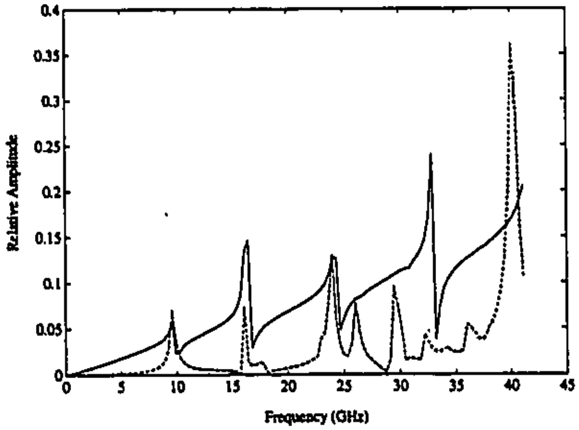

Figure 5.11: Spectrum for an X-band resonator without a wafer (solid line), with a Si wafer (dashed line) and with GaAs wafer (dotted line)

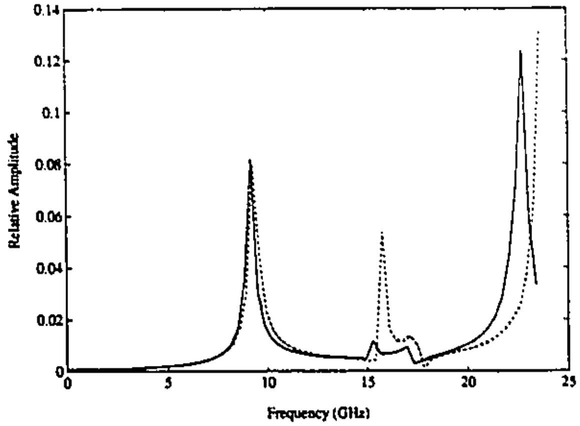

Figure 5.12: Spectrum for a Silicon wafer tuned resonator without illumination (solid line), with illumination and n_e=10^{14} cm^{-3} (dashed line), and with illumination and $n_e = 10^{18}$ cm^{-3} (dotted line)

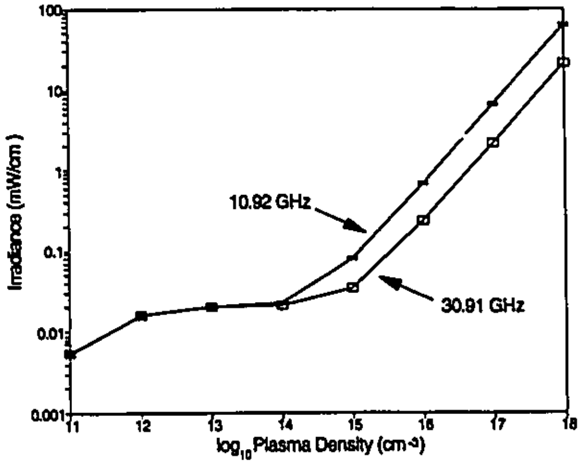

Figure 5.13: Irradiance versus photoinduced carrier density (T=300 K) for silicon wafer (solid line) and GaAs wafer (dashed line)

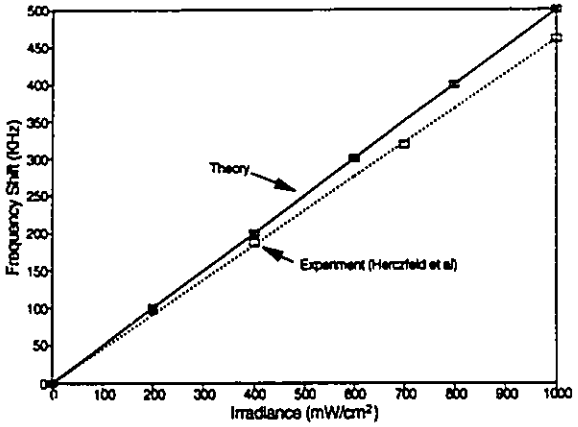

Figure 5.14: Predicted shift in resonant frequency as a function of irradiance and experimental results of Herczfeld *et al*

that the experimental material parameters were not available and not necessarily equal to the values in Table 5.4.2.

5.5 Optically-Controlled Phase-Shifters / Attenuators

The CPW configuration to be studied is shown in Fig. 5.15. The strip and the ground plane metallization thickness is considered negligible. Assuming a uniform top-side continuous light illumination across the slot of width W, illuminated regions in the semiconductor will generate rectangular plasma strips of width W and diffusion depth d. The optically induced phase shift $\Delta\phi$ for a given section of waveguide of length l is determined by computing the change in the waveguide phase propagation constant β when light is applied, so that $\Delta\phi = \Delta\beta l$. When optically controlled CPW as an attenuator, the photoinduced attenuation can be obtained from the attenuation constant α.

If the semiconductor is illuminated strongly enough to support high level injection, the relationship between plasma density n_e for both illuminated areas, and the illumination photon flux Φ impinging on the substrate can be expressed as

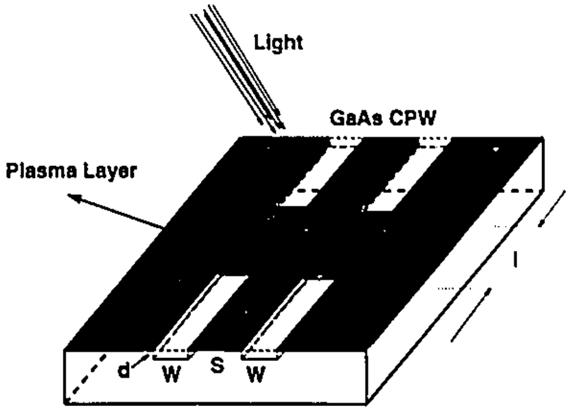

Figure 5.15: Optically controlled coplanar waveguide

$$n_e = \frac{(\tau_p + \tau_e)(1 - R)}{2Wld}\Phi, \tag{5.38}$$

where R is the reflection coefficient of the air-semiconductor interface, E_g is the semiconductor bandgap energy, d is the diffusion depth, and τ_p and τ_e are the recombination times for electrons and holes respectively. The equation considers only direct bandgap generation and assumes photon energies between E_g and $2E_g$, which corresponds to a wavelength range of 435nm to 870nm for GaAs. If the illumination is monochromatic, Φ is directly proportional to the illumination power P: $\Phi = P\lambda/(1.24\mu m)e$

5.5.1 Three-Dimensional $M(FD)^2TD$ Method for Optically Controlled Coplanar Waveguide

The $M(FD)^2TD$ leap-frog difference equations are used for the field calculations. By updating the fields using these equations, one can simulate the propagation of a pulse on the GaAs CPW, as well as photoconductive attenuation. Mur's first absorbing boundary condition is used to evaluate the tangential field components on the boundaries.

After evaluating the time domain field distribution, the frequency-domain parameters are derived by using a Fourier transform. The phase propagation constant and attenuation constant are obtained from the transfer function for the length l of illuminated GaAs CPW:

$$e^{-\gamma(f)l} = \frac{E_x(f, z = l)}{E_x(f, z = 0)} \tag{5.39}$$

where $\gamma(f) = \alpha(f) + j\beta(f)$. The permittivity ϵ_{reff}(f) is defined through $\beta(f)$ as $\beta(f) = 2\pi f\sqrt{\mu_0\epsilon_0\epsilon_{reff}(f)}$, or

$$\epsilon_{reff} = \frac{\beta(f)^2}{\omega^2\epsilon_0\mu_0} \tag{5.40}$$

The guide wavelength $\lambda_g = 2\pi / \beta(f)$.

5.5.2 Simulation Results and Experimental Results

The following parameters have been applied to the CPW segment of Fig. 5.15 to simulate its microwave properties when illuminated with 800 nm radiation:

W=49 μm, S=74 μm, l=500 μm, $\epsilon_r = 13.1$, $\mu_n = 8500\ cm^2/Vs$, $\mu_p = 400\ cm^2/Vs$,$\tau_e = \tau_p = 250$ ps, $v_s = 10^4\ cm/s$, T=300K, $k_b = 1.381 \times 10^{-23}\ J/K$, $E_g = 1.43\ eV$.

Figs. 5.16 (a) and 5.16 (b) show the dependence of the complex dielectric constant on plasma density. The photoconductivity of the CPW as a function of frequency is given in Fig. 5.17.

Plots of the expected phase shift and insertion loss are given in Fig. 5.18 and Fig. 5.19. Based on this analysis, this device is expected to get larger attenuation and phase shift when light illumination is increased. Both attenuation and phase shift resulting from photoconductivity are more dependent on illumination power density than plasma depth. For the given parameters, illumination by one milliwatt (1 mW) of 850nm radiation with a reflectivity R of 0.65 will yield an n_e of only $5 \times 10^{11} cm^{-3}$. This follows from the very small values of τ_n and τ_p associated with GaAs, possibly explaining a preference for the use of silicon as a substrate in other works [28], [33].

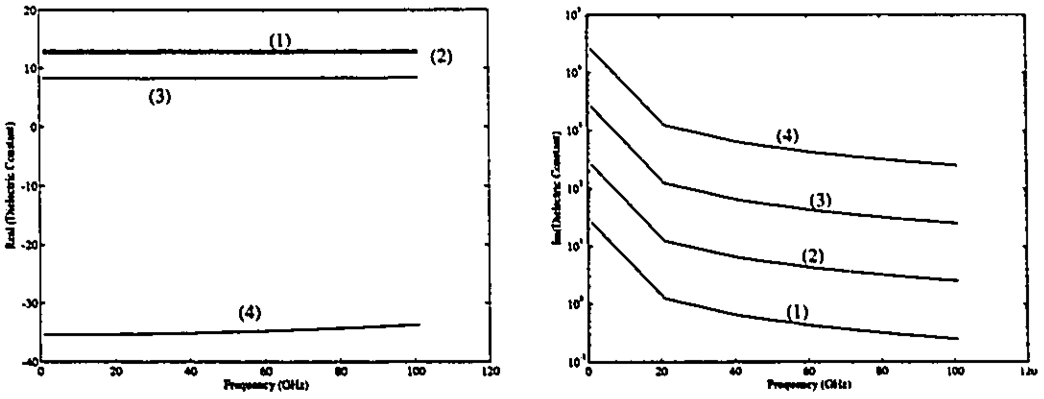

(a) (b)

Figure 5.16: Dielectric constant of photo-induced plasma; line 1: $n_e = 10^{13}\ cm^{-3}$ line 2: $n_e = 10^{14}\ cm^{-3}$ line 3: $n_e = 10^{15}\ cm^{-3}$ line 4: $n_e = 10^{16}\ cm^{-3}$. (a) real part of the dielectric constant (b) imaginary part of dielectric constant

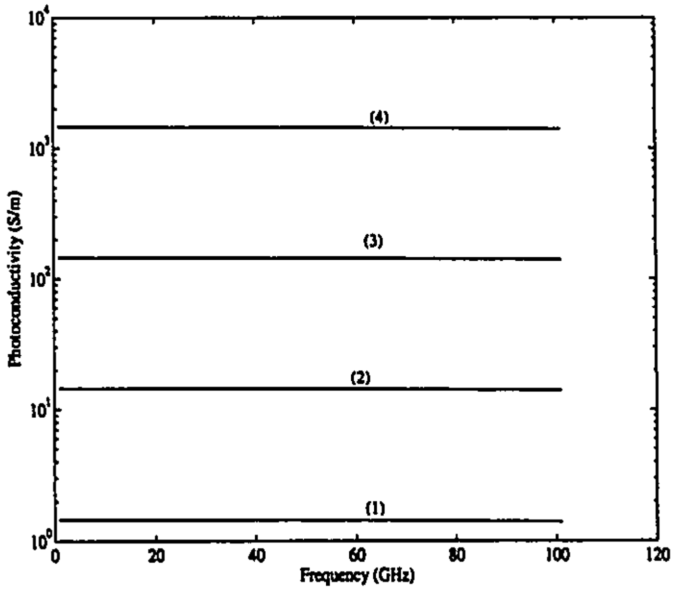

Figure 5.17: Photoconductivity of photo-induced plasma; line 1: $n_e = 10^{13}\ cm^{-3}$ line 2: $n_e = 10^{14}\ cm^{-3}$ line 3: $n_e = 10^{15}\ cm^{-3}$ line 4: $n_e = 10^{16}\ cm^{-3}$

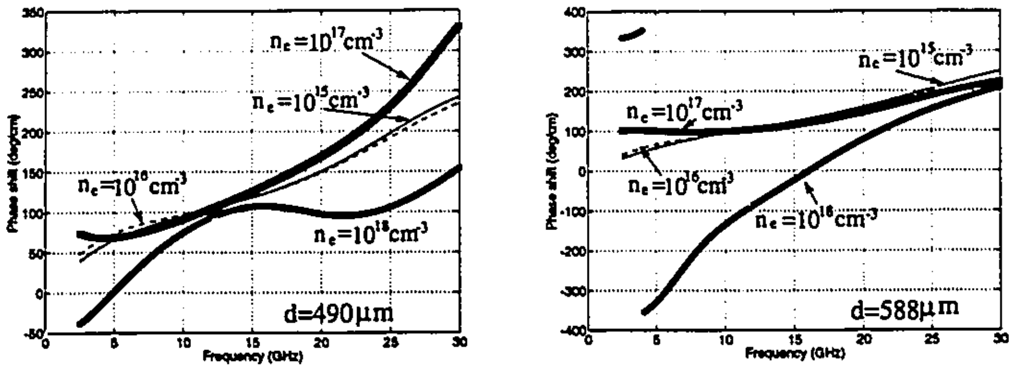

(a) (b)

Figure 5.18: Phase shifter of an optically controlled coplanar waveguide; (a) plasma depth = 490 μm (b) plasma depth = 588 μm

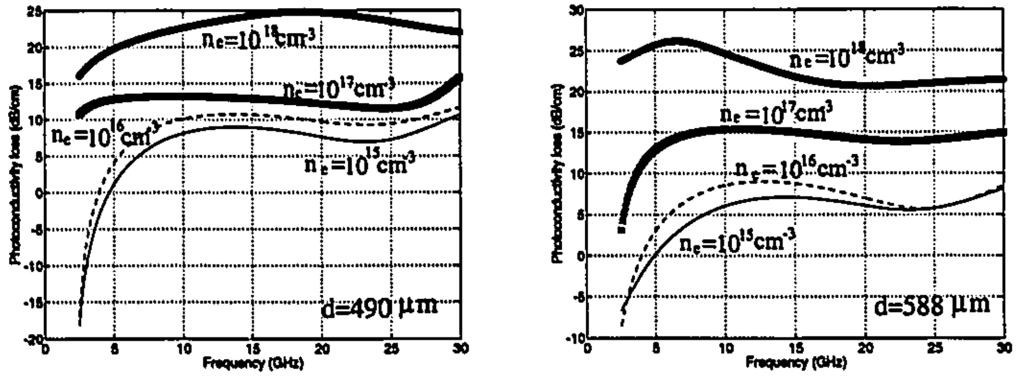

(a) (b)

Figure 5.19: Photoconductivity loss of an optically controlled coplanar waveguide; (a) plasma depth = 490 μm (b) plasma depth = 588 μm

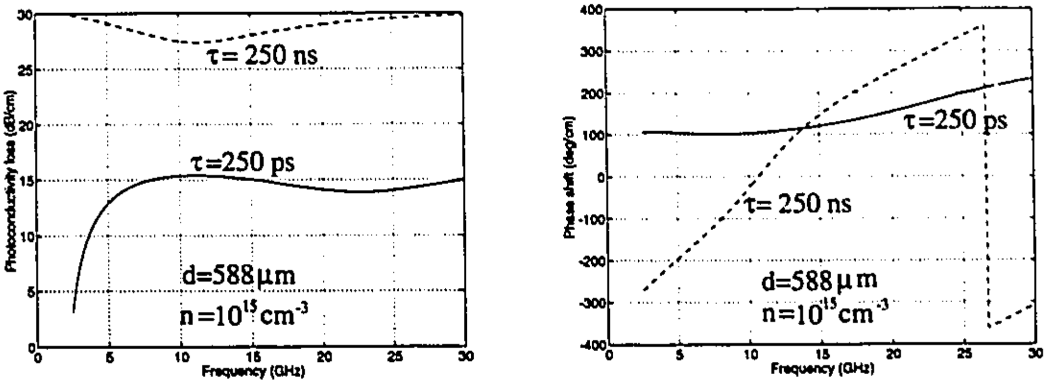

(a) (b)

Figure 5.20: Comparison of phase shift and attenuation for different collision times (a) attenuation (b) phase shift

Fig. 5.20 shows the simulation results for different collision times of material. It is expected that we can get good phase shifter or attenuator if we choose an appropiate material.

5.6 Discussion and Conclusions

A physics-based full-wave time domain method has been developed to carry out a three dimensional analysis of optically controlled passive microwave devices. However, long semiconductor substrate recombination times(*e.g.* $\geq 1\ \mu s$) may be required to make these devices useful with low levels of illumination, thus implying a compromise between control speed and illumination power. Optically controlled active microwave devices can also be extended by using this method with current-continuity equations based on drift-diffusion for both electrons and holes. The performance of optically controlled microwave devices is expected to predict accurately by using this method. Various optical control methods will be finally used in DBF systems.

Chapter 6

Conclusions

This work has contributed to the digital beamforming techniques in three areas: DBF array receiver system design and implementation, active antennas in DBF system and other applications, and investigation of optical control in DBF system.

In DBF system design and implementation, we have designed and developed a C-band multilayer double down conversion IF-sampling receiver using commercial MMIC chips. Based on an element receiver design, a four-element linear array receiver system was implemented. The system works at the center frequency of 4.9256 GHz, has a noise figure around 7 dB, a signal bandwidth 360 KHz and a dynamic range 64 dB. In the system, a new self-calibration for multilayer structure has also been proposed and realized in the array system.

With regard to active antennas, an integrated active receiver antenna and transmitter antenna for DBF system were studied. A low-noise receiver module and a power-amplifier transmitter module have been designed and developed. Active antennas for DBF array are simply the same as the single module. A multilayer oscillator active antenna at C-band as a transmitter or source was proposed and tested. Furthermore, we studied the active array antennas. An X-band four-element active antenna has been investigated and good experimental results have been achieved. In addition, an active antenna for other applications, such as spatial power combiners, spatial amplifiers and larger active antennas, have been discussed. Several new structures were designed and tested. It is believed that all the structures proposed in this work have applications in future radar and communication systems. Although all our realized active antennas were MIC structures, the design techniques and structures are equally well suited for MMIC designs.

The study of optically controlled microwave devices is the another part of this thesis. In DBF array system, each element has its own receiver / transmitter module so that optically controlled microwave devices, as a new technique, is especially important in DBF investigation. In this thesis, our work concentrated on the accurate simulation of optically controlled microwave devices, especially passive optically controlled microwave devices. A physics-based full wave analysis, modified frequency-dependent FDTD method, has been presented. Two-dimensional optically controlled dielectric resonators and three-dimensional optically controlled coplanar waveguide were analyzed and compared with experimental results.

The next step would be to develop the larger DBF system, either planar array or linear array. The main limitation will confined in its cost. Investigation of transmitter DBF system is just at beginning. Integrated active antenna and optical control used in real DBF systems are other possible topics.

Appendix A

OmniSys File For A DBF Receiver

```
! SYD FILENAME: DBFREC
! DESCRIPTION:  INTEGRATED RECEIVER FOR DBF
! DATE/AUTHOR:  March 9, 1993/Ying Shen

DIM
    FREQ    GHZ
    RES     OH
    LNG     MM
    TIME    NS
    ANG     DEG
    DIST    M
    PWR     DBM

SYD
    MSUB  ER=10.8 H=0.635 T=0.0356 RHO=0.73 RGH=0.00241
    TAND  TAND=0.0019
    TEMP  TEMP=30
```

```
    TLIN   1   2   Z=50  E=240  F=5
    MLIN   2   3   W=0.53  L=10
    S2P0   3   4   BPF1   ! measured S parameters of bandpass filter
    MIX    4   5   A=23 NF=5 LO=5 TYP=2 S11=-7  S22=-7  &
    GCOMP3 IP3=21 1DBC=-8
    MLIN   5   6   W=0.53  L=30
    S2P1   6   7   SAWF   ! measured S parameters of SAW filter
    MLIN   7   8   W=0.53  L=10
    TLIN   8   9   Z=50  E=3.573  F=0.0744
    MSUB  ER=6.15 H=1.31  T=0.0356 RHO=0.73 RGH=0.00241
    S2P2   9   10  AGC    ! measured S parameters of AGC amplifier
    S2P3   10  11  AMPT   ! measured S parameters of two satge amplifier
    MIX    11  12  A=-7 NF=7 LO=0.078125 TYP=2 S11=-7 S22=-7 &
    GCOMP3 IP3=15 1DBC=4
    MLIN   12  13  W=1.89 L=26
    TLIN   13  14  Z=50  E=0.179  F=0.003725
    MLIN   14  15  W=2.77 L=27
    GAIN1  15  16  A=19.5 NF=10 S11=-32 S22=-20
    MLIN   16  17  W=2.77 L=20
    DEF2P  1   17  DBFREC

    DBFREC 1   2
    DEF2P  1   2   DBFREC1

SOURCE
    DBFREC   SWEEP  F(4.922 4.927 0.0001 )  P(-50  -10  10)
    DBFREC1  SWEEP  F(4.922 4.927 0.0001 )  P(0 0 0)
```

```
OUT
    NBW       NBW=30
    DBFREC    POWER   GR1
    DBFREC    GAIN    GR2
    DBFREC    GC      GR3
    DBFREC    IP3OS   GR4
    DBFREC    1DBCO   GR5
    DBFREC1   GAIN    GR6
    DBFREC1   DB[S11] GR7
    DBFREC1   DB[S22] GR7
    DBFREC1   NF      GR8
    DBFREC1   GD      GR9
```

Appendix B

Touchstone File for an Active Antenna Design

```
! INTEGRATED ACTIVE ANTENNA DESIGN
! POWER AMPLIFIER DESIGN FOR DBF TRANSMITTER
! Data: April 6, 1992
! Designer: Ying Shen


DIM
        FREQ    GHZ
        RES     OH
        IND     NH
        CAP     PF
        LNG     MM
        TIME    NS
        COND    /OH
```

```
        ANG     DEG


VAR
        LFB #2  2.388493   10
        CFB =150
        RFB =500
        RS= 150
        CS=180
        LIND1 #1 1.191680 50
        LIND2 #1 1.164585 50
        W1# 1 3.767529   8
        W2# 1  1.432901    4
        L1 #2  2.031709   10
        L2 #2  2.013391   10
        L3 #2  2.001182   10
        L4 #2   2.765817   10
        L5 #2   7.020349   10
        L6 #2  2.000557   10
        L7 #2   9.993471   10
        L8 #2  8.768319   10


CKT
        MSUB ER=6.15 H=1.905 T=0.0356 RHO=0.73 RGH=0.00241

        RES   1   2   R^RFB
        MLIN  2   3   W=2.86 L^LFB
        CAP   3   4   C^CFB
```

```
DEF2P 1   4   FEEDBK

MLIN  1   2   W=2.86  L=5
CAP   2   3   C=22
IND   3   4   L^LIND1
MLIN  4   5   W=2.86  L^L1
MLEF  5       W^W1    L^L2
MLIN  5   6   W=2.86  L^L3
RES   6   20  R=2000
MLIN  20  21  W=0.3   L^L4
CAP   21  0   C=1000
S2PA  6  7  8  NE8004985
WIRE  8   0   D=0.4  L=1  RHO=0.705
WIRE  8   0   D=0.4  L=1  RHO=0.705
FEEDBK  6  7
RES   6   40  R^RS
CAP   40  0   C^CS
RES   7   30  R=200
MLIN  30  31  W=0.3  L^L5
CAP   31  0   C=1000
MLIN  7   9   W=2.86 L^L6
MLEF  9       W^W2   L^L7
MLIN  9  10   W=2.86 L^L8
IND   10 11   L^LIND2
CAP   11 12   C=22
MLIN  12 13   W=2.86 L=5

DEF2P  1   13  PAMP
```

```
FREQ

        SWEEP   4.0     6.0   0.01


OUT

        PAMP   DB[S21]  GR1

        PAMP   DB[S11]  GR2

        PAMP   DB[S22]  GR3

        PAMP   MAG[Z2]  GR4

        PAMP   ANG[Z2]  GR5

        PAMP   NF       GR6


FILEOUT

        PAMP   TS  SPAR  PAMP.S2P

GRID

        FREQ    4.4     5.6     0.01

        GR1     0        15     3

        GR2     0       -20     5

        GR3     10      -40     10

        GR4     0       200     40

        GR5     -180    180     45

        GR6     0       10      2


OPT

        FREQ    4.0   6.0

        PAMP    DB[S21] >7

        PAMP    DB[S11] <-10
```

```
RANGE   4.9156   4.9156
PAMP    MAG[Z2] =62.796
PAMP    ANG[Z2] =-8.424
RANGE   4.9186   4.9186
PAMP    MAG[Z2] =63.553
PAMP    ANG[Z2] =-8.057
RANGE   4.9256   4.9256
PAMP    MAG[Z2] =65.318
PAMP    ANG[Z2] =-7.032
RANGE   4.9266   4.9266
PAMP    MAG[Z2] =65.569
PAMP    ANG[Z2] =-6.866
RANGE   4.9356   4.9356
PAMP    MAG[Z2] =67.773
PAMP    ANG[Z2] =-5.148
```

Bibliography

[1] H. Steyskal, "Digital beamforming antennas: an introduction," *Microwave J.*, vol. 30, pp. 107–124, Jan. 1987.

[2] T.Lo, C.Laperle, Y.Shen, M.Zhang, and J.Litva, "Digital beamforming for mobile satellite communications: technology assessment and design study," tech. rep., Contract Report for SPAR Aerospace Ltd.,, Oct. 1993.

[3] A.D.Craig and et al, "Study on digital beamforming networks," tech. rep., ESA Contract Report, July 1990.

[4] A.D.Craig, C.K.Leong, and P.C.Marston, "A digital beamforming payload concept for advanced mobile missions," in *ESA Workshop on Advanced Beamforming Networks for Space Applications*, pp. 2.5.1–2.5.17, Nov. 1991.

[5] F.J.Lake and R.P.Curnow, "Active interference suppression and onboard source location within a digital beamforming payload," in *ESA Workshop on Advanced Beamforming Networks for Space Applications*, pp. 3.4.1–3.4.11, Nov. 1991.

[6] M.Barrett, "Digital beamforming network technologies for satellite communications," in *ESA Workshop on Advanced Beamforming Networks for Space Applications*, pp. 3.6.1–3.6.11, Nov. 1991.

[7] J.F.Rose, "Digital beamforming receiver technology," in *Proceedings of 1990 IEEE APS*, pp. 380–383, 1990.

[8] W.Sander, "Experimental phased-array radar ELRA: antenna system," *IEE Proc., pt.f*, vol. 127, no. 4, 1980.

[9] P.Barton, "Digital beam forming for radar," *IEE Proc., Pt.f*, vol. 127, no. 4, 1980.

[10] B.Wardrop, "Experimental linear phased array with partial adaptivity," *IEE Proc., Pt.f*, vol. 130, no. 2, 1983.

[11] J.Litva, "Introduction to sampled aperture radar technology," in *Proc. of IEEE International Electrical Electronic Conf.*, (Toronto), 1983.

[12] T.Lo and J.Litva, "Low-angle tracking using multifrequency sampled aperture radar," *IEEE Trans. on Aerospace and Electronic Systems*, vol. 27, pp. 797–805, Sept. 1991.

[13] B.Wardrop, "Digital beamforming in radar system: a review," in *Proc. of Military Microwave Conf.*, UK 1984.

[14] J.M.Loomis and J.F.Rose, "A DBF array," Tech. Rep. RE-83-21, US Army MICOM Technical Report, May 1983.

[15] L.Eber, "Digital beam steering antenna," Final Technical Report RADC-TR-88-83, General Electric Company, 1988.

[16] W.Chujo and K.Yasukawa, "Design study of digital beam forming antenna applicable to mobile satellite communications," in *Proc. of 1990 IEEE APS*, pp. 400–403, May 1990.

[17] Y.Ohtaki, W.Chujo, and et al., "Implementation of a DBF antenna for mobile satellite communications utilizing multi-digital signal processors," in *Proc. of 1992 Int. Symp. on Antenna and Prop. (ISAP'92)*, 1992.

[18] J.Litva, T.Lo, and Y.Shen, "Combining electromagnetics and digital signal processing: moving towards the intelligent antenna," in *Proc. of ANTEM 92*, (Winnipeg), Aug. 1992.

[19] D.M.Pozar, "Microstrip antenna," *Proc. of IEEE*, vol. 80, pp. 79–91, Jan. 1992.

[20] K.Chang, K.A.Hummer, and J.L.Klein, "Experiments on injection locking of active antenna elements for active phased arrays and spatial power combiners," *IEEE Trans. on Microwave and Techniques*, vol. 37, pp. 1078–1084, 1989.

[21] J.Birkeland and T.Itoh, "FET-base planar circuits for quasi-optical sources and transceivers," *IEEE Trans. on Microwave and Techniques*, vol. 37, pp. 1452–1459, 1989.

[22] S.Kawasaki and T.Itoh, "A layered negative resistance amplifier and oscillator using a FET and a slot antenna," in *Proc. of 1991 IEEE MTT-S*, pp. 1261–1264, 1991.

[23] P.Herczfeld, "Monolithic microwave photonic integrated circuits: a possible follow-up to MMIC," *Microwave J.*, vol. 35, pp. 64–78, Jan. 1992.

[24] C.H.Lee, "Picosecond optics and microwave technology," *IEEE Trans. on Microwave Theory and Techniques*, vol. 38, pp. 596–607, May 1990.

[25] A.M.Vaucher, C.D.Striffler, and C.H.Lee, "Theory of optically controlled millimeter wave phase shifters," *IEEE Trans. on Microwave Throry and Techniques*, vol. 31, pp. 209–216, Feb. 1983.

[26] A.J.Seeds, "Optical technologies for phased array antennas," *IEICE Trans. on Electron*, vol. E76-C, pp. 198–206, Feb. 1993.

[27] A.J.Seeds and A.A.A.Salles, "Optical control of microwave semiconductor devices," *IEEE Trans. on Microwave Theory and Techniques*, vol. 38, pp. 577–585, May 1990.

[28] W.Platte, "Optoelectronic microwave switching," *IEE Proc., Pt.J*, vol. 132, pp. 126–132, April 1985.

[29] P.Herczfeld and et al., "Optical gain and phase control of a GaAs MMIC transmit/receiver module," in *Proc. of 18th EuMc Dig.*, pp. 831–836, 1988.

[30] R.A.Kiehl, "Novel optical control techniques for solid-state radar transmitters," *IEEE Trans. on Microwave Theory and Techniques*, vol. 28, pp. 409–413, April 1980.

[31] W.Platte and B.Sauerer, "Optically CW-induced losses in semiconductor coplanar waveguides," *IEEE Trans. on Microwave Theory and Techniques*, vol. 37, pp. 139–148, Jan. 1989.

[32] P.Cheung, D.P.Neikirk, and T.Itoh, "Optically controlled coplanar waveguide phase shifters," *IEEE Trans. on Microwave Theory and Techniques*, vol. 38, pp. 586–595, May 1990.

[33] C.H.Lee, P.S.Mak, and A.P.Defonzo, "Optical control of millimeter-wave propagation in dielectric waveguide," *IEEE J. of Quantum Electronics*, vol. 16, no. 3, pp. 277–288, 1980.

[34] E.Sano and T.Shibata, "Fullwave analysis of picosecond photoconductive switches," *IEEE J. of Quantum Electronics*, vol. 26, no. 2, pp. 372–377, 1990.

[35] R.J.Luebbers, F.P.Hunsberger, K.Kunz, R.B.Standler, and M.schneider, "A frequency dependent finite difference time domain formulation for dispersive materials," *IEEE Trans. on Electromagnetic Compatibility*, vol. 32, no. 3, pp. 222–227, 1990.

[36] R.J.Luebbers, F.P.Hunsberger, and K.S.Kunz, "A frequency dependent finite difference time domain formulation for transient propagation in plasma," *IEEE Trans. on Antenna and Propagation*, vol. 39, pp. 29–34, Jan. 1991.

[37] C.Laperle, Y.Shen, and P.Jarmuszewski, "Integrated receiver for digital beamforming," in *Proc. of 1993 TRIO/ITRC Research Retreat*, (Peterborough), 1993.

[38] Y.Shen, R.Fralich, C.Wu, and J.Litva, "Active radiating oscillator using a reflection amplifier module," *Electronics Letters*, vol. 28, pp. 991–992, June 1992.

[39] Y.Shen, R.Fralich, C.Wu, and J.Litva, "Active radiating oscillator using FET source integrated with a multilayer slot coupled patch antenna," in *Proc. of 1992 IEEE APS Int. Symp.*, pp. 1052–1055, July 1992.

[40] Y.Shen, C.Laperle, N.Sangary, and J.Litva, "A symmetrical 4-element active array module for spatial power combiner," in *Proc. of 1993 IEEE APS Int. Symp.*, pp. 838–841, June 1993.

[41] Y.Shen, C.Laperle, N.Sangary, and J.Litva, "A new active array module for spatial power combiners and active antennas," *submittd to IEEE Trans. on Microwave Theory Tech.*, 1993.

[42] Y. Shen, N. Sangary, C. Laperle, P. Jarmuszewski, and J. Litva, "Circular quasi-optical power-combining arrays," *submitted to 1994 IEEE MTT-S*, 1994.

[43] Y.Shen, Z.Bi, K.Wu, and J.Litva, "FD-TD analysis open cylindrical dielectric resonators," *Microwave and Optical Technology Letters*, vol. 5, pp. 261–265, May 1992.

[44] Y.Shen, Z.Bi, K.Wu, and J.Litva, "Efficient FDTD analysis of dielectric resonators with tuning screw and multilayer structures," in *Proc. of 1992 IEEE MTT-S Int. Microwave Symp.*, pp. 967–970, June 1992.

[45] Y.Shen, Z.Bi, K.Wu, and J.Litva, "Study of $TE_{01\delta}$ mode in open dielectric resonators by a finite differnce time domain method," in *Proc. of 1991 Canadian Conf. on Electrical and Computer Engineering*, pp. 236–240, Sept. 1991.

[46] Z.Bi, Y.Shen, K.Wu, and J.Litva, "Fast finite difference time domain analysis of resonators by using digital filtering and spectrum estimation techniques," *IEEE Trans. on Microwave Theory and Techniques*, vol. 40, pp. 1611–1619, Aug. 1992.

[47] Z.Bi, Y.Shen, K.Wu, and J.Litva, "Enhancing finite difference time domain analysis of dielectric resonators using spectrum estimation techniques," in *Proc. of 1992 IEEE MTT-S Int. Microwave Symp.*, pp. 869–872, 1992.

[48] Y.Shen, K.Nickerson, and J.Litva, "Frequency dependent FDTD method for optically controlled dielectric resonators," *IEEE Trans. on Microwave Theory and Techniques*, vol. 41, June 1993.

[49] Y.Shen, K.Nickerson, C.Wu, J.Litva, and D.Conn, "Full-wave analysis of optically controlled semiconductor coplanar waveguides," in *Proc. of 1993 IEEE APS Int. Symp.*, pp. 1370–1373, June 1993.

[50] Y.Shen, K.Nickerson, J.Litva, and D.Conn, "Modified $(FD)^2TD$ method for three-dimensional optically controlled phase shifters/attenuators," *to submit to IEEE Trans. on Microwave Theory and Techniques*, 1993.

[51] R.J.Mailloux, "Phased array architecture for mm-wave active arrays," *Microwave J.*, vol. 29, pp. 117–124, July 1986.

[52] D.M.Pozar and D.H.Schaubert, "Comparison of architectures for monolithic phased array antennas," *Microwave J.*, vol. 29, pp. 93–104, March 1986.

[53] J.W.Mink, "Quasi-optic power combining of solid-state millimeter-wave sources," *IEEE Trans. on Microwave Theory Tech.*, vol. MTT-34, pp. 273–279, Feb. 1986.

[54] C.Zah, R.C.Compton, and D.B.Rutledge, "Efficiencies of elementary integrated-circuit feed antennas," *Electromagnetics*, vol. 3, pp. 239–254, 1983.

[55] J.Litva, Z. Bi, K.Wu, R.Fralich, and C.Wu, "Full-wave analysis of an assortment of printed antenna structures using the fdtd method," in *Proc. of 1991 IEEE AP-S Int. Symp.*, pp. 410–413, June 1991.

[56] R.Fralich, J.Wang, and J.Litva, "Enhanced precision microstrip antenna measurements with non-standard impedance lines at an arbitrary reference plane," CRL report 228, McMaster Univ., Jan. 1991.

[57] G.D.Vendelin, A.M.Pavio, and U.L.Rohde, *Microwave circuit design using linear and nonlinear techniques.* John Wiley and Sons, 1990.

[58] C.A.Balanis, *Antenna Theory Analysis and Design.* John Wiley & Sons, 1982.

[59] K.D.Stephan and T.Itoh, "Recent efforts on planar components for active quasi-optical applications," in *Proc. of 1990 IEEE MTT-S Int. Microwave Symp.*, pp. 1205–1208, May 1990.

[60] Z.B.Popovic, R. II, M.Kim, and D.B.Rutledge, "A 100-MESFET planar grid oscillator," *IEEE Trans. on Microwave Theory Tech.*, vol. 39, pp. 193–200, Feb. 1991.

[61] Z.B.Popovic, R. II, M.Kim, K.A.Potter, and D.B.Rutledge, "Bar-grid oscillators," *IEEE Trans. on Microwave Theory Tech.*, vol. 38, pp. 225–230, March 1990.

[62] R.A.York and R.C.Compton, "Quasi-optical power combining using mutually synchronized oscillator arrays," *IEEE Trans. on Microwave Theory Tech.*, vol. 39, pp. 1000–1009, June 1991.

[63] Y. Shen, N. Sangary, C. Laperle, P. Jarmuszewski, and J. Litva, "Circular active array for quasi-optical spatial power combiners," *submitted to IEEE Trans. on Microwave Theory Tech.*, 1993.

[64] R.Simons, *Optical control of microwave devices.* Artech House, 1991.

[65] W.B.Scott, "Air force funding joint studies to develop smart skin avionics," *Aviation Week and Space Technology*, vol. 128, pp. 65–69, April 1988.

[66] G.Gustafson, M.Bendett, J. Carney, R.Mactaggart, and et al., "Gaas circuits for monolithic optical controller," in *Optoelectronic Signal Processing for Phased-Array Antennas*, pp. 80–87, SPIE, 1988.

[67] K.S.Yee, "Numerical solution of initial boundary value problems involving Maxwell's equations in isotropic media," *IEEE Trans. on Antennas Propagat.*, vol. 14, pp. 302–307, May 1966.

[68] A.Navarro, M.J.Nanez, and E.Martin, "Study of TE_0 and TM_0 modes in dielectric resonators by a finite difference time-domain method coupled with the discrete fourier transform," *IEEE Trans. on Microwave Theory Techn.*, vol. MTT-39, no. 1, pp. 14–17, 1991.

[69] F.H.Gil and J.P.Martinez, "Analysis of dielectric resonators with tuning screw and supporting structure," *IEEE Trans. on Microwave Theory Techn.*, vol. MTT-33, pp. 1453–1457, Dec. 1985.

[70] J.C.Bolomey, C.Durix, and D.Lesselier, "Time domain integral equation approach for inhomogenious and dispersive slab problems," *IEEE Trans. on Antennas Propagat.*, vol. AP-26, pp. 658–667, Sept. 1978.

[71] R.A.Smith, *Semiconductors.* Cambridge: Cambridge, MA, 1968.

[72] R.F.Pierret, *Modular series on solid state devices, Volume VI: Advanced semiconductor fundamentals.* Addison-Wesley Publishing Comp., 1989.

[73] D.Kajfez and P.Guillon, *Dielectric Resonators.* Artech House, Inc., 1986.

[74] P.R.Herczfeld, A.Daryoush, C.D.Ascenzo, M.Contarino, and A.Rosen, "Optically controlled and FM modulated X-band dielectric resonator oscillator," in *Proc. of 14th European Microwave Conf.*, pp. 268–273, 1984.

[75] J.S.Blakemore, "Semiconducting and other major properties of gallium arsenide," *J. Appl. Phys.*, vol. 53, pp. R123–R181, 1982.

[76] Y.P.Varshni, "Band-to-band radiative recombination in groups IV, VI, and III-V semiconductors (II)," *Phys. Stat. Sol.*, vol. 20, pp. 9–36, 1967.

[77] Y.P.Varshni, "Band-to-band radiative recombination in groups IV, VI, and III-V semiconductors (I)," *Phys. Stat. Sol.*, vol. 19, pp. 459–514, 1967.